1-11-2016

The origin of mantle xenoliths in Tertiary alkaline basalts, British Columbia, Canada: Implications for convergent plate margin geodynamic and petrogenetic processes

Eyal Friedman
University of Windsor

The origin of mantle xenoliths in Tertiary alkaline basalts, British Columbia, Canada: Implications for convergent plate margin geodynamic and petrogenetic processes

By

Eyal Friedman

A Thesis
Submitted to the Faculty of Graduate Studies
through the Department of Earth and Environmental Sciences
in Partial Fulfillment of the Requirements for
the Degree of Master of Science
at the University of Windsor

Windsor, Ontario, Canada
2015

The origin of mantle xenoliths in Tertiary alkaline basalts, British Columbia, Canada: Implications for convergent plate margin geodynamic and petrogenetic processes

by

Eyal Friedman

APPROVED BY:

_____

Dr. B. Zielinski, External Examiner
Department of Biological Sciences

_____

Dr. I. Samson, Internal Examiner
Department of Earth and Environmental Sciences

_____

Dr. A. Polat, Advisor
Department of Earth and Environmental Sciences

December 17, 2015

Declaration of Co-Authorship / Previous Publication

I. Co-Authorship Declaration

I hereby declare that this thesis incorporates material that is result of joint research, as follows:

The collaboration occurs in Chapters 1-9 of this thesis. These chapters contain material that has been accepted for publication. Field work was conducted with Ali Polat. Robert Frei assisted with radiogenic isotope analyses. Ali Polat, Derek Thorkelson and Robert Frei contributed to the manuscript by means of criticism and revision. With these exceptions, field observations, laboratory analyses, data interpretation, key ideas and manuscript preparation were performed by the author.

I am aware of the University of Windsor Senate Policy on Authorship and I certify that I have properly acknowledged the contribution of other researchers to my thesis, and have obtained written permission from each of the co-author(s) to include the above material(s) in my thesis.

I certify that, with the above qualification, this thesis, and the research to which it refers, is the product of my own work.

II. Declaration of Previous Publication

This thesis includes 1 original paper that has been accepted for publication in a peer reviewed journal, as follows:

Thesis Chapter	Publication Title/Full Citation	Publication Status*
Chapters 1-9	**Eyal Friedman** (60%), Ali Polat (20%), Derek Thorkelson (10%), Robert Frei (10%), Formation of the subcontinental lithospheric mantle beneath southern British Columbia, Canada, at a convergent plate margin: Evidence from trace element geochemistry of mantle xenoliths	Accepted for Publication (Gondwana Research)

I certify that I have obtained a written permission from the copyright owner(s) to include the above published material(s) in my thesis. I certify that the above material describes work completed during my registration as graduate student at the University of Windsor.

I declare that, to the best of my knowledge, my thesis does not infringe upon anyone's copyright nor violate any proprietary rights and that any ideas, techniques, quotations, or any other material from the work of other people included in my thesis, published or otherwise, are fully acknowledged in accordance with the standard referencing practices. Furthermore, to the extent that I have included copyrighted material that surpasses the bounds of fair dealing within the meaning of the Canada Copyright Act, I certify that I have obtained a written permission from the copyright owner(s) to include such material(s) in my thesis.

I declare that this is a true copy of my thesis, including any final revisions, as approved by my thesis committee and the Graduate Studies office, and that this thesis has not been submitted for a higher degree to any other University or Institution.

Abstract

The Tasse basalts of southeastern British Columbia, Canada, are host to a variety of mantle xenoliths consisting predominantly of spinel lherzolite with minor dunite and pyroxenite. On the basis of REE patterns, the xenoliths are divided into three groups reflecting varying degrees of mantle metasomatism: (1) Group 1; concave-up LREE patterns; (2) Group 2; flat to moderately LREE-enriched patterns; and (3) Group 3; strongly LREE-enriched patterns. The majority of xenolith are enriched in LILE, LREE, U, Th, Pb, and Sr, and depleted in HFSE and HREE. These geochemical characteristics are consistent with a sub-arc mantle source. The Tasse lavas are compositionally alkaline basalts and display OIB-like trace element patterns. They have positive εNd (+3.8 to +5.5) values, with 338−426 Ma depleted mantle model ages, and display OIB-like Nd, Sr and Pb isotopic compositions. The Sr−Nd−Pb isotope and trace element characteristics suggesting that they originated from an upwelling asthenospheric mantle source.

This thesis is dedicated to my parents, Martin and Eva, and my brother, Tal, for all of their love, encouragement and support through this journey.

This thesis is also in loving memory of my best friend Andrew Avetikov. You will forever be in my memories and in my heart.

April 2, 1986 – November 9, 2013

Acknowledgements

This thesis has been a long time coming. This journey would not have been possible without the help of Dr. Ali Polat. I would like to thank Dr. Polat for his guidance and patience over the past few years through this process. I would also like to thank him for giving me this wonderful opportunity.

I would also like to thank Dr. Iain Samson for sharing his expertise in petrography and mineralogy. His insights allowed me to further develop key concepts in my research and studies.

Special thanks go to Melissa Price and the staff at GLIER for all their help with laboratory equipment and processes.

Thank you to Dr. Barb Zielinski for being a part of my committee and giving me feedback and constructive criticism during my thesis proposal and defense.

A final thank you goes to all of my graduate peers who have had to put up with me over the past few years. I appreciate all of the help you have given me and wish you the best with your areas of research.

Table of Contents

List of Tables

List of Figures

CHAPTER 1
Introduction

The mantle has played a major role in the evolution of the Earth (Hofmann, 1997; Wang et al., 2007; König et al., 2008). Since the mantle cannot be directly sampled, studies of mantle xenoliths have provided significant insights into our understanding of the geodynamic and petrological processes that shaped the evolution of the mantle-crust system (McCulloch, 1993; McCulloch and Bennett, 1994; Hofmann, 1997; Kerrich et al., 1999; Condie, 2000; Downes, 2001; Bennett, 2003; Arai et al., 2007; Chin et al., 2012). Samples recovered from kimberlites, lamproites and alkaline basalts have placed new constraints on the petrogenetic and geodynamic processes operating over the past 3.5 billion years (Shi et al., 1998; Wyman and Kerrich, 2010; Shirey and Richardson, 2011; Tang et al., 2013). These constraints have improved our understanding of plate tectonics, mantle plumes, and mantle composition (Ballhaus, 1993; Putirka, 1999; Beccaluva et al., 2004; Nkouandou and Temdjim, 2011; Shirey and Richardson, 2011) and provided insight into geodynamics, geochemistry, geophysics, and many other branches of Earth Sciences.

Mantle xenoliths hosted in alkaline basalts have been documented world-wide (Brearley et al., 1984; Parkinson et al., 2003; Ionov et al., 2006; De Hoog et al., 2010; Nkouandou and Temdjim, 2011; Tang et al., 2013; Downes et al., 2014). Alkaline basalts are lower in silica content than mid-ocean ridge basalts (MORB) and are characterised by high alkali content (Na_2O+K_2O) (Polat et al., 1997; Nkouandou and Temdjim, 2011; Li et al., 2014). The origin of alkaline basalts can be explained by two main processes: (1) low degrees of partial melting of mantle (Kay and Gast, 1973; Wilshire et al., 1988); and (2) partial melting of enriched mantle (Wilshire et al, 1980; Wilshire et al., 1988; Maury et

al., 1992; Polat et al., 1997). Enriched mantle may be produced by metasomatism involving hydrous and/or carbonate-rich fluids, intrusion of silicate magmas, or physical mixing between 'normal' mantle and fertile rocks such as pyroxenite and eclogite. These processes can raise the abundances of incompatible elements in the mantle which, in turn, can lead to greater alkalinity in derivative magmas (Bailey, 1972, 1982; Wilshire et al., 1988). British Columbia, Canada, is known to host various locations of alkaline basalts within its complex geological history (Fig. 1) (Brearley and Scarfe, 1984; Brearley et al., 1984; Sun and Kerrich, 1995; Shi et al., 1998; Edwards and Russell, 2000; Peslier et al., 2000a, 2000b; Ferri and O'Brien, 2002; Peslier et al., 2002; Abraham et al., 2005; Sluggett, 2008; Greenfield et al., 2013).

Several outstanding questions remain in regards to the evolution of the subcontinental lithospheric mantle and relationship to subduction and orogenic processes beneath southeastern British Columbia. How did the mantle evolve during the subduction and orogenic processes? What are the origins of the Miocene to Holocene alkaline lavas that emplaced the mantle xenoliths? Is there a relation between the evolution of the mantle and the origin of the alkaline basalts? How did continental-scale tectonic processes play a role in the origin of alkaline basalts and their mantle xenoliths? In this study, we present whole-rock major and trace element data for twenty-two samples of mantle xenoliths and twenty-three samples of alkaline basalts collected from the Tasse property of Barker Minerals Ltd, near Likely, British Columbia (Figs. 1 and 2). In addition, we report whole-rock Sr−Nd−Pb isotope data for seven alkaline basalt samples. Using the new and previously published data, we address the questions regarding the petrogenesis of the mantle xenoliths and their host alkaline basalts with respect to the

subcontinental lithospheric and asthenospheric mantle domains beneath southeastern British Columbia.

CHAPTER 2
Regional geology

The Canadian Cordillera consists of rocks that range in age from Paleoproterozoic to Holocene. They are commonly divided into assemblages that originated along the western margin of ancestral North America (cratonic), near North America (pericratonic) or far from North America (exotic) (Gabrielse et al., 1991; Nelson and Colpron, 2007). In the Mesozoic, these assemblages were brought together by subduction, forming a collage of accreted terranes (tectonic blocks) and deformed cratonic and pericratonic rocks (Fig. 3) (Coney et al., 1980; Monger et al., 1982; Gabrielse et al., 1991; Johnston, 2001). These events led to westward growth of the North American continent and the formation of a new western margin near to that of the present day coastline. By the Cenozoic, most of the accretionary tectonism was complete but the Cordillera continued to undergo deformation, metamorphism and magmatism (Fig. 3). During the Paleocene and Eocene, two or three oceanic plates were subducting beneath the continental margin, leading to widespread magmatism, strike-slip deformation, localized extension and core-complex formation (Ewing, 1980; Parrish et al. 1988). During this time, magmatism was voluminous and subduction processes were modified by the effects of ridge subduction and slab window formation (Breitsprecher et al., 2003; Madsen et al., 2006). Offshore plate reorganization in the mid-Cenozoic led relative quiescence in the Oligocene and restriction of arc magmatism to the northern and southern parts of the Canadian Cordillera (Madsen et al., 2006). The sum of all of the aforementioned activity led to the recognition of five morphogeologic belts which are characterized by a combination of features including terrane type and origin, age, metamorphic grade and geomorphology (Fig. 4) (Gabrielse et al., 1991; Monger, 2014). During the Miocene to Holocene,

magmatic activity was widespread throughout the region, and was grouped by Bevier et al. (1979) into three main regions: the Cascade-Garibaldi arc in the southwest, the Aleutian-Wrangell volcanic belt in the northwest, and a broad intervening region of varied but largely mafic alkaline volcanism. This intervening volcanic field was regarded having a range of causes including back-arc volcanism (Chilcotin Group) and mantle plume activity (Anahim belt) (Fig. 1) (Bevier et al., 1979; Kuehn et al., 2015). Edwards and Russell (2000) re-examined the northern part of this mafic field, named it the Northern Cordilleran Volcanic Province (NCVP) (Fig. 1), and suggested that lithospheric extension played a primary role in its development.

Using a different approach, Thorkelson and Taylor (1989) and Thorkelson et al. (2011) regarded the Chilcotin-Anahim-NCVP field as having a common origin related to subduction of the Juan de Fuca spreading ridge and formation of an extensive slab window in the Late Cenozoic. In this model, the entire region between the Garibaldi and Wrangell arcs was affected by upflow of asthenospheric mantle through the slab window, leading to low-degree partial melts of mantle peridotite. According to the interpretations of Edwards and Russell (2000), Greenfield et al. (2013) and Francis et al. (2010), both asthenospheric and lithospheric mantle were involved in the mantle anatexis. As noted by Edwards and Russell (2000), Francis et al. (2010) and Thorkelson et al. (2011), the previously identified processes of back-arc circulation (developed more fully by Currie and Hyndman, 2006), plume activity and lithospheric extension may have contributed locally to the various volcanic belts included within the field of slab window magmatism. In addition, general westward mantle flow and continental lithospheric delamination may have contributed to the magmatic activity (Bao et al., 2014). Importantly, these processes

contributed to the current thermal (hot) and rheological (weak) state of the central and western Cordillera (Hyndman et al., 2009), in which a thin layer of lithospheric mantle underlies a hot crust with high heat flow and a Moho temperature near 800 °C (Harder and Russell, 2006; Francis et al., 2010; Greenfield et al., 2013). Thinning of the mantle lithosphere is likely to be ongoing (Francis et al., 2010).

CHAPTER 3
Geology of the study area

The study area is located within the Cariboo district, which lies within the southern portion of the Omineca belt (Fig. 4) (Monger and Price, 2002). The region consists of various terranes including the Cariboo, Quesnel, Cache Creek and Kootenay terranes (Fig. 2) (Ferri and Schiarizza, 2006; Eyles and Miall, 2007). The Cariboo terrane has been identified as a representative piece of the ancestral North American margin. This portion of the terrane contains carbonate and siliciclastic rocks (Struik, 1986; Ferri and Schiarizza, 2006).

The Barkerville subterrane, of the larger Kootenay terrane, is bounded on both sides by thrust faults (Figs. 2 and 5) (Struik, 1986; Ferri and Schiarizza, 2006). To the west of the Barkerville subterrane is the Eureka thrust fault that separates the Barkerville subterrane from the Quesnel terrane (Figs. 2 and 5). The Pundata thrust and Pleasant Valley thrust separate the Cariboo terrane from the eastern edge of the Barkerville subterrane (Figs. 2 and 5) (Struik 1986; Ferri and Schiarizza, 2006).

The Quesnel terrane consists principally of arc volcanic and sedimentary rocks. This terrane has been thrust onto the hanging wall of the Eureka thrust and Crooked amphibolite of the Slide Mountain terrane (Figs. 2 and 5) (Struik 1986; Ferri and Schiarizza, 2006). The sedimentary rocks are of the Nicola Group and characterized by phyllitic rocks with interbeds of siltstones to fine-grained sandstone. Minor mafic tuffaceous and coarse-grained volcaniclastic rocks have been found to interfinger in the Nicola Group (Ferri and O'Brien, 2002; Ferri and Schiarizza, 2006; Thomas, 2009). Numerous sills and plutons, granitic to gabbroic, have intruded the stratigraphic units, mainly the Snowshoe Group. The Nicola and Snowshoe stratigraphic units are separated

by the Eureka thrust fault (Thomas, 2009). Granitic sills are the most extensive of all igneous bodies. The Quesnel Lake gneiss protolith consists of megacrystic granite to granodiorite (Ferri et al., 1999; Ferri and Schiarizza, 2006).

The region has undergone various degrees of deformation, magmatism, sedimentation, and metamorphism. The highest intensity of deformation took place during the Early to Middle Jurassic (Ferri and Schiarizza, 2006). The obduction of the Quesnel arc rocks onto the Kootenay terrane appears to have been the cause of the intense deformation. This largely occurred along the Eureka thrust in the Northern Kootenay terrane (Ferri and Schiarizza, 2006). The ensuing obduction of the Quesnel arc rocks, southwest folding was accompanied by greenschist to amphibolite facies metamorphism. There have been multiple generations of folding and metamorphism throughout the region (Ferri and Schiarizza, 2006). The neighbouring Barkerville-Cariboo terrane boundary structures indicate similar fold patterns that postdate other events and are associated with a younger metamorphic event (Ferri and Schiarizza, 2006).

All sampled outcrops of this study are devoid of weathering and volcanic cone structures are well preserved in the study area, suggesting a young age for the sampled alkaline basalts. Recently, Kuehn et al. (2015) dated the volcanic rocks in the region (e.g., the Satah Mountain and Baldface Mountain volcanic fields) using $^{40}Ar/^{39}Ar$ geochronology. Only one sample was collected from the Tasse basalts and yielded an age of 0.174±0.007 Ma.

CHAPTER 4
Sampling

Sampling was conducted on the Tasse property of Barker Minerals, near the north shore of Quesnel Lake (Figs. 1 and 2). A total of 61 samples were collected from six alkaline basalt volcanic centres (Fig. 6); 32 mantle xenoliths and 29 alkaline basalts (Fig. 7; Appendices A and B). The sizes and weights ranged from ~7 cm – 20+ cm and 1 kg – 7+ kg. The *Global Positioning System* (*GPS*) coordinates for sample locations are given in Appendices A and B.

CHAPTER 5
Methodology

5.1 Major and trace element analyses

A total of 45 samples were selected for both major and trace element analyses (Tables 1 and 2). Major elements and specific trace elements (Ba, Sr, Y, Sc, Zr, V) were analysed by Thermo Jarrell-Ash ENVIRO II ICP, at Activation Laboratories Ltd. (Actlabs) in Ancaster, Ontario. The samples were fluxed using lithium metaborate and lithium tetraborate agents followed by digestion with nitric acid, 5% solution (http://www.actlabs.com/).

Trace element analyses includes large ion lithophile elements (LILE; e.g., K, Rb, Ba), rare earth elements (REE; e.g., La-Lu), high field strength elements (HFSE; e.g., Zr, Hf, Nb, Ta). Analyses were conducted at Geoscience Laboratories (Geo Labs) in Sudbury, Ontario, using inductively coupled plasma-mass spectrometry (ICP-MS). The samples were digested by using multi-acid techniques (method code IM100) as detailed by Burnham et al. (2002).

Selected elements were normalized to chondrite (cn) (see McDonough and Sun, 1995) and average normal-mid-ocean ridge basalt (MORB) (see Sun and McDonough, 1989). The chondrite-normalized anomalies of Ce/Ce* [$Ce_{cn}/(La_{cn} \times Pr_{cn})^{0.5}$] and Eu/Eu* were calculated with respect to the neighbouring elements (see Tables 1 and 2), following the method of Taylor and McLennan (1985). Similarly, N-MORB-normalized Nb/Nb*, Pb/Pb*, Zr/Zr*, and Ti/Ti* anomalies were calculated with respect to the neighbouring elements (see Tables 1 and 2) using the same method. Mg-numbers were calculated as the molar ratio of $Mg/(Mg+Fe^{2+})$, where Fe^{2+} is assumed to be 90 % of total Fe.

5.2 Strontium, neodymium and lead isotope analyses

Seven samples of alkaline basalts were selected for Sr, Nd and Pb isotope analyses at the Geological Institute, University of Copenhagen, Denmark. Details of the analytical procedure are given in Frei and Polat (2013). The powdered samples were dissolved through standard procedures using concentrated HNO_3, HF and HCl within Savillex^{TM} beakers on a hotplate at 130ºC for 3 days. A $^{150}Nd/^{147}Sm$ spike was added before dissolution. The isotopic ratios of Sm, Nd, Pb and Sr, and of Sm and Nd isotopic dilution concentrations were determined from separately dissolved powder aliquots using a VG Sector 54 IT Thermal Ionization Mass Spectrometer (TIMS).

Element separation was carried out using chromatographic columns charged with 12 ml AG50W-X 8 (100–200 mesh) cation resin, where Sr and REE fractions were collected. Rare earth element fractions were further separated over smaller chromatographic columns containing Eichrom's^{TM} LN resin SPS (Part# LN-B25-S). Strontium cuts were purified using a standardized 3M HNO_3-H_2O elution recipe on self-made disposable mini-extraction columns, following the procedure of Horwitz et al. (1992). $^{87}Rb/^{86}Sr$ ratios were calculated using ICP-MS Rb and Sr concentrations.

Samarium isotopes were measured in a static multi-collection mode, whereas Nd isotope ratios were measured in a multi-dynamic routine, both on a triple Ta-Re-Ta filament setting. The measured Nd isotope ratios were normalized to $^{146}Nd/^{144}Nd=0.7219$. The mean value of $^{143}Nd/^{144}Nd$ ratios for the JNdi standard runs during the period in which the samples were analyzed amounted to 0.512105±5 (2σ; n=8). Precision for $^{147}Sm/^{144}Nd$ ratios is better than 2% (2σ).

Chemical separation of Pb from the whole-rock aliquot was carried out using conventional glass stem and subsequently miniature glass stem anion exchange columns containing, respectively, 1 ml and 200µl of 100–200 mesh Bio-Rad AG 1×8 resin. Lead isotope ratios were determined in a static multi-collection-mode where fractionation was controlled by repeated analysis of the NBS 981 standard using values of Todt et al. (1993). Total procedural blanks were below <200 pg Pb which compared to >100 ng Pb loads.

CHAPTER 6
Petrography

6.1 Mantle xenoliths

The samples were studied using transmitting light microscopy and scanning electron microscope (SEM) with energy dispersive spectroscopy (EDS) to determine their textural and compositional characteristics. The xenoliths are dominantly spinel lherzolites with minor dunite and pyroxenite. They typically display a phaneritic, granoblastic texture, with triple junction grain boundaries (Fig. 8). Several associations have been identified, such as pyroxene-spinel and melt-fluid inclusions with pyroxene and spinel. A small number of samples exhibit small bands of neoblasts with a mosaic-like texture. Olivine comprises the largest modal abundances (40−70%) in the xenoliths. They are typically subhedral, homogeneous, one to two millimeters in size, colourless to pale yellow-green (Figs. 8 and 9), and are of forsterite ($Fo_{87–93}$) composition.

Pyroxene grains are anhedral to subhedral, often fractured, constitute 30−50% of the samples and are dominated by ca. one millimeter orthopyroxene (enstatite) and clinopyroxene (diopside). Orthopyroxene grains are light brown and in some samples show evidence of mineral-melt chemical reactions (resorption). Clinopyroxene grains are tinted green and contain, on average, 0.8 wt.% Cr. Clinopyroxene also shows evidence of mineral-melt chemical reactions (resorption) displaying a mottled texture associated with fluid and/or melt inclusions (Figs. 8 and 9).

Spinel is the only major aluminous phase present and the least abundant mineral, comprising approximately 5% of the samples. Spinel grains are homogenous, reddish brown to dark brown, 250−300 micrometers in size, and compositionally Cr-rich. The majority of spinel grains are anhedral and sporadically display xenomorphic and skeletal

textures (see also Mercier and Nicolas, 1975). Spatially spinel is associated with clinopyroxene and occasionally displays diffuse grain boundaries (Fig. 8).

Other studies of mantle xenoliths from within British Columbia reported similar mineralogical and textural characteristics, with only minor differences (Littlejohn and Greenwood, 1974; Brearley and Scarfe, 1984; Brearley et al., 1984; Sun and Kerrich, 1995; Peslier et al., 2002; Greenfield et al., 2013). Some studies documented exsolution lamellae of clinopyroxene within the orthopyroxene (Littlejohn and Greenwood, 1974; Peslier et al., 2002). Augite-bearing mantle xenoliths were identified in numerous locations (Littlejohn and Greenwood, 1974; Brearley and Scarfe, 1984; Peslier et al., 2002), as well as harzburgites (Littlejohn and Greenwood, 1974; Peslier et al., 2002; Greenfield et al., 2013). A sample containing pargasitic amphibole (mode <5%) was found in a Cr-diopside spinel lherzolite by Brearley and Scarfe (1984) from Lightning Peak in British Columbia.

6.2 Alkaline basalts

The host rocks compositionally range from basanites to alkaline basalts and are very fine-grained and vesicular (Fig. 10). Due to the fine-grained nature it is difficult to determine its exact mineralogical composition. Plagioclase (± nepheline) and pyroxene and Fe-Ti oxide phases were identified. Olivine fragments from the mantle xenoliths are also present. Olivine and plagioclase display various skeletal textures (Fig. 10d). Several samples contain quartz xenocrysts with a reaction rim of unknown fine-grained minerals.

CHAPTER 7
Results

7.1 Mantle xenoliths

The mantle xenoliths are characterized by 42.8−45.2 wt.% SiO_2, 37.5−42.7 wt.% MgO, 8.2−9.7 wt.% Fe_2O_3 (Table 1). Al_2O_3 (0.85−4.61 wt.%) and TiO_2 (0.02−0.16 wt.%) show moderate variations, resulting in super-chondritic Al_2O_3/TiO_2 (21−72) ratios (Table 1). CaO concentrations range from 0.61−3.8 wt.%, whereas the CaO/Al_2O_3 possess a narrow range (0.71−0.92). They have rather restricted Mg-numbers (89−92%) but are strongly depleted in incompatible elements (Ba=2−11 ppm; Sr=3−31 ppm; Zr=6−21 ppm, K_2O=0.01−0.07 wt.%) and variably depleted in transitional metals (V=41−95 ppm; Sc=6−17 ppm) (Table 1). Yttrium (1−3 ppm) is also strongly depleted. Both Zr/Hf and Nb/Ta ratios show sub- to super-chondritic values (Zr/Hf=34−60 and Nb/Ta=13−32) whereas Y/Ho (25−31) retains a near-chondritic value (Fig. 11; Table 1).

On the basis of chondrite-normalized REE patterns, samples are divided into three groups: (1) Group 1 has concave-up LREE patterns (La/Sm_{cn}=0.48−1.16; Gd/Yb_{cn}=0.71−0.92) (Fig. 12a); (2) Group 2 is characterized by flat to moderately LREE-enriched patterns (La/Sm_{cn}=1.14−1.92; Gd/Yb_{cn}=0.87−1.09) (Fig. 12b); and (3) Group 3 displays strongly LREE-enriched patterns (La/Sm_{cn}=1.53−2.45; Gd/Yb_{cn}=1.00−1.32) (Fig. 12c). All three groups display negative Ti anomalies (Ti/Ti^*_{MORB}=0.68−0.95) relative to Eu and Gd (Table 1; Figs. 12e-g and 13). In all Groups, Zr displays positive anomalies (Zr/Zr^*_{MORB}=1.11−2.13) relative to Sm and Eu (Table 1; Figs. 12e-g and 13). Two outlier samples (TA-2012-14, TA-2012-25) do not fit into the initial three groupings and display separate geochemical signatures (Fig. 12d and h). These two outlier samples represent the highest Mg-numbers of 90.6 and 91.9, as well, La/Sm_{cn} ratios 5.65 and 6.65,

respectively (Table 1). TA-2012-14 possesses the highest Al_2O_3/TiO_2 ratio of 72 (Table 1). The outlier samples also have larger positive Zr anomalies (Zr/Zr^*_{MORB}= 3.37−4.78) than the rest of samples (Fig. 12h). All samples have negative Nb anomalies (Nb/Nb^*_{MORB}=0.18−0.89) relative to U and K (Fig. 12).

7.2 Alkaline basalts

The Tasse alkaline basalts are characterized by low SiO_2 (44.2−46.0 wt.%) values. They have moderately variable MgO (6.5−10.2 wt.%), CaO (7.5−8.6 wt.%), Fe_2O_3 (12.9−14.9 wt.%), and Al_2O_3 (13.6−15.0 wt.%) contents (Table 2). Mg-numbers (%) vary between 47 and 59. High total alkaline element values (Na_2O+K_2O=5.1−6.6 wt.%) (Table 2) are consistent with an alkaline basalt composition. They have highly fractionated REE patterns (La/Sm_{cn}=3.15−3.80; Gd/Yb_{cn}=3.42−4.61) (Fig. 14a), consistent with an alkaline basalt affinity. They are strongly enriched in incompatible elements (e.g., TiO_2=2.38−3.1 wt.%; Ba=580−797 ppm; Sr=872−993 ppm; Zr=302−383 ppm) (Fig. 14b). High Zr and low Y (24−27 ppm) concentrations resulting in high Zr/Y=12−14. The basalts display positive anomalies of Zr (Zr/Zr^*_{MORB}=1.32−1.51) and negative Ti (Ti/Ti^*_{MORB}=0.80−0.96) anomalies (Table 2). Niobium shows slight positive anomalies (Nb/Nb^*_{MORB}=0.98−1.18) (Table 2). The samples are uniform in composition and exhibit very narrow ranges amongst major and trace elements.

7.3 Strontium, neodymium and lead isotopes of the alkaline basalts

The Tasse basalts have very small ranges of $^{87}Sr/^{86}Sr$ (0.703346−0.703591). $^{87}Rb/^{86}Sr$ ratios range from 0.1185 to 0.1269 (Table 3). They have uniform $^{143}Nd/^{144}Nd$

(0.512834−0.512922) and $^{147}Sm/^{144}Nd$ (0.1093−0.1117) ratios, yielding large positive εNd (+3.8 to +5.5) values (Table 4). Depleted mantle model ages range between 338 and 474 Ma. Like Sr and Nd isotopes, Pb isotopes also display very narrow variations ($^{206}Pb/^{204}Pb$=19.40−19.58; $^{207}Pb/^{204}Pb$=15.57−15.60; $^{208}Pb/^{204}Pb$=38.99−39.14) (Table 5). Figure 15 compares the Sr, Nd and Pb isotopic compositions of the Tasse alkaline basalts with MORB, OIB, HIMU, and FOZO, and with basalts from various arcs, forearcs, back-arcs and continental flood basalt provinces. On $^{87}Sr/^{86}Sr$ versus $^{143}Nd/^{144}Nd$, $^{206}Pb/^{204}Pb$ versus $^{207}Pb/^{204}Pb$, $^{206}Pb/^{204}Pb$ versus $^{208}Pb/^{204}Pb$, and $^{206}Pb/^{204}Pb$ versus $^{87}Sr/^{86}Sr$ diagrams, the alkaline basalts plot in the OIB field. They also plot close to the FOZO field.

CHAPTER 8
Discussion

8.1 Source characteristics of the mantle xenoliths

The concave-upward LREE patterns of Group 1 xenoliths are similar to those of Phanerozoic boninites and forearc peridotites, reflecting the addition of La, Ce and Pr to a strongly LREE-depleted mantle domain (see Pearce et al., 1992; König et al., 2010). Similarly, Group 1 xenoliths share the super-chondritic Al_2O_3/TiO_2 (32−34) ratios, MORB-normalized negative Nb (0.14−0.34) and Ti (0.84−0.93), and positive Rb, U, K, Pb (4.51−5.12) and Zr (1.37−2.13) anomalies of Phanerozoic boninites (see Pearce et al., 1992; König et al, 2010). These geochemical characteristics are collectively consistent with the enrichment of a highly depleted mantle domain by subduction-derived melts and/or fluids in a sub-arc mantle wedge. Although Group 2 and Group 3 xenoliths share the enrichment of LILE (Rb, Ba, K), LREE, Th, U, Pb, Zr, Hf of Group 1 xenoliths, they have higher abundances of all these elements than Group 1 xenoliths (Fig. 12), suggesting that the sources of Group 2 and Group 3 xenoliths underwent more extensive metasomatic enrichment than the source of Group 1 xenoliths by subduction-derived melts and/or fluids. Different degrees of enrichment in the sources of Groups 1, 2 and 3 xenoliths are consistent with the existence of a heterogeneous mantle domain beneath the Omineca belt (Fig. 4) and differential metasomatic enrichment processes in the sub-arc mantle wedge beneath southeastern British Columbia.

The distinct geochemical characteristics of samples TA-2012-14 and TA-2012-25 are also consistent with heterogeneous mantle domain beneath the Omineca belt. Sample TA-2012-14 is a spinel lherzolite and shows evidence of extensive melt metasomatism modifying clinopyroxene (Fig. 8e-f), resulting in a resorption texture and an LREE-

enriched, U-shaped pattern with mild MREE depletion (Fig. 12d). Sample TA-2012-25 is a dunite and dominated by high LREE and lower HREE typical of LREE-enriched dunitic samples (Fig. 12d). These samples display strong U, K, Pb, P, Zr and Hf anomalies, as well as Th. Negative anomalies are associated with Nb (Ta) and Ti (Fig. 12h).

Mantle xenoliths have been identified globally and in different tectonic environments (Ionov et al., 2006; Arai et al., 2007; Zheng et al., 2007; Lu et al., 2013). It is well known that the Canadian Cordillera has been formed through many periods of accretion due to subduction and arc related tectonism (Gabrielse et al., 1991; Price, 1994; Hart, 1999; Monger and Price, 2002; Eyles and Miall, 2007; Monger, 2014). Ultramafic rocks occurring in different geodynamic settings have distinct rock associations and geochemical signatures (Bodinier and Godard, 2003; Beccaluva et al., 2004; Ishizuka et al, 2014; Khedr et al., 2014). In order to constraint their origin, the geochemistry of the mantle xenoliths in the Canadian Cordillera are compared with those of ultramafic rocks formed in forearcs, ophiolites and orogenic massifs.

8.1.1 Comparison with other Phanerozoic ultramafic rocks

Forearc ultramafic rocks are commonly represented by serpentinized harzburgites and dunites with subordinate pyroxenites and lherzolites (Ishii et al, 1992; Pearce et al., 1992; Parkinson and Pearce, 1998; Pearce et al., 2000; Hyndman and Peacock, 2003; Beccaluva et al., 2004; Ishizuka et al, 2014). Harzburgites and dunites are characteristics of a highly depleted mantle source and have high Mg-numbers (92−94) (Ishiwatari, 1985; Ishii et al., 1992; Artemieva, 2011). Chondrite-normalized patterns indicate strongly

depleted sources (Parkinson and Pearce, 1998), with heavy LREE-depletion and positive incline towards the HREE component, leading to lower MREE/HREE and LREE/HREE values (Fig. 16b). Strong depletion of LREE, relative to HREE, and high Mg-numbers have been attributed to high degrees of partial melting and multiple stages of melt extraction (Ishiwatari, 1985; Ishii et al., 1992; Pearce et al., 2000; Artemieva, 2011).

Ophiolites are representative sections of oceanic lithosphere (crust and upper mantle) that have been accreted to the continental lithosphere (Bodinier and Godard, 2003; Metcalf and Shervais, 2008; Pearce, 2008; Dilek and Furnes, 2014; Furnes et al., 2014, 2015; Pearce, 2014). Many major orogenic belts, such as the Himalayan, Appalachian, Altaids, and Alpine orogenic belts, contain numerous ophiolite complexes (Bodinier and Godard, 2003; Şengör and Natal'in, 2004; Eyuboglu et al., 2007; Hanghøj et al., 2010; Dilek and Furnes, 2011, 2014; Uysal et al., 2012; Santosh et al., 2013; Khedr et al., 2014, Pearce, 2014). The ultramafic basal section of ophiolites may contain lherzolitic (Internal Ligurides, Western Alps) and/or harzburgitic (Semail ophiolite, Oman) rock types (Bodinier and Godard, 2003; Hanghøj et al., 2010; Dilek and Furnes, 2014). Most ophiolites do not have the complete rock association as defined in the Penrose Conference in 1972 (Anonymous, 1972), as their mantle section tend to be fragmented and destroyed during their accretion (Kusky, 2004; Dilek and Furnes, 2011, 2014; Furnes et al., 2014, 2015). Ophiolitic lherzolites are more commonly distinguished by 'N-MORB' type patterns, demonstrated by LREE-depletion in chondrite-normalized plots (Fig. 16b) (Bodinier and Godard, 2003; Hanghøj et al., 2010; Khedr et al., 2014). Similar to harzburgites, ophiolitic lherzolites occasionally exhibit minor to moderate

positive slope towards the HREE, which differs from the 'N-MORB' type flat MREE to HREE patterns (Fig. 16b) (Bodinier and Godard, 2003; Khedr et al., 2014).

Orogenic peridotite massifs are characterized by a predominance of lherzolites with minor harzburgites and dunites (Bodinier and Godard, 2003). Contrasting with ophiolitic peridotites, orogenic massifs do not show specific structural sequences (Bodinier and Godard, 2003). Orogenic massifs are representative of fertile mantle (>10% clinopyroxene) and commonly dominated by spinel peridotites of intermediate pressure (Bodinier and Godard, 2003). Petrologically and geothermobarometrically orogenic massifs are divided into three types: (1) high-(ultra-high)-pressure (garnet-bearing) peridotites, (2) intermediate pressure (spinel-bearing) peridotites, and (3) low pressure (plagioclase-bearing) peridotites (Bodinier and Godard, 2003). Serpentinized massifs are of low pressure within the plagioclase stability field and have been known to show evidence of recrystallization within the lower pressure environment (Bodinier and Godard, 2003).

The major element composition of the Tasse lherzolites is comparable to other spinel lherzolites from various localities in British Columbia (Fig. 16b) (Peslier et al., 2002; Francis et al., 2010; Greenfield et al., 2013). Similarly, the lherzolites studied by Peslier et al. (2002) are akin to the Tasse xenoliths, by showing distinctive groupings of LREE-depleted and moderately to more strongly LREE-enriched (Figs 12 and 16). Lherzolites reported by Peslier et al. (2002) show negative Zr, Hf, Ti, Nb, Ta anomalies and are variable in LILE. The negative Zr and Hf anomalies are not common with the Tasse suite, which may be due to heterogeneity in source composition or metasomatism. The LREE enrichment factors also differ. The most depleted lherzolites studied by Peslier

et al. (2002) show no LREE enrichment compared to the Tasse Group 1 lherzolites (Fig. 16b). The sources of LREE enrichment may be attributed to metasomatism by either melt or subduction fluids and are variable in extent. The Tasse xenoliths are representative of pieces of a variably metasomatized sub-arc mantle emplaced by alkaline basalt upwelling.

The major difference between the Tasse mantle xenoliths and ultramafic rocks from a forearc setting, ophiolites and massif peridotite is that the latter rocks are strongly serpentinized. In contrast to the dry nature of the Tasse mantle xenoliths (LOI <1 wt.%), ultramafic rocks from forearc settings, ophiolites and massif peridotites are strongly hydrated (LOI >8 wt.%).

Forearc harzburgites and dunites (Parkinson and Pearce, 1998) contain notable geochemical differences compared with the Tasse xenoliths. Izu–Bonin–Mariana forearc samples contain higher MgO and lower Fe_2O_3, CaO, Al_2O_3 and Na_2O values. Distinctively lower Zr (<0.3 ppm) and greater Ni (2400–3100 ppm) values are also notable compared with the Tasse lherzolites (Table 1). Along with Zr, other HFSE, and Th and U are more enriched in the Tasse xenoliths. Both the Tasse and Izu–Bonin–Mariana xenoliths show comparable fluctuations in LILE (e.g., K, Rb, Sr, Ba), as seen in many arc environments (Pearce et al., 2000; Arai et al., 2007; Ishizuka et al., 2014). Chondritic Y/Ho (~28) and sub- to superchondritic Nb/Th values (2–13) are representative of the Tasse xenoliths. Izu-Bonin-Mariana forearc samples display larger variation in Y/Ho (15–35) and subchondritic Nb/Th (1–5). The Tasse xenoliths represent a less depleted source with less alteration and notably there is an absence of harzburgites and serpentinization (serpentine minerals; e.g., antigorite, chrysotile).

The most depleted Tasse xenoliths (Group 1), show higher LREE (La/Sm_{cn}=0.48−1.16) and enriched HREE (Gd/Yb_{cn}=0.71−0.92) patterns compared with ophiolitic lherzolites (La/Sm_{cn}=0.29–0.78 and Gd/Yb_{cn}=0.27–0.65) (Khedr et al., 2014). Ophiolites, similar to forearc settings, represent a more depleted source than is seen in the Tasse suites, although geochemical similarities are notable. Both ophiolitic and Tasse lherzolites contain similar MgO (43–46 wt.%) and CaO (2.0–3.7 wt.%) content. The Tasse lherzolites contain higher TiO_2, Al_2O_3, Fe_2O_3 and Na_2O compared with ophiolites. Ophiolitic xenoliths contain similar Cr and slightly lower V and Ni contents. The greater variability of Eu/Eu^*_{cn} in ophiolitic lherzolites is not seen in the Tasse xenoliths (Eu/Eu^*_{cn}= avg. 1.01).

Studies from China have shown an abundance of mantle xenoliths present, brought to the surface by both basaltic rocks and kimberlites (Menzies et al., 1993; Wang et al., 1998; Wu et al., 2003, 2006; Xu et al., 2003; Chu et al., 2009). The majority of mantle xenoliths found throughout China are spinel lherzolites, harzburgites, dunites, wehrlites and pyroxenites (Wu et al., 2003, 2006; Xu et al., 2003; Chu et al., 2009). Garnet-bearing xenoliths are also present and are more commonly sampled by kimberlites from deeper mantle sources (Menzies et al., 1993; Wang et al., 1998; Chu et al., 2009). Lherzolites found within China share the major and trace element characteristics of the Tasse xenolith suite (see Chu et al., 2009). The more refractory dunites and harzburgites from the Mengyin kimberlites show evidence of LREE-enrichment (Chu et al., 2009), as the dunite sample from the Tasse suite. Spinel lherzolites hosted by the Penglai basalts exhibit similar enrichment patterns to the Group 2 and Group 3 spinel lherzolites of the Tasse suite (Chu et al., 2009). The trace element patterns indicate variable metasomatic

enrichment throughout the lithospheric mantle beneath China (Menzies et al., 1993; Wang et al., 1998; Wu et al., 2003, 2006; Xu et al., 2003; Chu et al., 2009). Mineralogically, mantle xenolith samples from China show evidence of both melt and hydrous metasomatism (Wu et al., 2003, 2006; Xu et al., 2003; Chu et al., 2009). Evidence of hydrous metasomatism is supported by the presence of phlogopite-, amphibole- and apatite-bearing mantle peridotites (Xu et al., 2003; Wu et al., 2006), which differs from the Tasse suite wherein no hydrous minerals have been recognized.

The Tasse xenoliths more closely resemble orogenic spinel lherzolites of the Lanzo and Lherz massifs (Le Roux et al., 2007; Riches and Rogers, 2011; Guarnieri et al., 2012). Field relationships of the Tasse xenoliths did not exhibit any particular structure or patterns. The xenoliths appeared as nodules or massif bodies emplaced within the alkaline basalts. Geochemically ophiolites and orogenic massifs share similarities; however, the LREE patterns of the Tasse lherzolites are more representative of the orogenic Lherz lherzolites showing elevated signatures and a moderate incline towards the HREE (Riches and Rogers, 2011; Khedr et al., 2014). Major element signatures and Mg-numbers compared with the orogenic North Lanzo spinel lherzolites (Guarnieri et al., 2012) are virtually identical. Cardinal differences include Fe_2O_3, HFSE, Th and U which are higher in the Tasse xenoliths. The elevated abundance in the aforementioned elements can be attributed to arc processes. There are no distinctive differences amid Y/Ho values (28) or Eu/Eu^*_{cn} (~1.0).

8.2 The petrogenetic origin of the Tasse alkaline lavas

The Tasse basalts are uniform in composition. They have La/Sm_{cn} (3.15–3.80), Gd/Yb_{cn} (3.42–4.61), Zr/Y (13–14), Nb/Y (2.6–3.0) and Th/Yb (3.04–3.80) ratios (Table 2), and high alkaline element (e.g., Na_2O, K_2O, Rb) contents, consistent with an incompatible-element enriched mantle source. The trace element systematics suggests a homogeneous mantle source or homogenized magma chamber(s). Negative Ti anomalies (0.80–0.96) may have resulted from a Ti-bearing mineral fractionation, possibly ilmenite or magnetite, as they are common accessory minerals in mafic rocks (see Barnes and Roeder, 2001). Eu/Eu* values are constant; and average 1.01, indicating that plagioclase was not a major fractionating phase.

The alkaline lavas are Cenozoic and scattered throughout British Columbia (Brearley et al., 1984; Carr, 1995; Sun and Kerrich, 1995; Peslier et al., 2002; Abraham et al., 2005; Sluggett, 2008; Kuehn et al., 2015). The origin of the alkaline basalts is attributed to partial melting of an enriched mantle source by either metasomatism or crustal contamination (Wilshire et al, 1980; Wilshire et al., 1988). Considering the metasomatic nature of the mantle xenoliths, the partial melting of an enriched mantle source model is highly probable, although the aforementioned models remain heavily debated. Kuehn et al. (2015) attributed the origin of alkaline basalts in the Satah Mountain and Baldface Mountain volcanic fields to a hot spot beneath central British Columbia.

On $^{87}Sr/^{86}Sr$ versus $^{143}Nd/^{144}Nd$, $^{206}Pb/^{204}Pb$ versus $^{87}Sr/^{86}Sr$, $^{206}Pb/^{204}Pb$ versus $^{207}Pb/^{204}Pb$, and $^{206}Pb/^{204}Pb$ versus $^{208}Pb/^{204}Pb$ diagrams, the Tasse alkaline basalts plot in the OIB field, and are located between MORB and FOZO fields, consistent with an

asthenospheric mantle source (Fig. 15). They plot away from the Turkish-Iranian Plateau, the Andean southern Volcanic Zone, the Izu-Bonin forearc, the Kuril arc, the Aleutian arc and the Scotia Ridge basalts on the Sr−Nd−Pb isotope diagrams (Fig. 15), suggesting that they are not derived from a subduction- modified mantle source.

The following trace element and Sr−Nd−Pb isotope characteristics are inconsistent with significant crustal contamination of the Tasse alkaline basalts: (1) La/Nb (0.68–0.73); (2) low Th/Nb_{cn} (0.61–0.72); (3) low Al_2O_3/TiO_2 (4.6–5.7); (4) Eu/Eu* (avg. 1.02); (5) Nb/Nb* (avg. 1.06); (6) large positive εNd (+3.8 to +5.5) values; and (7) low $^{87}Sr/^{86}Sr$ values (0.703346−0.703591) (Tables 2-4) (cf., Taylor and McLennan, 1995; Hofmann, 1997; Polat et al., 1997; Rudnick and Gao, 2003; Kamgang et al., 2008; Yanagi, 2011; Li et al., 2014).

8.2.1 Comparison with other Cenozoic alkaline lavas

Cenozoic alkaline magmatism was not only common in British Columbia but also widespread globally (Wilshire et al., 1988; Polat et al., 1997; Colgan et al., 2006; Camp and Hanan, 2008; Hidas et al., 2010; Nkouandou and Temdjim, 2011; Putirka and Platt, 2012; Camp et al., 2013). Many of these alkaline basaltic lavas (e.g., Argentina, Cameroon, China, Hungary, Oman) host mantle xenoliths (Chen et al., 2007, 2014; Dantas et al., 2009; Grégoire et al., 2009; Hidas et al., 2010; Nkouandou and Temdjim, 2011; Liu et al., 2012; Li et al., 2014).

The Tasse alkaline lavas in British Columbia share many geochemical characteristics of the Cenozoic alkaline lavas erupted in different parts of the world (Chen et al., 2007; Dantas et al., 2009; Grégoire et al., 2009; Hidas et al., 2010; Nkouandou and

Temdjim, 2011; Liu et al., 2012; Li et al., 2014). Nkouandou and Temdjim (2011) studied the geochemistry of both spinel lherzolite and alkaline lavas associated with the Adamawa Massif, Cameroon Line, Cameroon, Africa. The basaltic flows in the region are of alkaline to peralkaline nature and appear to have been derived by low degrees of partial melting (1−2%) from a FOZO-mantle source at approximately 80 km depth, leaving a residual garnet source (Nkouandou and Temdjim, 2011). Chondrite-normalized REE patterns (Fig. 17c) of the Cameroon Line basalts are similar to those of the Tasse alkaline lavas. N-MORB multi-element patterns (Fig. 18c) of the Cameroon Line basalts show differences with highly negative K and P (sample C-10) anomalies. The Cameroon Line samples show two distinct trace element patterns with NG-130 more closely resembling characteristics of the Tasse basalts. Positive Ba, Ta and Zr are shared between both Cameroon Line and Tasse samples (Figs. 17c and 18c).

The Bohai Bay Basin, northeast China, contains >1 km thick, compositionally uniform alkaline basaltic flows displaying several eruption cycles (Li et al., 2014). On N-MORB-normalized diagrams, these flows display positive Nb anomalies as well, negative Th, U, Sm and Hf anomalies (Fig. 18b) (Li et al., 2014). The basaltic flows each contain specific signatures that appear to be unrelated to continental input or metasomatic reaction due to low Th and Nb (Rudnick and Gao, 2003; Li et al., 2014) and positive Nb and Ta anomalies, respectively (Fig. 18b). The basaltic flows are ascribed to lithospheric thinning to thickening throughout the eruption cycles (Li et al., 2014).

All three Bohai Basin basalt sequences contain similar Al_2O_3 and lower Fe_2O_3 and alkali (K_2O+Na_2O) content than the Tasse basalts. The Guantao group contains lower MgO and higher SiO_2 content than the other two basaltic series of the Bohai Bay Basin

and Tasse samples. The Guantao group also shares similar Zr/Y (11−16) ratios as the Tasse basalts. On N-MORB multi-element plots Tasse alkaline basalts show positive anomalies in Ba, Sr and Zr with variable Ti negative anomalies most comparable to the Guantao group basalts from the Bohai Bay Basin. The Tasse basalts do not show large Nb anomalies as seen in the Bohai Basin basalts. All three Bohai Basin bay basalt suites are slightly less enriched in LREE and MREE than the Tasse basalts (Fig. 17b).

Quaternary basalts studied by Polat et al. (1997) in Turkey, contain two suites of alkaline basalts, Ceyhan-Osmaniye plain basalts (COPB) and Hassa graben basalts (HGB). The two suites of basalts originated from a metasomatized asthenospheric source, show OIB characteristics and are associated with the East Anatolian and Dead Sea fault zones. The COPB basalt can be further subdivided into two groupings, but overall they contain similar SiO_2, Al_2O_3, higher CaO and lower Fe_2O_3 and alkali (K_2O+Na_2O) content than the Tasse basalts. Group 1 COPB contain higher Zr/Y (~10) values than those of Group 2 (Zr/Y = 6.5-7.6). HGB have comparable TiO_2, Al_2O_3, MgO and CaO contents with higher alkali (K_2O+Na_2O) and lower Fe_2O_3 contents in contrast to Tasse basalts. Neither the COPB nor HGB share similar Zr/Y ratios to the Tasse xenoliths. Both COPB and HGB basalts show less LREE enrichment compared with the Tasse basalts (Fig. 17c), with HGB being significantly lower. The COPB and HGB sequences contain positive Ti anomalies which differ from the Tasse basalts (Fig. 18c). Positive Ba, Sr and Zr and negative Sm anomalies are seen amongst all basalt sequences (Fig. 18c).

Alkaline lavas in many of these locations share some geochemical similarities to the Tasse alkaline basalts but originated in differing tectonic settings. The Tasse alkaline basalts are compositionally more akin to those of the Guantao group and NG-130 of the

Cameroon Line, although the degree of source enrichments and geodynamic processes may differ (see Nkouandou and Temdjim, 2011).

The Tasse alkaline basalts possess higher $^{143}Nd/^{144}Nd$ but lower $^{87}Sr/^{86}Sr$ ratios than the Deccan Trap and the Turkish-Iranian Plateau basalts, signifying less interaction with the continental crust (Fig. 15). In addition, the Tasse basalts have higher $^{206}Pb/^{204}Pb$ ratios than basalts in the North Queensland, the Turkish-Iranian Plateau and the Payenia Volcanic Province of the southern Andes (Fig. 15), suggesting higher $^{238}U/^{204}Pb$ values in source of the Tasse basalts than in those of the North Queensland, the Turkish-Iranian Plateau and the Payenia Volcanic Province counterparts.

8.3 Geodynamic constraints on the origins of Cenozoic alkaline lavas in British Columbia

An early framework for the Late Cenozoic volcanism in the Canadian Cordillera was provided by Bevier et al. (1979) and Souther (1991) who divided the region into a series of belts and fields, each with a distinctive rationale such as subduction, extension or mantle plume activity. Since then, numerous studies of the volcanic belts have provided additional information on age and petrogenesis (e.g., Edwards and Russell, 2000; Preece and Hart, 2004; Abraham et al., 2005; Sluggett, 2008; Manthei et al., 2010; Mullen and Weis, 2013; and Kuehn et al., 2015). Studies of subducted slab geometry (Breitsprecher et al., 2003; Madsen et al., 2006) and mantle tomography (Frederiksen et al., 1998; Audet et al., 2008; Mercier et al., 2009; and Bao et al., 2014) have provided additional constraints and insights into the crustal and mantle environments and the processes responsible for the magmatism.

The most fundamental geological elements in the region are the subducted slabs and the intervening Northern Cordilleran Slab Window which divide the region into two volcanic arcs and an intervening field of slab window-associated volcanoes (Thorkelson and Taylor, 1989; Madsen et al., 2006). The slab window-related field is approximately 2000 km long and is characterized by mafic, alkalic compositions with intra-oceanic trace element profiles. Localized magmatism in this field began in the Oligocene, became widespread during the Miocene to Pliocene, and contracted to fewer localities in the Pleistocene and Holocene (Edwards and Russell, 2000). Clearly, the absence of slab beneath this region was a fundamental control on the compositions of the volcanoes, few of which bear supra-subduction zone signatures.

Thorkelson et al. (2011) suggested that diffuse upwelling through the slab window resulted in low-degree decompressional anatexis of both asthenospheric and lithospheric reservoirs and was the primary mechanism of the magmatism. However, the field of intraplate volcanism is both wide and long, and additional causes of magmatism have been proposed and deserve exploration. Focused mantle upwelling in the form of a small plume may have been responsible for the Anahim belt (Souther, 1986; Kuehn et al., 2015), although the younging of volcanism from west to east (Kuehn et al., 2015) is not as consistent as might be expected, the topographic elevation of the region is modest, and tomographically identified slowness anomalies (Audet et al., 2008; Mercier et al. 2009) are not particularly deep or well defined.

Lithospheric extension related to intervals of divergence between the Pacific and North American plates (Edwards and Russell, 2000) has also been proposed and appears to be particularly relevant to the central part of the intraplate field where Neogene graben

development and faulting have been documented (Souther, 1991; Edwards and Russell, 2000). However, many of the intraplate volcanoes are located where no extensional structures have been identified, and the degree of extension within most of the Canadian Cordillera during Miocene and later times appears to be low and unlikely to trigger mantle melting. Nevertheless, localized extensional faulting may have provided conduits for magma that was produced by other means such as upwelling and decompression.

Back-arc style mantle convection and melting behind the Garibaldi arc in southern British Columbia remains as a viable mechanism to form the Chilcotin Group (Bevier et al., 1979). However, these back-arc lavas are broadly similar to those found elsewhere in the intraplate belt, suggesting a common mechanism. Appealing solely to mantle stirring by the subducting Juan de Fuca slab for these lavas may be problematic, however, because the Chilcotin Group extends northward beyond the modeled extent of subducted slab of the Juan de Fuca plate and merges with the so-called Anahim hot-spot track. The back-arc model for this area, however, is strongly supported by the geophysical modeling of Currie and Hyndman et al. (2006) who invoked small-domain mantle convection within the asthenosphere behind the arc. That model may be broadly applicable to magmatism and high heat flow in southern British Columbia, but appears to be unable to account for Miocene to Holocene volcanism in the central and northern parts of the intraplate belt which have not lain behind a volcanic arc since the Paleogene (Madsen et al., 2006). Moreover, some of the magmatism and high heat flow in southern British Columbia may be related to tears and breaches in the downgoing slab (Madsen et al., 2006; Sluggett, 2008; Mullen and Weis, 2013).

Another model for high heat flow and magmatism in the intraplate field is lithospheric delamination and orogenic collapse in the Paleogene (Ranalli et al, 1989; Bao et al., 2014). In this model, delamination removed much of the previously extant lithospheric mantle in the central and western Cordillera, contributing to Paleocene to Eocene magmatism and leaving behind a thin layer of lithospheric mantle. As noted by Francis et al. (2010), the mantle lithosphere appears to have undergone thinning in the Neogene, a process that would require additional thermal erosion, albeit of a mantle lithosphere that may have been catastrophically thinned during the Paleogene.

8.4 Characteristics of the lithospheric mantle beneath southeastern British Columbia

Understanding the origin of the Tasse alkaline basalts and their mantle xenoliths requires the assessment of the degrees of partial melting, source characteristics and the nature of metasomatism associated with subduction and arc generating processes in southeastern British Columbia.

The Tasse mantle xenoliths represent a section of mantle beneath southeastern British Columbia. The major element characteristics of the xenoliths indicate the mantle has emanated from melt extraction of a relatively fertile source (Fig. 19) (Canil and Lee, 2009). Modal clinopyroxene has been used to estimate mantle fertility (Parkinson and Pearce, 1998). The Tasse lherzolites contain ~10−15% clinopyroxene. Depletion of LREEs in the Tasse lherzolites reflects extraction of basaltic melts from their sources (cf., Peslier et al., 2002; Pearce and Stern, 2006). There is no evidence to suggest a single partial melting event and based on subduction and arc forming history of British Columbia, the removal of basaltic partial melts may have occurred over a large time span.

The elevated Mg-numbers are also indicative of a source that underwent various degrees of partial melting (cf., Ishiwatari, 1985; Ishii et al, 1992; Parkinson and Pearce, 2008). Although the Tasse xenolith suite contains only one representative dunite sample, harzburgites have been found in other localities within British Columbia (Peslier et al., 2002; Greenfield et al., 2013). These more refractory mantle xenoliths typically contain higher Mg-numbers stemming from high degrees of partial melting (see Ishiwatari, 1985; Ishii et al, 1992). The lherzolites within the Tasse property contain rather restricted Mg-numbers (90). The dunite sample from the Tasse location has the highest Mg-number (92) indicating a larger degree of partial melting from the initial fertile source (Figs. 19 and 20). The semi-quantitative model produced by Ishiwatari (1985), using Mg-numbers and major element oxides (wt.%) illustrates the relative degrees of melting in ultramafic rocks. When the Tasse samples are plotted, it shows that the lherzolites have undergone 10−15% partial melting, while the dunite sample resembles those for forearc dunite and harzburgites (see Ishii et al., 1992), which indicate higher degrees of partial melting, 25−30% (Fig. 20). The 10−15% degrees of partial melting are consistent with the Peslier et al. (2002) model for Cr-diopside bearing lherzolites from other localities within British Columbia.

Th-REE-LILE-HFSE (e.g., Th/Yb, Th/Nb, La/Nb, La/Sm) ratios are commonly used to assess the subduction zone geochemistry, given that Th, LREE and LILE tend to be mobilized whereas HFSE are predominantly immobile during slab-dehydration processes (Pearce and Parkinson, 1993; Pearce and Peate, 1995; Zack and John, 2007; Pearce, 2008, 2014; König et al., 2010; Shervais and Jean, 2012). Chondritic values of coupled HFSE ratios, such as Nb/Ta and Zr/Hf, have been used for assessing source

characteristics and petrogenetic processes (Jochum et al., 1989). The mantle xenoliths sampled during this study show subchondritic to superchondritic values for Y/Ho and Nb/Ta, while Zr/Hf chondritic values tend to be superchondritic (Fig. 11; Table 1). The spread seen in Zr/Hf and Nb/Ta may in part be due to metasomatic processes, fractionation effects or an increase in element mobility.

It is common for Nb and Ta to substitute into a Ti-bearing phase, such as rutile or ilmenite (see Stolz et al., 1996; Plank, 2005; König et al., 2010; Hui et al., 2011), resulting in depletion of these elements relative to Th, LREE and LILE. The mantle xenoliths do not show any abundance of such phases, which suggests that the Ti-bearing phases may have been retained in the subduction slab. The enrichment of Th and La relative to Nb and Ta by rutile-saturated melts can also generate negative Nb-Ta anomalies as seen in the Tasse xenoliths (see Plank, 2005; König et al., 2010). Island arc rocks are commonly depleted in HFSE, although not necessarily Zr and Hf (see Saunders et al. 1991; Pearce and Peate, 1995). The Sr/Nd values (15±8) of the Tasse suite are similar to global averages (15±5) of other peridotites (Jochum et al., 1989). Island arc basalts have elevated Sr/Nd (30−35) (Jochum et al., 1989). The Sr/Nd values seen in the Tasse suite are more characteristic of MORBs (10−15) and OIBs (14−22).

The LREE-enriched characteristics of the Tasse mantle xenoliths are variable from slight to more strongly enriched samples (Fig. 12). This has also been seen in lherzolite, dunite and harzburgite xenoliths throughout southeastern British Columbia (Brearley and Scarfe, 1984; Brearley et al., 1984; Sun and Kerrich, 1995; Peslier et al., 2002; Greenfield et al., 2013) indicating that metasomatism has likely been prevalent throughout the region.

The nature of the metasomatism is correlated with subduction and arc forming processes. Common forms of metasomatism associated with these environments are typically slab dehydration and melt percolation. The Tasse xenoliths do not contain any hydrous mineral phases, as seen in forearc peridotites (see Ishii et al., 1992; Pearce et al., 1992; Parkinson and Pearce, 1998; Pearce et al., 2000; Hyndman and Peacock, 2003; Ishizuka et al., 2014), commonly associated with serpentinization. One such study, noted earlier by Brearley and Scarfe (1984), did find minor amounts of amphibole in one spinel lherzolite from British Columbia, but it is not commonly present throughout suites of xenoliths studied within British Columbia. It does not appear that hydrous metasomatism is prevalent within the subcontinental lithosphere throughout a large extent beneath southeastern British Columbia.

Numerous studies have attributed mantle metasomatism to silicate and carbonatite melt percolation and interaction with peridotites (see Yaxley et al., 1998; Coltorti et al. 1999; Litasov et al., 2000; Downes, 2001; Dixon et al., 2008; Maruyama et al., 2009; Martin et al., 2014). Coltorti et al. (1999) suggested that carbonatite melt metasomatism results in strong LREE enrichments ($La/Yb_{cn}>3-4$) and various Ti and Zr negative anomalies compared to alkaline-silicate metasomatism. The LREE enrichment, and positive Zr and negative Ti anomalies in the Tasse xenoliths (Figs. 12 and 13) likely reflect carbonatite- or alkaline-melt metasomatism. Although, no petrographic evidence of secondary carbonate phases has been recognized in the Tasse xenoliths, clinopyroxene resorption texture (Fig. 8e-f) might reflect the effect of carbonate metasomatism. However, geochemical evidence: (1) $La/Yb_{cn}<4$; (2) Ti/Eu > 3000; (3) positive Zr anomalies are consistent with alkalic-silicate metasomatism rather than carbonate-melt

metasomatism (Fig. 21) (Coltorti et al. 1999). Clinopyroxene and spinel in the Tasse mantle xenoliths might have formed at the expense of Al-rich orthopyroxene during alkalic-silicate melt peridotite interaction (cf., Kepezhinskas et al., 1995; Coltorti et al. 1999). The alkali-silicate melt metasomatism may in part be related to the percolation of host alkaline basaltic melts. Although the alkaline basaltic rocks only erupted to the surface recently in the Cenozoic (Littlejohn and Greenwood, 1974; Brearley and Scarfe, 1984; Brearley et al., 1984; Sun and Kerrich, 1995; Peslier et al., 2002; Greenfield et al., 2013; Kuehn et al., 2015), the melts may have percolated through the mantle for extended periods of time prior to the eruption of the alkaline basalts.

Re-Os studies of mantle xenoliths in British Columbia by Peslier et al. (2000a, b) have demonstrated that the lithospheric mantle beneath the Omineca and Intermontane belts is likely Precambrian in age. Specifically, the Os isotopic signature of the lherzolites indicates partial melting of the mantle during intervals in the late Mesoproterozoic, broadly at the time of Grenville orogenesis in eastern and southern North America. This interpretation implies continuation of North American subcontinental lithospheric mantle below a large swath of the accreted terranes (Peslier et al., 2000a, b) and is consistent with seismic interpretations that show westward continuation of North American crust under the Omineca and Intermontane belts (Cook et al., 2004). The Re-Os results are also consistent with an emerging realization of modest Grenville-age activity that extends in a belt from the northern Canadian Cordillera to the northwestern conterminous United States (Milidragovic et al. 2011). The interpretation of metasomatic activity in the mantle of the Canadian Cordillera is supported by the studies of Brearley and Scarfe (1984), Brearley et al. (1984) and Sun and Kerrich (1995). Our findings also suggest that the

mantle has undergone various events of partial melting and metasomatism (Figs. 19−21). We are unable to determine if the melting and metasomatism in the Tasse suite occurred during the Precambrian or Phanerozoic, using our current set of data.

Studies of the Lherz massif have shown evidence regarding refertilization of refractory peridotites (harzburgites) producing secondary lherzolites (Le Roux et al., 2007). The formation of the secondary lherzolites was shown by detailed structural mapping and geochemical analysis. Reaction textures at harzburgite-lherzolite contacts suggest refertilization of harzburgite by upwelling asthenospheric partial melts. Our study indicates that melt metasomatism played an important role in the origin of LREE- and LILE-enriched patterns by refertilizing numerous sections of previously depleted lithospheric mantle. This enrichment process is not specific to lherzolites, as harzburgites from British Columbia have also shown metasomatic enrichment (Peslier et al., 2002). Additional petrographic and geochemical studies of mantle xenoliths in southeast British Columbia are needed to better understand the possible refertilization of the mantle and secondary lherzolite formation, as seen in the Lherz massif.

CHAPTER 9
Conclusions

On the basis of new field observations, SEM analyses, and whole-rock major and trace element and Sr−Nd−Pb isotope data, the following petrologic and geodynamic conclusions are drawn for the Tasse alkaline basalts and mantle xenoliths.

1. Distinct geochemical characteristics of the spinel peridotites analyzed for this study, as well as studies conducted by other researchers (e.g., Peslier et al., 2002; Francis et al., 2010; Kuehn et al., 2015) in southern British Columbia provide evidence for upper mantle heterogeneity. The presence of lherzolites, harzburgites and dunites throughout the Omineca and Intermontane belts demonstrate varying degrees of partial melting and metasomatism generating upper mantle heterogeneity. Tasse spinel lherzolites represent residues of 10–15% partial melt depletion and 20–25% partial melt depletion for the dunite sample.
2. The Tasse xenoliths exhibit three distinctive REE patterns reflecting various degrees of metasomatic enrichment in a pre-Miocene sub-arc mantle wedge: (1) Group 1 is characterized by concave-upward LREE patterns; (2) Group 2 displays flat to moderately LREE enriched patterns; and (3) Group 3 is strongly LREE enriched. Two outlier samples exhibit unique patterns indicating further variable degrees of metasomatism. Metasomatism in the source of the xenoliths appears to have stemmed from percolating alkaline-silicate melts. All xenolith samples share positive Th, Rb K, Pb and Zr (Hf) anomalies and negative Nb (Ta) and Ti anomalies on MORB-normalized trace element diagrams, which is consistent with the formation of the

subcontinental lithospheric mantle beneath southern British Columbia above subducted oceanic slabs.

3. The Tasse alkaline basalts are uniform in composition and originated from a well-homogenized asthenospheric mantle source. The alkaline nature (K_2O+Na_2O=5.1−6.6 wt.%), Nb/Y (2.6−3.0) and Zr/Y (13−14) are consistent with an incompatible-element enriched source originating from the garnet stability field.
4. The alkaline basalts have large positive εNd (+3.8 to +5.5) values and 338-426 Ma depleted mantle model ages, suggesting a minimal magma-crust interaction and mantle melting events between the Silurian to Carboniferous. They display narrow ranges of Sr ($^{87}Sr/^{86}Sr$=0.703346−0.703591) and Pb ($^{206}Pb/^{204}Pb$=19.40−19.58; $^{207}Pb/^{204}Pb$=15.57−15.60; $^{208}Pb/^{204}Pb$=38.99−39.14) isotopic ratios, consistent with a homogeneous mantle source. The Tasse basalts are isotopically distinct from continental flood basalts and subduction-related basalts, plotting mainly in the ocean island basalt (OIB) field on Sr−Nd−Pb isotope ratio diagrams.
5. The Neogene intraplate volcanic field was generated by a combination of diffuse mantle upflow through the Northern Cordilleran Slab Window, localized lithospheric extension, slab-induced “back arc” mantle circulation, possible plume activity and localized delamination of cratonic lithospheric mantle.

References

Abraham, A.C., Francis, D., Polvé, M., 2005. Origin of Recent alkaline lavas by lithospheric thinning beneath the northern Canadian Cordillera. Canadian Journal of Earth Sciences 42, 1073-1095.

Anonymous, 1972. Penrose field conference on ophiolites. Geotimes 17, 24-25.

Arai, S., Abe, N., Ishimaru, S., 2007. Mantle peridotites from the Western Pacific. Gondwana Research 11, 180-199.

Artemieva, I., 2011. The Lithosphere: An Interdisciplinary Approach. Cambridge University Press, Cambridge, pp. 794.

Audet, P., Bostock, M. G., Mercier, J.-P., Cassidy, J. F., 2008. Morphology of the Explorer–Juan de Fuca slab edge in northern Cascadia: Imaging plate capture at a ridge-trench-transform triple junction. Geology 36, 895-898.

Bailey, D.K., 1972. Uplift, rifting and magmatism in continental plates. Journal of Earth Sciences 8, 225-239.

Bailey, D.K., 1982. Mantle metasomatism; continuing chemical change within the Earth. Nature, 296, 525-530.

Ballhaus, C., 1993. Redox states of lithospheric and asthenospheric upper mantle. Contributions to Mineralogy and Petrology 114, 331-348.

Bao, X., Eaton, D.W., Guest, B., 2014. Plateau uplift in western Canada caused by lithospheric delamination along a craton edge. Nature Geoscience 7, 830-833.

Barker Minerals Ltd. (http://www.barkerminerals.com)

Barnes, S.J., Roeder, P.L., 2001. The range of spinel compositions in terrestrial mafic and ultramafic rocks. Journal of Petrology 42, 2279-2302.

Beccaluva, L., Coltorti, M., Giunta, G., Siena, F., 2004. Tethyan vs. Cordilleran ophiolites: a reappraisal of distinctive tectono-magmatic features of supra-subduction complexes in relation to the subduction mode. Tectonophysics 393, 163-174.

Bennett, V.C., 2003. Compositional Evolution of the Mantle. In: Treatise on Geochemistry, Volume 2: The Mantle and Core, Carlson, R.W. (ed.), Elsevier, Pergamon, Oxford, pp. 493-519.

Bevier, M.L., Armstrong, R.L., Souther, J.G., 1979. Miocene peralkaline volcanism in west-central British Columbia—Its temporal and plate-tectonics setting. Geology 7, 389-392.

Bodinier, J-L., Godard, M., 2003. Orogenic, Ophiolitic, and Abyssal Peridotites. In: Treatise on Geochemistry, Volume 2: The Mantle and Core, Carlson, R.W. (ed.), Elsevier, Pergamon, Oxford, pp. 61-102.

Brearley, M., Scarfe, C.M., 1984. Amphibole in a spinel lherzolite xenolith: evidence for volatiles and partial melting in the upper mantle beneath southern British Columbia. Canadian Journal of Earth Sciences 21, 1067-1072.

Brearley, M., Scarfe, C.M., Fujii, T., 1984. The petrology of ultramafic xenoliths from Summit Lake, near Prince George, British Columbia. Contributions to Mineralogy and Petrology 88, 53-63.

Breitsprecher, K., Thorkelson, D.J., Groome, W.G., 2003. Geochemical confirmation of the Kula-Farallon slab window beneath the Pacific Northwest in Eocene time. Geology 31, 351-354.

Burnham, O.M., Hechler, J.H., Semenyna, L., Schweyer, J., 2002. Summary of Field Work and Other Activities 2002; Ontario Geological Survey Open File Report 6100. Baker, C.L., Debicki, E.J., Kelly, R.I. and Parker, J.R. (Eds.), Sudbury, Ontario, 36-1-36-12.

Camp, V.E., Hanan, B.B., 2008. A plume-triggered delamination origin for the Columbia River Basalt Group. Geosphere 4, 480-495.

Camp, V.E., Ross, M.E., Duncan, R.A., Jarboe, N.A., Coe, R.S., Hanan, B.B., Johnson, J.A., 2013. The Steens Basalt: Earliest lavas of the Columbia River Basalt Group. In: The Columbia River Flood Basalt Province, Special Paper 497. Reidel, S.P., Camp, V.E., Ross, M.E., Wolff, J.A., Martin, B.S., Tolan, T.L., and Wells, R.E. (Eds.), Geological Society of America, pp. 87-116.

Canil, D., Lee, C.-T., 2009. Were deep cratonic mantle roots hydrated in Archean oceans? Geology 37, 667-670.

Carr, S.D., 1995. The southern Omineca Belt, British Columbia: new perspectives from the Lithoprobe Geoscience Program. Canadian Journal of Earth Sciences 32, 1720-1739.

Chen, Y., Zhang, Y., Graham, D., Su, S., Deng, J., 2007. Geochemistry of Cenozoic basalts and mantle xenoliths in Northeast China. Lithos 96, 108-126.

Chen, M.M., Tian, W., Suzuki, K., Tejada, M.-L.-G. , Liu, F.L., Senda, R., Wei, C.J., Chen, B., Chu, Z.Y., 2014. Peridotite and pyroxenite xenoliths from Tarim, NW China: Evidences for melt depletion and mantle refertilization in the mantle source region of the Tarim flood basalt. Lithos 204, 97-111.

Chin, E.J., Lee, C-T.A., Luffi, P., and Tice, M., 2012. Deep Lithospheric Thickening and Refertilization beneath Continental Arcs: Case Study of the P, T and Compositional Evolution of Peridotite Xenoliths from the Sierra Nevada, California. Journal of Petrology 53, 477-511.

Chu, Z.-Y., Wu, F.-Y., Walker, R.J., Rudnick, R.L., Pitcher, L., Puchtel, I.S., Yang, Y.-H., Wilde, S.A., 2009. Temporal Evolution of the Lithospheric Mantle beneath the Eastern North China Craton. Journal of Petrology 50, 1857-1898.

Colgan, J.P., Dumitru, T.A., McWilliams, M., Miller, E.L., 2006. Timing of Cenozoic volcanism and Basin and Range extension in northwestern Nevada: New constraints from the northern Pine Forest Range. GSA Bulletin 118, 126-139.

Coltorti, M., Bonadiman, C., Hinton, R. W., Siena, F., Upton, B. G. J., 1999. Carbonatite Metasomatism of the Oceanic Upper Mantle: Evidence from Clinopyroxenes and Glasses in Ultramafic Xenoliths of Grande Comore, Indian Ocean. Journal of Petrology 40, 133-165.

Condie, K.C., 2000. Episodic continental growth models: afterthoughts and extensions. Tectonophysics 322, 153-162.

Coney, P.J., Jones, D.L., Monger, J.W.H., 1980. Cordilleran suspect terranes. Nature 288, 329-333.

Cook, F.A., Clowes, R.M., Snyder, D.B. van der Velden, A.J., Hall, K.W., Erdmer, P., Evenchick, C.A., 2004. Precambrian crust beneath the Mesozoic northern Canadian Cordillera discovered by Lithoprobe seismic reflection profiling. Tectonics 23, 1-28.

Currie, C.A., Hyndman, R.D., 2006. The thermal structure of subduction zone back arcs. Journal of Geophysical Research 111, 1-22.

Dantas, C., Grégoire, M., Koester, E., Conceição, R.V., Rieck Jr., N., 2009. The lherzolite-websterite xenolith suite from Northern Patagonia (Argentina): Evidence of mantle-melt reaction processes. Lithos 107, 107-120.

De Hoog, J.C. M., Gall, L., Cornell, D.H., 2010. Trace-element geochemistry of mantle olivine and application to mantle petrogenesis and geothermobarometry. Chemical Geology 270, 196-215.

DePaolo, D.J., 1981. Neodymium isotope geochemistry: An introduction. New York, Springer-Verlag, pp. 187.

Dilek, Y., Furnes, H. 2011. Ophiolite genesis and global tectonics: Geochemical and tectonic fingerprinting of ancient oceanic lithosphere. Geological Society of America Bulletin 123, 387-411.

Dilek, Y., Furnes, H., 2014. Ophiolites and Their Origins. Elements 10, 93-100.

Dixon, J., Clague, D.A., Cousens, B., Monsalve, M.L., Uhl, J., 2008. Carbonatite and silicate melt metasomatism of the mantle surrounding the Hawaiian plume: Evidence from volatiles, trace elements, and radiogenic isotopes in rejuvenated-stage lavas from Niihau, Hawaii. Geochemistry, Geophysics, Geosystems 9, 1-34.

Downes, H., 2001. Formation and modification of the shallow sub-continental lithospheric mantle: a review of geochemical evidence from ultramafic xenolith suites and tectonically emplaced ultramafic massifs of western and central Europe. Journal of Petrology 42, 233-250.

Downes, H., de Vries, C., Wittig, N., 2014. Hf–Zr anomalies in clinopyroxene from mantle xenoliths from France and Poland: implications for Lu–Hf dating of spinel peridotite lithospheric mantle. International Journal of Earth Sciences 104, 89-102.

Edwards, B.R., Russell, J.K., 2000. Distribution, nature, and origin of Neogene–Quaternary magmatism in the northern Cordilleran volcanic province, Canada. GSA Bulletin 112, 1280-1295.

Ewing, T.E., 1980. Paleogene Tectonic Evolution of the Pacific Northwest. The Journal of Geology 88, 619-638.

Eyles, N., Miall, A., 2007. Chapter 8: Building Western Canada. Canada Rocks: The Geologic Journey. Fitzhenry and Whiteside, Markham, ON.

Eyuboglu, Y., Bektas, O., Pul, D., 2007. Mid-Cretaceous Olistostromal Ophiolitic Mélange Developed in the Back-arc Basin of the Eastern Pontide Magmatic Arc, Northeast Turkey. International Geology Review 49, 1103-1126.

Ferri, F., Höy, T., and Friedman, R.M., 1999. Description, U-Pb age and Tectonic Setting of the Quesnel Lake Gneiss, East-central British Columbia. Geological Fieldwork 1998 Report, British Columbia Ministry of Energy and Mines, Victoria, British Columbia, pp. 69-80.

Ferri, F., O'Brien, B.H., 2002. Preliminary Geology of the Cariboo Lake Area, Central British Columbia (093A/11, 12, 13 AND 14). Geological Fieldwork 2001 Report, British Columbia Ministry of Energy and Mines, Victoria, British Columbia, pp. 59-82.

Ferri, F., Schiarizza, P., 2006. Reinterpretation of the Snowshoe Group stratigraphy across a southwest-verging nappe structure and its implications for regional correlations within the Kootenay terrane. In Paleozoic Evolution and Metallogeny of Pericratonic Terranes at the Ancient Pacific Margin of North America, Canadian and Alaskan Cordillera, Special Paper 45. Colpron, M. and Nelson, J. (eds.) Geological Association of Canada (GAC), St. John's, Newfoundland, Canada. pp. 415-432.

Francis, D., Minarik, W., Proenza, Y., Shi, L., 2010. An overview of the Canadian Cordilleran lithospheric mantle. Canadian Journal of Earth Sciences 47, 353-368.

Franz, L., Becker, K-P., Kramer, W., Herzig, P.M., 2002. Metasomatic mantle xenoliths from the Bismarck Microplate (Papua New Guinea) – thermal evolution, geochemistry and extent of slab-induced metasomatism. Journal of Petrology 43, 315-343.

Frederiksen, A.W., Bostock, M.G., VanDecar, J.C., Cassidy, J.F., 1998. Seismic structure of the upper mantle beneath the northern Canadian Cordillera from teleseismic travel-time inversion. Tectonophysics 294, 43-55.

Frei, R., Polat, A., 2013. Chromium isotope fractionation during oxidative weathering – implications from the study of a Paleoproterozoic (ca. 1.9 Ga) paleosol, Schreiber Beach, Ontario, Canada. Precambrian Research 224, 434-453.

Fretzdorff, S., Livermore, R.A., Devey, C.W., Leat, P.T., Stoffers, P., 2002. Petrogenesis of the Back-arc East Scotia Ridge, South Atlantic Ocean. Journal of Petrology 43, 1435-1467.

Furnes, H., de Wit, M., and Dilek, Y., 2014. Four billion years of ophiolites reveal secular trends in oceanic crust formation. Geoscience Frontiers 5, 571-603.

Furnes, H., Dilek, Y., de Wit, M., 2015. Precambrian greenstone sequences represent different ophiolite types. Gondwana Research 27, 649-685.

Gabrielse, H., Monger, J.W.H., Wheeler, J.O. and Yorath, C.J., 1991. Morphogeological belts, tectonic assemblages and terranes. In: Gabrielse, H., Yorath, C.J. (Eds.), Geology of the Cordilleran Orogen in Canada, Geology of Canada no. 4, Chapter 2, Part A, Geological Survey of Canada. Ottawa, Canada, 15-28.

Greenfield, A.M.R., Ghent, E.D., Russell, J.K., 2013. Geothermobarometry of spinel peridotites from southern British Columbia: implications for the thermal conditions in the upper mantle. Canadian Journal of Earth Sciences 50, 1019-1032.

Grégoire, M., Langlade, J.A., Delpech, G., Dantas, C., Ceuleneer, G., 2009. Nature and evolution of the lithospheric mantle beneath the passive margin of East Oman: Evidence from mantle xenoliths sampled by Cenozoic alkaline lavas. Lithos 112, 203-216.

Guarnieri, L., Nakamura, E., Piccardo, G.B., Sakaguchi, C., Shimizu, N., Vannucci, R., Zanetti, A., 2012. Petrology, Trace Element and Sr, Nd, Hf Isotope Geochemistry of the North Lanzo Peridotite Massif (Western Alps, Italy). Journal of Petrology 53, 2259-2306.

Hanghøj, K., Kelemen, P.B., Hassler, D., Godard, M., 2010. Composition and Genesis of Depleted Mantle Peridotites from the Wadi Tayin Massif, Oman Ophiolite; Major and Trace Element Geochemistry, and Os Isotope and PGE Systematics. Journal of Petrology 51, 201-227.

Harder, M., Russell, J.K., 2006. Thermal state of the upper mantle beneath the Northern Cordilleran Volcanic Province (NCVP), British Columbia, Canada. Lithos 87, 1-22.

Hart, C., 1999. The Geological Framework of the Yukon Territory. Department of Energy, Mines and Resources, Yukon Geological Survey, http://www.geology.gov.yk.ca/pdf/bedrock_geology.pdf.

Hidas, K., Guzmics, T., Szabó, C., Kovács, I., Bodnar, R.J., Zajacz, Z., Nédli, Z., Vaccari, L., Perucchi, A., 2010. Coexisting silicate melt inclusions and H2O-bearing, CO2-rich fluid inclusions in mantle peridotite xenoliths from the Carpathian–Pannonian region (central Hungary). Chemical Geology 274, 1-18.

Hofmann, A.W., 1997. Mantle geochemistry: the message from oceanic volcanism. Nature 385: 219-229.

Holm, P.M., Søager, N., Dyhr, C.T., Nielsen, M.R., 2014. Enrichments of the mantle sources beneath the Southern Volcanic Zone (Andes) by fluids and melts derived from abraded upper continental crust. Contributions to Mineralogy and Petrology 167, 1-27.

Horwitz, E.P., Chiarizia, R., Dietz, M.L., 1992. A novel strontium-selective extraction chromatographic resin. Solvent Extraction and Ion Exchange 10, 313-336.

Hui, H., Niu, Y., Zhidan, Z., Huixin, H., Dicheng, Z., 2011. On the Enigma of Nb-Ta and Zr-Hf Fractionation — A Critical Review. Journal of Earth Science 22, 52-66.

Hyndman, R.D., Peacock, S.M., 2003. Serpentinization of the forearc mantle. Earth and Planetary Science Letters 212, 417-432.

Hyndman, R.D., Currie, C.A., Mazzotti, S., Frederiksen, A., 2009. Temperature control of continental lithosphere elastic thickness, Te vs Vs. Earth and Planetary Science Letters 277, 539-548.

Ionov, D.A., Chazot, G., Chauvel, C., Merlet, C., Bodinier, J.-L., 2006. Trace element distribution in peridotite xenoliths from Tok, SE Siberian craton: A record of pervasive, multi-stage metasomatism in shallow refractory mantle. Geochimica et Cosmochimica Acta 70, 1231-1260.

Ishii, T., Robinson, P.T., Maekawa, H. Fiske, R., 1992. Petrological studies of peridotites from diapiric serpentinite seamounts in the Izu-Ogasawara-Mariana Forearc, Leg 125. Proceedings of the Ocean Drilling Program, Scientific Results 125, 445-485.

Ishiwatari, A., 1985. Igneous Petrogenesis of the Yakuno Ophiolite (Japan) in the context of the diversity of ophiolites. Contributions to Mineralogy and Petrology 89, 155-167.

Ishizuka, O., Tani, K., Reagan, M.K., 2014. Izu-Bonin-Mariana Forearc Crust as a Modern Ophiolite Analogue. Elements 10, 115-120.

Jochum, K.P., McDonough, W.F., Palme, H. Spettel, B., 1989. Compositional constraints on the continental lithospheric mantle from trace elements in spinel peridotite xenoliths. Nature 340, 548-550.

Johnston, S.T., 2001. The Great Alaskan Terrane Wreck: reconciliation of paleomagnetic and geological data in the northern Cordillera. Earth and Planetary Science Letters 193, 259-272.

Kamgang, P., Chazot, G., Emmanuel, N., Tchoua, F.M., 2008. Geochemistry and geochronology of mafic rocks from Bamenda Mountains (Cameroon): Source composition and crustal contamination along the Cameroon Volcanic Line. Comptes Rendus Geoscience, 340, 850-857.

Kay, R.W., Gast, P.W., 1973. The rare earth content and origin of alkali-rich basalts. Journal of Geology 81, 653-682.

Kepezhinskas, P.K., Defant, M.J., Drummond, M.S., 1995. Na Metasomatism in the Island-Arc Mantle by Slab Melt-Peridotite Interaction: Evidence from Mantle Xenoliths in the North Kamchatka Arc. Journal of Petrology 36, 1505-1527.

Kerrich, R., Wyman, D., Hollings, P., Polat, A.1999. Variability of Nb/U and Th/La in 3.0 to 2.7 Ga Superior Province ocean plateau basalts: implications for the timing of continental growth and lithosphere recycling. Earth and Planetary Science Letters 168, 101-115.

Khedr, M.Z., Arai, S., Python, M., Tamura, A. 2014. Chemical variations of abyssal peridotites in the central Oman ophiolite: Evidence of oceanic mantle heterogeneity. Gondwana Research 25, 1242-1262.

Kheirkhah, M., Neill, I., Allen, M.B., 2015. Petrogenesis of OIB-like basaltic volcanic rocks in a continental collision zone: Late Cenozoic magmatism of Eastern Iran. Journal of Asian Earth Sciences 106, 19-33.

König, S., Münker, C., Schuth, S., Luguet, A., Hoffmann, J.E., Kuduon, J., 2010. Boninites as windows into trace element mobility in subduction zones. Geochimica et Cosmochimica Acta 74, 684-704.

König, S., Münker, C., Schuth, S., Garbe-Schönberg, D., 2008. Mobility of tungsten in subduction zones. Earth and Planetary Science Letters 274, 82-92.

Kuehn, C., Guest, B., Russel, J.K., Benowitz, J.A., 2015. The Satah Mountain and Baldface Mountain volcanic fields: Pleistocene hot spot volcanism in the Anahim Volcanic Belt, west-central British Columbia, Canada. Bulletin of Volcanology 77, 3-27.

Kuritani, T., Yokoyama, T., Nakamura, E., 2008. Generation of Rear-arc Magmas Induced by Influx of Slab-derived Supercritical Liquids: Implications from Alkali Basalt Lavas from Rishiri Volcano, Kurile Arc. Journal of Petrology 49, 1319-1342.

Kusky, T., 2004. Epilogue: What if anything have we learned about Precambrian ophiolites and early Earth processes? In Precambrian Ophiolites and Related Rocks, Developments in Precambrian Geology, Volume 13, Kusky, T. (ed.) and Condie, K.C. (Series ed.), Elsevier, Amsterdam, pp. 727-737.

Le Roux, V., Bodinier, J.-L., Tommasi, A., Alard, O., Dautria, J.-M., Vauchez, A., Riches, A.J.V., 2007. The Lherz spinel lherzolite: Refertilized rather than pristine mantle. Earth and Planetary Science Letters 259, 599-612.

Li, H-Y., Huang, X-L., Guo, H., 2014. Geochemistry of Cenozoic basalts from the Bohai Bay Basin: Implications for a heterogeneous mantle source and lithospheric evolution beneath the eastern North China Craton. Lithos 196-197, 54-66.

Litasov K.D., Foley S.F., Litasov Y.D., 2000. Magmatic modification and metasomatism of the subcontinental mantle beneath the Vitim volcanic field (East Siberia): evidence from trace element data on pyroxenite and peridotite xenoliths from Miocene picrobasalt. Lithos 54, 83-114.

Littlejohn, A.L., Greenwood, H.J., 1974. Lherzolite Nodules in Basalts from British Columbia, Canada. Canadian Journal of Earth Sciences 11, 1288-1308.

Liu, J., Carlson, R.W., Rudnick, R.L., Walker, R.J., Gao, S., Wu, F-Y., 2012. Comparative Sr-Nd-Hf-Os-Pb isotope systematics of xenolithic peridotites from Yangyuan, North China Craton: Additional evidence for a Paleoproterozoic age. Chemical Geology 332-333, 1-14.

Lu, J., Zheng, J., Griffin, W.L., Yu, C., 2013. Petrology and geochemistry of peridotite xenoliths from the Lianshan region: Nature and evolution of lithospheric mantle beneath the lower Yangtze block. Gondwana Research 23, 161-175.

Madsen, J.K., Thorkelson, D.J., Friedman, R.M., Marshall D.D., 2006. Cenozoic to Recent plate configurations in the Pacific Basin: Ridge subduction and slab window magmatism in western North America. Geosphere 2, 11-34.

Manthei, C.D., Ducea, M.N., Girardi, J.D., Patchett, P.J. Gehrels, G.E., 2010. Isotopic and geochemical evidence for a recent transition in mantle chemistry beneath the western Canadian Cordillera. Journal of Geophysical Research 115, 1-19.

Martin, A.P., Price, R.C., Cooper, A.F., 2014. Constraints on the composition, source and petrogenesis of plagioclase-bearing mantle peridotite. Earth-Science Reviews 138, 89-101.

Maruyama, S., Hasegawa, A., Santosh, M., Kogiso, T., Omori, S., Nakamura, H., Kawai, K., Zhao, D., 2009. The dynamics of big mantle wedge, magma factory and metamorphic-metasomatic factory in subduction zones. Gondwana Research 16, 414-430.

Maury, R.C., Defant, M.J., Joron, J-L., 1992. Metasomatism of the sub-arc mantle inferred from trace elements in Philippine xenoliths. Nature 360, 661-663.

McCulloch, M.T., 1993. The role of subducted slabs in an evolving Earth. Earth and Planetary Science Letters 115, 89-100.

McCulloch, M.T., Bennett, V.C., 1994. Progressive growth of the Earth's continental crust and depleted mantle: Geochemical constraints. Geochimica et Cosmochimica Acta 58, 4717-4738.

McDonough, W.F., Sun, S.-S., 1995. The composition of the Earth. Chemical Geology, 120: 223-253.

Menzies, M.A., Fan, W., Zhang, M., 1993. Palaeozoic and Cenozoic lithoprobe and the loss of >120 km of Archean lithosphere, Sino-Korean craton, China. In Magmatic Processes and Plate Tectonics, Special Publication 76, Prichard, H.M., Alabaster, T., Harris, N.B.W., Neary, C.R. (eds.), Geological Society. pp. 71-81.

Mercier, J-C. C., Nicolas, A., 1975. Textures and Fabrics of Upper-Mantle Peridotites as Illustrated by Xenoliths from Basalts. Journal of Petrology 16, 454-487.

Mercier, J.-P., Bostock, M.G., Cassidy, J.F., Dueker, K., Gaherty, J.B., Garnero, E.J., Revenaugh, J., Zandt, G., 2009. Body-wave tomography of western Canada. Tectonophysics 475, 480-492.

Metcalf, R.V., Shervais, J.W., 2008. Suprasubduction-zone ophiolites: Is there really an ophiolite conundrum? In Ophiolites, Arcs, and Batholiths: A Tribute to Cliff Hopson, Special Paper 438, Wright, J.E. and Shervais, J.W. (eds.), Geological Society of America. pp. 191-222.

Milidragovic, D., Thorkelson, D.J., Davis, W.J., Marshall, D.D., Gibson, H.D., 2011. Evidence for late Mesoproterozoic tectonism in northern Yukon and the identification of a Grenville-age tectonothermal belt in western Laurentia. Terra Nova 23, 307-313.

Monger, J., 2014. Seeking the Suture: The Coast-Cascade Conundrum. Geoscience Canada, 41, 379-398.

Monger, J., Price, R., 2002. The Canadian Cordillera: Geology and Tectonic Evolution. CSEG Recorder, Feb: 17-36.

Monger, J., Price, R.A., Tempelman-Kluit, D.J., 1982. Tectonic accretion and the origin of the two major metamorphic and plutonic welts in the Canadian Cordillera. Geology 10, 70-75.

Mullen, E.K., Weis, D., 2013. Sr-Nd-Hf-Pb isotope and trace element evidence for the origin of alkalic basalts in the Garibaldi Belt, northern Cascade arc. Geochemistry, Geophysics, Geosystems 14, 3126-3155.

Nelson, J., Colpron, M., 2007. Tectonics and metallogeny of the British Columbia, Yukon and Alaskan Cordillera, 1.8 Ga to the present, in Goodfellow, W.D., ed., Mineral Deposits of Canada: A Synthesis of Major Deposit-Types, District Metallogeny, the Evolution of Geological Provinces, and Exploration Methods: Geological Association of Canada, Mineral Deposits Division, Special Publication 5, 755-791.

Nkouandou, O.F., Temdjim, R., 2011. Petrology of spinel lherzolite xenoliths and host basaltic lava from Ngao Voglar volcano, Adamawa Massif (Cameroon Volcanic Line, West Africa): equilibrium conditions and mantle characteristics. Journal of Geosciences 56, 375-387.

Parkinson, I.J., Pearce, J.A., 1998. Peridotites from the Izu–Bonin–Mariana Forearc (ODP Leg 125): Evidence for Mantle Melting and Melt–Mantle Interaction in a Supra-Subduction Zone Setting. Journal of Petrology 39, 1577-1618.

Parkinson, I.J., Arculus, R.J. and Eggins, S.M., 2003. Peridotite xenoliths from Grenada, Lesser Antilles Island Arc. Contributions to Mineralogy and Petrology 146, 241-262.

Parrish, R., Carr, S.D., Parkinson, D.L., 1988, Eocene extensional tectonics and geochronology of the southern Omineca Belt, British Columbia and Washington, Tectonics 7, 181-212.

Pearce, J.A., 2008. Geochemical fingerprinting of oceanic basalts with applications to ophiolite classification and the search for Archean oceanic crust. Lithos 100, 14-48.

Pearce, J.A., 2014. Immobile Element Fingerprinting of Ophiolites. Elements 10, 101-108.

Pearce, J.A., Barker, P.F., Edwards, S.J., Parkinson, I.J., Leat, P.T., 2000. Geochemistry and tectonic significance of peridotites from the South Sandwich arc-basin system, South Atlantic. Contributions to Mineralogy and Petrology 139, 36-53.

Pearce, J.A., van der Laan, S.R., Arculus, R.J., Murton, B.J., Ishii, T., Peate, D.W., Parkinson, I.J., 1992. Boninite and harzburgite from Leg 125 (Bonin-Mariana forearc): A case study of magma genesis during the initial stages of subduction. Proceedings of the Ocean Drilling Program, Scientific Results 125, 623-659.

Pearce, J.A., Peate, D.W., 1995. Tectonic implications of the composition of volcanic arc magmas. Annual Review of Earth and Planetary Sciences 23, 251-285.

Pearce, J.A., Parkinson, I.J., 1993. Trace element models for mantle melting to volcanic arc petrogenesis. In: Prichard, H.M., Alabaster, T., Harris, N.B.W, Neary, C.R. (eds.), Magmatic Processes and Plate Tectonics. Geological Society Special Publication 76, 373-403.

Pearce, J.A., Stern, R.J., 2006. Origin of Back-Arc Basin Magmas: Trace Element and Isotope Perspectives. In: Christie, D.M., Fisher, C.R., Lee, S-M., Givens, S., (eds.), Back-Arc Spreading Systems: Geological, Biological, Chemical, and Physical Interactions, American Geophysical Union, Washington, DC. pp. 63-86.

Peng, Z.X., Mahoney, J.J., Vanderkluysen, L., Hooper, P.R., 2014. Sr, Nd and Pb isotopic and chemical compositions of central Deccan Traps lavas and relation to southwestern Deccan stratigraphy. Journal of Asian Earth Sciences 84, 83-94.

Peslier, A.H., Reisberg, L., Ludden, J., Francis, D., 2000a. Os isotopic systematics in mantle xenoliths; age constraints on the Canadian Cordillera lithosphere. Chemical Geology 166, 85-101.

Peslier, A.H., Reisberg, L., Ludden, J., Francis, D., 2000b. Re-Os constraints on harzburgite and lherzolite formation in the lithospheric mantle: A study of Northern Canadian Cordillera xenoliths. Geochimica et Cosmochimica Acta 64, 3061-3071.

Peslier, A.H., Francis, D., Ludden, J., 2002. The Lithospheric Mantle beneath Continental Margins: Melting and Melt-Rock Reaction in Canadian Cordillera Xenoliths. Journal of Petrology 43, 2013-2047.

Plank, T., 2005. Constraints from Thorium/Lanthanum on Sediment Recycling at Subduction Zones and the Evolution of the Continents. Journal of Petrology 46, 921-944.

Polat, A., Kerrich, R., Casey, J.F., 1997. Geochemistry of Quaternary basalts erupted along the East Anatolian and Dead Sea Fault zones of southern Turkey: implications for mantle sources. Lithos 40, 55-68.

Preece, S.J., Hart, W.K., 2004. Geochemical variations in the <5 Ma Wrangell Volcanic Field, Alaska: implications for the magmatic and tectonic development of a complex continental arc system. Tectonophysics 392, 165-191.

Price, R.A., 1994. Cordilleran tectonics and the evolution of the Western Canada sedimentary basin: In Chapter 2 of Geological Atlas of Western Canada, Mossop, G.D., Shetsen I. (eds.), Canadian Society of Petroleum Geologists, Calgary, Alberta, pp. 13-24.

Putirka, K., 1999. Melting depths and mantle heterogeneity beneath Hawaii and the East Pacific Rise: Constraints from Na/Ti and rare earth element ratios. Journal of Geophysical Research 104, 2817-2829.

Putirka, K., Platt, B., 2012. Basin and Range volcanism as a passive response to extensional tectonics. Geosphere 8, 1274-1285.

Ranalli, G., Brown, R.L., Bosdachin, R., 1989. A geodynamic model for extension in the Shuswap core complex, southeastern Canadian Cordillera. Canadian Journal of Earth Sciences 26, 1647-1653.

Riches, A.J.V., Rogers, N.W., 2011. Mineralogical and geochemical constraints on the shallow origin, ancient veining, and multi-stage modification of the Lherz peridotite. Geochimica et Cosmochimica Acta 75, 6160-6182.

Rudnick, R.L., Gao, S, 2003. Composition of the continental crust. In: Rudnick, R.L. (ed.), Treatise on Geochemistry, Volume 3: The Crust, Elsevier. Pergamon, Oxford. pp. 1-64.

Santosh, M., Shaji, E., Tsunogae, T., Ram Mohan, M., Satyanarayanan, M., Horie, K., 2013. Suprasubduction zone ophiolite from Agali hill: Petrology, zircon SHRIMP U–Pb geochronology, geochemistry and implications for Neoarchean plate tectonics in southern India. Precambrian Research 231, 301-324.

Saunders, A.D., Norry, M.J. and Tarney, J., 1991. Fluid influence on the trace element compositions of subduction zone magmas. Philosophical Transactions of the Royal Society of London A. 335, 377-392.

Şengör, A.M.C., Natal'in, B.A., 2004. Phanerozoic analogues of Archaean oceanic basement fragments: Altaid ophiolites and ophirags. In Precambrian Ophiolites and Related Rocks, Developments in Precambrian Geology, Vol. 13, Kusky, Timothy (ed.) and Condie, Kent C. (Series ed.), Elsevier, Amsterdam, pp. 675-726.

Shervais, J.W., Jean, M.M., 2012. Inside the subduction factory: Modeling fluid mobile element enrichment in the mantle wedge above a subduction zone. Geochimica et Cosmochimica Acta 95, 270-285.

Shi, L., Francis, D., Ludden, J., Frederiksen, A., Bostock, M., 1998. Xenolith evidence for lithospheric melting above anomalously hot mantle under the northern Canadian Cordillera. Contributions to Mineralogy and Petrology 131, 39-53.

Shirey, S.B., Richardson, S.H., 2011. Start of the Wilson Cycle at 3 Ga Shown by Diamonds from Subcontinental Mantle. Science 333, 434-436.

Singer, B.S., Jicha, B.R., Leeman, W.P., Rogers, N.W., Thirlwall, M.F., Ryan, J., Nicolaysen, K.E., 2007. Along-strike trace element and isotopic variation in Aleutian Island arc basalt: Subduction melts sediments and dehydrates serpentine. Journal of Geophysical Research 112, 1-26.

Sluggett, C.L., 2008. Quaternary alkaline and calc-alkaline basalts in southern British Columbia: mixed signals from mantle sources above the southern edge of the Juan de Fuca-Pacific slab window. M.Sc. Thesis, Department of Earth Sciences, Simon Fraser University, British Columbia.

Søager, N., Holm, P.M., Thirlwall, M.F., 2015. Sr, Nd, Pb and Hf isotopic constraints on mantle sources and crustal contaminants in the Payenia volcanic province, Argentina. Lithos 212-215, 368-378.

Souther, J.G., 1986. The western Anahim Belt: root zone of a peralkaline magma system. Canadian Journal of Earth Sciences 23, 895-908.

Souther, J.G., 1991. Chapter 14 Volcanic regimes. In: Gabrielse, H.,Yorath, C.J. (Eds.), Geology of the Cordilleran Orogen in Canada, Geology of Canada no. 4, Geological Survey of Canada. Ottawa, Canada, 457-490.

Stolz, A. J., Jochum, K.P., Spettel, B., Hofmann, A.W., 1996. Fluid- and melt-related enrichment in the subarc mantle: Evidence from Nb/Ta variations in island-arc basalts. Geology 24: 587-590.

Stracke, A., Hofmann, A.W., Hart, S.R., 2005. FOZO, HIMU, and the rest of the mantle zoo. Geochemistry, Geophysics, Geosystems 6, 1-20.

Struik, L.C., 1986. Imbricated terranes of the Cariboo gold belt with correlations and implications for tectonics in southeastern British Columbia. Canadian Journal of Earth Sciences 23, 1047-1061.

Sun, M., Kerrich, R., 1995. Rare earth element and high field strength element characteristics of whole rocks and mineral separates of ultramafic nodules in Cenozoic volcanic vents of southeastern British Columbia, Canada. Geochimica et Cosmochimica Acta 59, 4863-4879.

Sun, S.S., McDonough, W.F., 1989. Chemical and isotopic systematics of oceanic basalts: implications for mantle composition and processes. In: Saunders A.D., Norry, M. J. (Eds.), Magmatism in the Ocean Basins. Society of London, Special Publications 42, 313-345.

Tang, Y-J., Zhang, H-F., Ying, J-F., Su, B-X., 2013. Widespread refertilization of cratonic and circum-cratonic lithospheric mantle. Earth-Science Reviews 118, 45-68.

Taylor, S.R., McLennan, S.M., 1995. The Geochemical Evolution of the Continental Crust. Reviews of Geophysics 32, 241-265.

Thomas, M.D., 2009. Geological Significance of New Aeromagnetic Data from the Quesnel Survey Area (Portions of NTS 93G E Half and 93H W Half), Central British Columbia: A Mountain Pine Beetle Program Contribution. Geological Survey of Canada, Open File 6225, Ottawa, Ontario.

Thorkelson, D.J., Madsen, J.K., Sluggett, C.L., 2011. Mantle flow through the Northern Cordilleran slab window revealed by volcanic geochemistry. Geology 39, 267-270.

Thorkelson, D.J., Taylor, R.P., 1989. Cordilleran slab windows. Geology 17, 833-836.

Todt, W., Cliff, R.A., Hanser, A., Hofmann, A.W., 1993. Re-calibration of NBS lead standards using 202Pb + 205Pb double spike. Terra Abstract 5, 396.

Uysal, I., Ersoy, E.Y., Karslı, O., Dilek, Y., Sadıklar, M.B. , Ottley, C.J., Tiepolo, M., Meisel, T., 2012. Coexistence of abyssal and ultra-depleted SSZ type mantle peridotites in a Neo-Tethyan Ophiolite in SW Turkey: Constraints from mineral composition, whole-rock geochemistry (major–trace–REE–PGE), and Re–Os isotope systematics. Lithos 132-133, 50-69.

Wang,W., Takahashi, E., Sueno, S., 1998. Geochemical properties of lithospheric mantle beneath the Sino-Korea craton; evidence from garnet xenocrysts and diamond inclusions. Physics of the Earth and Planetary Interiors 107, 249-260.

Wang, Q., Wyman, D., Zhao, Z-H., Xu, J-F., Bai, Z-H., Xiong, X-L., Dai, T.-M., Li, C-F., Chu, Z-Y., 2007. Petrogenesis of Carboniferous adakites and Nb-enriched arc basalts in the Alataw area, northern Tianshan Range (western China): Implications for Phanerozoic crustal growth in the Central Asia orogenic belt. Chemical Geology 236, 42-64.

Webb, S.A.C., Wood, B.J., 1986. Spinel-pyroxene-garnet relationships and their dependence on Cr/Al ratio. Contributions to Mineralogy and Petrology 92, 471-480.

Wilshire, H.G., Meyer, C.E., Nakata, J.K., Calk, L.C., Shervais, J.W., Nielson, J.E., Schwarzman, E.C., 1988. Mafic and ultramafic xenoliths from volcanic rocks of the western United States. USGS Professional Paper 1443, Department of the Interior, Washington, DC, pp. 179.

Wilshire, H.G., Pike, J.E.N., Meyer, C.E., Schwarzman, E.C., 1980. Amphibole-rich veins in lherzolite xenoliths, Dish Hill and Deadman Lake, California. American Journal of Science, 280-A, Part 2, 576-593.

Wu, F.-Y., Walker, R.J., Ren, X.-W., Sun, D.-Y., Zhou, X.-H., 2003. Osmium isotopic constraints on the age of lithospheric mantle beneath northeastern China. Chemical Geology 196, 107-129.

Wu, F.-Y., Walker, R.J., Yang, Y.-H., Yuan, H.-L., Yang, J.-H., 2006. The chemical-temporal evolution of lithospheric mantle underlying the North China Craton. Geochimica et Cosmochimica Acta 70, 5013-5034.

Wyman, D., Kerrich, R., 2010. Mantle plume – volcanic arc interaction: consequences for magmatism, metallogeny, and cratonization in the Abitibi and Wawa subprovinces, Canada. Canadian Journal of Earth Sciences 47, 565-589.

Xu, X., O'Reilly, S.Y., Griffin, W.L., Zhou, X., 2003. Enrichment of upper mantle peridotite: petrological, trace element and isotopic evidence in xenoliths from SE China. Chemical Geology 198, 163-188.

Yanagi**,** T., 2011. Chemical Composition of Continental Crust and the Primitive Mantle. Chapter 2 In Arc Volcano of Japan: Generation of Continental Crust from the Mantle. Berlin, New York, Springer Science and Business Media, pp. 9-17.

Yaxley, G.M., Green, D.H. and Kamenetsky, V., 1998. Carbonatite Metasomatism in the Southeastern Australian Lithosphere. Journal of Petrology 39, 1917-1930.

Zack, T., John, T., 2007. An evaluation of reactive fluid flow and trace element mobility in subducting slabs. Chemical Geology 239, 199-216.

Zhang, M., Stephenson, P.J., O'Reilly, S.Y., McCulloch, M.T., Norman, M., 2001. Petrogenesis and Geodynamic Implications of Late Cenozoic Basalts in North Queensland, Australia: Trace-element and Sr–Nd–Pb Isotope Evidence. Journal of Petrology 42, 685-719.

Zheng, J.P., Griffin, W.L., O'Reilly, S.Y., Yu, C.M., Zhang, H.F., Pearson, N., Zhang, M., 2007. Mechanism and timing of lithospheric modification and replacement beneath the eastern North China Craton: Peridotitic xenoliths from the 100 Ma Fuxin basalts and a regional synthesis. Geochimica et Cosmochimica Acta 71, 5203-5225.

Table 1. Whole-rock major (wt.%) and trace (ppm) element concentrations and significant element ratios for the mantle xenoliths.

	Group 1				
	TA-2012-1	TA-2012-3	TA-2012-8	TA-2012-16	TA-2012-R4
SiO_2	43.4	44.1	45.1	42.8	45.0
TiO_2	0.106	0.093	0.049	0.075	0.125
Al_2O_3	3.42	3.18	2.8	2.55	4.03
Fe_2O_3	8.66	9.04	8.63	9.02	8.65
MnO	0.13	0.13	0.13	0.13	0.13
MgO	39.7	41.2	42.0	41.6	39.1
CaO	2.97	2.9	1.99	2.35	3.51
K_2O	0.02	0.01	0.01	0.02	0.01
Na_2O	0.28	0.27	0.16	0.23	0.32
P_2O_5	0.03	0.02	< 0.01	0.01	0.01
LOI	-0.57	-0.62	-0.56	-0.55	-0.52
Total	98.2	100.3	100.2	98.2	100.3
Mg #	90.1	90.0	90.6	90.1	89.9
Cr	2450	2664	3502	2509	2574
Co	107	109	111	118	101
Ni	1997	2056	2119	2208	1864
Rb	0.56	0.34	0.34	0.38	0.19
Sr	7.7	5.8	3.2	5.5	5.7
Ba	5.2	2.8	2	3.2	2.4
Sc	12.2	14.8	13.2	9.2	10.6
V	73	73	62	89	87
Nb	0.22	0.101	0.186	0.199	0.138
Ta	0.007				0.008
Zr	8	10	6	8	
Hf	0.22	0.29	0.15	0.19	0.17
Th	0.06	0.05	0.02	0.03	<0.018
U	0.04	0.03	0.02	0.02	0.02
Y	2.86	3.04	1.57	2.33	3.31
La	0.35	0.19	0.18	0.23	0.19
Ce	0.55	0.46	0.38	0.45	0.41
Pr	0.08	0.08	0.06	0.06	0.10

Table 1. Continued.

	Group 1				
	TA-2012-1	TA-2012-3	TA-2012-8	TA-2012-16	TA-2012-R4
Nd	0.49	0.49	0.32	0.40	0.57
Sm	0.20	0.22	0.09	0.16	0.26
Eu	0.09	0.08	0.04	0.07	0.11
Gd	0.35	0.34	0.17	0.27	0.43
Tb	0.07	0.07	0.03	0.05	0.08
Dy	0.46	0.51	0.24	0.39	0.56
Ho	0.11	0.11	0.06	0.09	0.13
Er	0.33	0.34	0.18	0.26	0.38
Tm	0.05	0.05	0.03	0.04	0.06
Yb	0.33	0.33	0.20	0.27	0.38
Lu	0.05	0.05	0.03	0.04	0.06
Cu	12.4	8.7	11.5	13.2	22.7
Zn	50	54	54	53	53
Ga	3.04	3	2.51	2.53	3.21
Pb	0.2	0.2	0.2	0.2	<0.18
La/Sm_{cn}	1.16	0.56	1.31	0.93	0.48
La/Yb_{cn}	0.77	0.41	0.66	0.60	0.36
Gd/Yb_{cn}	0.90	0.84	0.71	0.82	0.92
Eu/Eu^*_{cn}	0.99	0.95	1.09	1.00	0.99
Ce/Ce^*_{cn}	0.82	0.91	0.92	0.91	0.74
Al_2O_3/TiO_2	32	34	57	34	32
CaO/Al_2O_3	0.87	0.91	0.71	0.92	0.87
Nb/Ta	31				17
Zr/Hf	36	34	40	42	
Pb/Pb^*_{MORB}	10	11	14	12	
Nb/Nb^*_{MORB}	0.19	0.14	0.34	0.23	0.28
Zr/Zr^*_{MORB}	1.37	1.62	2.13	1.70	
Ti/Ti^*_{MORB}	0.93	0.84	0.87	0.84	0.89

MORB: Normal Mid-Ocean Ridge Basalt; cn: Chondrite. Pb/Pb* values were calculated relative to Ce and Pr. Nb/Nb* values were calculated relative to U and K. Zr/Zr* values were calculated relative to Sm and Eu. Ti/Ti* values were calculated relative to Eu and Gd.

Table 1. Continued.

	Group 2				
	TA-2012-6	TA-2012-13	TA-2012-18	TA-2012-19	TA-2012-45
SiO_2	44.7	44.7	43.4	43.6	44.7
TiO_2	0.123	0.113	0.101	0.11	0.117
Al_2O_3	3.69	3.35	3.25	3.13	3.61
Fe_2O_3	8.77	8.9	8.67	9.5	9.01
MnO	0.13	0.13	0.12	0.14	0.13
MgO	39.3	40.8	40.2	39.4	40.5
CaO	3.31	2.73	2.88	2.34	2.85
K_2O	0.06	0.03	0.04	0.01	0.01
Na_2O	0.36	0.27	0.33	0.23	0.27
P_2O_5	0.01	0.02	0.01	0.04	0.02
LOI	-0.58	-0.6	-0.53	-0.58	-0.61
Total	99.9	100.5	98.5	97.9	100.6
Mg #	89.9	90.1	90.2	89.1	89.9
Cr	2665	2709	3275	2845	2615
Co	107	106	107	108	106
Ni	2019	1970	2030	1915	1962
Rb	1	0.62	0.58	0.31	0.33
Sr	12	16.4	14.6	14.5	17
Ba	6.9	4.2	3.4	1.9	3.9
Sc	16.4	14.1	11.4	14.9	13.5
V	76	80	86	83	74
Nb	0.755	0.632	0.463	0.552	0.562
Ta	0.039	0.04	0.022	0.037	0.029
Zr	9	12	10	14	11
Hf	0.26	0.28	0.25	0.34	0.26
Th	0.06	0.09	0.06	0.07	0.07
U	0.03	0.04	0.03	0.03	0.03
Y	3.35	2.87	2.84	2.63	2.94
La	0.47	0.67	0.53	0.76	0.72
Ce	1.18	1.48	1.13	1.79	1.43
Pr	0.17	0.20	0.15	0.26	0.21

Table 1. Continued.

	Group 2				
	TA-2012-6	TA-2012-13	TA-2012-18	TA-2012-19	TA-2012-45
Nd	0.77	0.83	0.67	1.15	0.97
Sm	0.27	0.25	0.23	0.32	0.28
Eu	0.12	0.10	0.09	0.11	0.11
Gd	0.42	0.36	0.36	0.38	0.39
Tb	0.08	0.06	0.07	0.07	0.07
Dy	0.55	0.46	0.48	0.46	0.50
Ho	0.12	0.10	0.10	0.09	0.10
Er	0.39	0.30	0.31	0.29	0.33
Tm	0.06	0.04	0.04	0.04	0.05
Yb	0.39	0.32	0.30	0.29	0.32
Lu	0.06	0.05	0.05	0.05	0.05
Cu	10.9	16.3	8.6	8.8	12.1
Zn	53	52	57	65	55
Ga	3.29	3.16	3.09	3.21	3.25
Pb	0.2	0.4		0.2	
La/Sm_{cn}	1.14	1.77	1.51	1.56	1.66
La/Yb_{cn}	0.87	1.50	1.27	1.88	1.64
Gd/Yb_{cn}	0.89	0.92	0.98	1.09	1.03
Eu/Eu^*_{cn}	1.09	1.04	0.99	1.01	1.01
Ce/Ce^*_{cn}	1.03	1.00	0.99	0.99	0.90
Al_2O_3/TiO_2	30	30	32	28	31
CaO/Al_2O_3	0.90	0.81	0.89	0.75	0.79
Nb/Ta	19	16	21	15	19
Zr/Hf	35	43	40	41	42
Pb/Pb^*_{MORB}	5	8		3	
Nb/Nb^*_{MORB}	0.44	0.44	0.32	0.84	0.89
Zr/Zr^*_{MORB}	1.12	1.69	1.54	1.64	1.39
Ti/Ti^*_{MORB}	0.85	0.91	0.85	0.81	0.87

Table 1. Continued.

	Group 2			
	TA-2012-46	TA-2012-49	TA-2012-56	TA-2012-62
SiO_2	43.7	43.7	45.2	43.5
TiO_2	0.107	0.1	0.15	0.078
Al_2O_3	2.89	3.25	4.61	2.52
Fe_2O_3	8.96	9.17	9.36	8.86
MnO	0.13	0.13	0.14	0.13
MgO	41.0	40.8	37.5	41.4
CaO	2.58	2.76	3.77	2
K_2O	0.01	0.02	0.02	0.01
Na_2O	0.25	0.29	0.39	0.2
P_2O_5	0.01	0.03	0.02	0.01
LOI	-0.61	-0.58	-0.57	-0.6
Total	99.1	99.7	100.6	98.1
Mg #	90.1	89.8	88.8	90.2
Cr	2593	2312	2936	2347
Co	106	104	98	110
Ni	1953	1901	1814	2054
Rb	0.56	0.33	0.5	0.27
Sr	19.1	9.8	18.5	11.9
Ba	6.5	3.9	3.5	3.5
Sc	12.5	10.4	8.6	10.8
V	72	71	88	66
Nb	0.316	0.346	0.606	0.511
Ta	0.01	0.02	0.046	0.029
Zr	9	8	14	9
Hf	0.24	0.22	0.34	0.21
Th	0.04	0.12	0.11	0.04
U	0.03	0.04	0.04	0.02
Y	2.56	2.74	3.49	1.83
La	0.68	0.52	0.87	0.44
Ce	0.96	1.02	2.07	1.02
Pr	0.15	0.13	0.28	0.14

Table 1. Continued.

	Group 2			
	TA-2012-46	TA-2012-49	TA-2012-56	TA-2012-62
Nd	0.74	0.63	1.32	0.64
Sm	0.23	0.23	0.39	0.17
Eu	0.09	0.09	0.14	0.07
Gd	0.33	0.34	0.51	0.25
Tb	0.06	0.06	0.09	0.04
Dy	0.43	0.47	0.67	0.30
Ho	0.10	0.10	0.14	0.06
Er	0.29	0.32	0.43	0.21
Tm	0.04	0.05	0.06	0.03
Yb	0.28	0.32	0.40	0.22
Lu	0.04	0.05	0.06	0.03
Cu	11.9	14	15.4	7.7
Zn	52	52	66	50
Ga	2.85	2.8	3.8	2.32
Pb		0.2	0.2	
La/Sm_{cn}	1.92	1.47	1.44	1.71
La/Yb_{cn}	1.73	1.17	1.58	1.42
Gd/Yb_{cn}	0.97	0.87	1.07	0.94
Eu/Eu^*_{cn}	0.99	1.01	0.96	1.05
Ce/Ce^*_{cn}	0.74	0.95	1.02	1.01
Al_2O_3/TiO_2	27	33	31	32
CaO/Al_2O_3	0.89	0.85	0.82	0.79
Nb/Ta	32	17	13	18
Zr/Hf	38	36	41	43
Pb/Pb^*_{MORB}		6	3	
Nb/Nb^*_{MORB}	0.45	0.30	0.54	0.90
Zr/Zr^*_{MORB}	1.39	1.22	1.33	1.85
Ti/Ti^*_{MORB}	0.95	0.87	0.86	0.90

Table 1. Continued.

	Group 3			
	TA-2012-2	TA-2012-10	TA-2012-15	TA-2012-44
SiO_2	44.5	44.6	44.3	45.1
TiO_2	0.135	0.143	0.159	0.121
Al_2O_3	3.11	3.84	3.33	3.82
Fe_2O_3	9.05	8.69	9.72	8.69
MnO	0.13	0.13	0.14	0.13
MgO	40.8	39.0	40.0	39.5
CaO	2.45	3.11	2.78	3.17
K_2O	0.02	0.03	0.04	0.03
Na_2O	0.27	0.32	0.34	0.35
P_2O_5	0.05	0.02	0.02	0.02
LOI	-0.59	-0.55	-0.59	-0.55
Total	99.9	99.3	100.3	100.3
Mg #	89.9	89.9	89.1	90.0
Cr	2239	2981	2486	2647
Co	107	105	110	101
Ni	2002	1881	2027	1875
Rb	0.42	0.66	0.69	0.78
Sr	18.3	21.3	31.1	25.2
Ba	4.9	11.4	6	8.8
Sc	12.2	16.7	13.4	14.7
V	60	95	84	77
Nb	0.549	1.061	0.813	0.958
Ta	0.041	0.055	0.059	0.064
Zr	13	14	21	14
Hf	0.37	0.34	0.47	0.34
Th	0.04	0.18	0.10	0.11
U	0.02	0.06	0.03	0.04
Y	2.75	3.45	3.17	3.24
La	1.04	1.25	1.51	1.26
Ce	2.92	2.37	3.79	2.55
Pr	0.43	0.30	0.51	0.32

Table 1. Continued.

	Group 3			
	TA-2012-2	TA-2012-10	TA-2012-15	TA-2012-44
Nd	1.82	1.30	2.16	1.35
Sm	0.44	0.33	0.51	0.33
Eu	0.15	0.13	0.18	0.13
Gd	0.47	0.48	0.54	0.43
Tb	0.08	0.09	0.09	0.08
Dy	0.49	0.57	0.58	0.53
Ho	0.10	0.12	0.12	0.11
Er	0.29	0.39	0.37	0.35
Tm	0.04	0.06	0.05	0.05
Yb	0.29	0.37	0.36	0.35
Lu	0.05	0.06	0.05	0.06
Cu	5.6	13.8	9.8	17.3
Zn	54	57	57	53
Ga	3.46	3.9	3.89	3.36
Pb	0.2	0.3		
La/Sm_{cn}	1.53	2.42	1.90	2.45
La/Yb_{cn}	2.55	2.42	3.04	2.58
Gd/Yb_{cn}	1.32	1.07	1.26	1.00
Eu/Eu^*_{cn}	1.03	1.03	1.04	1.04
Ce/Ce^*_{cn}	1.08	0.95	1.06	0.98
Al_2O_3/TiO_2	23	27	21	32
CaO/Al_2O_3	0.79	0.81	0.83	0.83
Nb/Ta	13	19	14	15
Zr/Hf	35	41	45	41
Pb/Pb^*_{MORB}	2	4		
Nb/Nb^*_{MORB}	0.63	0.62	0.58	0.74
Zr/Zr^*_{MORB}	1.11	1.46	1.53	1.51
Ti/Ti^*_{MORB}	0.77	0.86	0.78	0.79

Table 1. Continued.

	Group 3		Outliers	
	TA-2012-48	TA-2012-55	TA-2012-14	TA-2012-25
SiO_2	44.3	44.3	43.6	43.0
TiO_2	0.125	0.099	0.033	0.017
Al_2O_3	3.54	2.97	2.37	0.85
Fe_2O_3	9.31	9.48	8.78	8.18
MnO	0.14	0.14	0.13	0.12
MgO	39.9	41.4	42.7	47.1
CaO	2.92	2.31	2.12	0.61
K_2O	0.03	0.03	0.07	0.03
Na_2O	0.32	0.26	0.26	0.11
P_2O_5	0.02	0.02	0.04	0.03
LOI	-0.62	-0.64	-0.6	-0.57
Total	100.0	100.3	99.5	99.5
Mg #	89.5	89.6	90.6	91.9
Cr	2586	2384	2899	2931
Co	102	112	111	122
Ni	1927	2078	2141	2505
Rb	0.63	0.52	1.24	0.76
Sr	25.8	16.2	13.9	11.5
Ba	8	3.1	10.3	2.8
Sc	13.8	6.3	12.9	7.5
V	78	64	72	41
Nb	1.058	0.485	0.486	0.309
Ta	0.069	0.033	0.035	0.021
Zr	14	11	11	9
Hf	0.3	0.27	0.21	0.15
Th	0.09	0.04	0.20	0.11
U	0.03	0.02	0.06	0.03
Y	3.32	2.31	1.29	0.44
La	1.54	0.85	0.7	1.03
Ce	3.72	2.27	1.17	1.83
Pr	0.51	0.34	0.10	0.18

Table 1. Continued.

	Group 3		Outliers	
	TA-2012-48	TA-2012-55	TA-2012-14	TA-2012-25
Nd	2.09	1.49	0.34	0.66
Sm	0.46	0.34	0.08	0.10
Eu	0.16	0.12	0.03	0.03
Gd	0.50	0.39	0.12	0.09
Tb	0.08	0.06	0.02	0.01
Dy	0.57	0.43	0.19	0.07
Ho	0.12	0.09	0.05	0.01
Er	0.37	0.28	0.14	0.05
Tm	0.05	0.04	0.02	0.01
Yb	0.35	0.26	0.18	0.05
Lu	0.05	0.04	0.03	0.01
Cu	8.7	12.6	9	4.4
Zn	64	65	52	51
Ga	3.34	2.7	2.15	1.14
Pb		0.2	0.2	0.2
La/Sm_{cn}	2.17	1.60	5.65	6.65
La/Yb_{cn}	3.17	2.33	2.81	15.08
Gd/Yb_{cn}	1.19	1.23	0.55	1.57
Eu/Eu^*_{cn}	0.99	1.03	1.02	1.11
Ce/Ce^*_{cn}	1.03	1.04	1.08	1.03
Al_2O_3/TiO_2	28	30	72	50
CaO/Al_2O_3	0.82	0.78	0.89	0.72
Nb/Ta	15	15	14	15
Zr/Hf	47	41	52	60
Pb/Pb^*_{MORB}		2	6	4
Nb/Nb^*_{MORB}	0.83	0.50	0.18	0.25
Zr/Zr^*_{MORB}	1.16	1.18	4.78	3.37
Ti/Ti^*_{MORB}	0.68	0.69	0.81	0.46

Table 2. Whole-rock major (wt.%) and trace (ppm) element concentrations and significant element ratios for the alkaline basalts.

	TA-2012-26	TA-2012-27	TA-2012-29	TA-2012-30	TA-2012-31
SiO_2	45.8	45.4	45.5	45.3	45.2
TiO_2	2.55	2.56	2.62	2.53	2.57
Al_2O_3	13.4	14.2	13.8	13.6	13.7
Fe_2O_3	14.3	14.4	14.2	14.0	14.2
MnO	0.19	0.19	0.19	0.19	0.19
MgO	10.24	9.27	9.39	9.59	9.53
CaO	7.82	7.85	7.73	7.65	7.77
K_2O	1.71	1.74	1.69	1.74	1.72
Na_2O	3.97	4.22	4.05	4.15	4.14
P_2O_5	0.8	0.82	0.81	0.82	0.8
LOI	-0.29	-0.64	-0.29	-0.62	-0.57
Total	100.5	100	99.69	98.99	99.22
Mg #	58.7	56.1	56.6	57.5	57.1
Cr	387	338	345	377	357
Co	53	51	51	51	49
Ni	318	263	276	289	276
Rb	37	38	39	37	36
Sr	933	907	906	882	881
Cs	0.46	0.53	0.60	0.55	0.54
Ba	719	734	755	732	737
Sc	16	15	15	14	15
V	161	157	152	146	146
Nb	71	72	72	71	71
Ta	4.07	4.09	4.09	4.09	4.10
Zr	328	324	324	319	317
Hf	6.81	6.79	6.83	6.67	6.81
Th	5.75	5.92	6.03	5.90	5.94
U	1.61	1.65	1.69	1.68	1.68
Y	26	25	25	25	24
La	49	51	52	51	51
Ce	99	101	104	102	101
Pr	12	12	12	12	12

Table 2. Continued.

	TA-2012-26	TA-2012-27	TA-2012-29	TA-2012-30	TA-2012-31
Nd	46	48	49	48	49
Sm	8.84	8.97	9.17	8.86	9.07
Eu	2.77	2.86	2.88	2.83	2.81
Gd	7.34	7.65	7.74	7.54	7.66
Tb	0.97	1.02	1.04	1.02	1.01
Dy	5.35	5.63	5.55	5.48	5.42
Ho	0.91	0.95	0.94	0.94	0.94
Er	2.37	2.37	2.39	2.38	2.37
Tm	0.29	0.30	0.30	0.30	0.30
Yb	1.75	1.75	1.79	1.75	1.77
Lu	0.24	0.24	0.25	0.24	0.24
Cu	41	41	40	39	39
Zn	122	119	120	116	116
Ga	22	21	21	21	21
Pb	3.2	3.1	3.2	3.1	3.1
La/Sm_{cn}	3.61	3.68	3.67	3.74	3.64
La/Yb_{cn}	20.3	21.0	20.9	21.0	20.7
Gd/Yb_{cn}	3.47	3.62	3.57	3.56	3.58
Eu/Eu^*_{cn}	1.05	1.05	1.04	1.06	1.03
Ce/Ce^*_{cn}	1.00	1.00	1.00	1.00	0.99
Al_2O_3/TiO_2	5.3	5.6	5.3	5.4	5.3
K_2O+Na_2O	5.7	6.0	5.7	5.9	5.9
Zr/Y	12.8	12.9	12.9	12.8	13.0
Nb/Y	2.8	2.9	2.9	2.9	2.9
Nb/Ta	17	18	18	17	17
Zr/Hf	48	48	47	48	47
Y/Ho	28	26	27	26	26
Pb/Pb^*_{MORB}	1.0	0.9	0.9	0.9	0.9
Nb/Nb^*_{MORB}	1.07	1.06	1.07	1.04	1.04
Zr/Zr^*_{MORB}	1.47	1.42	1.40	1.41	1.39
Ti/Ti^*_{MORB}	0.86	0.84	0.85	0.84	0.85

MORB: Normal Mid-Ocean Ridge Basalt; cn: Chondrite. Pb/Pb* values were calculated relative to Ce and Pr. Nb/Nb* values were calculated relative to U and K. Zr/Zr* values were calculated relative to Sm and Eu. Ti/Ti* values were calculated relative to Eu and Gd.

Table 2. Continued.

	TA-2012-33	TA-2012-34	TA-2012-35	TA-2012-37	TA-2012-38
SiO_2	45.5	45.4	45.1	45.7	46.0
TiO_2	2.59	2.54	2.56	2.70	2.54
Al_2O_3	13.6	13.6	13.4	14.2	13.4
Fe_2O_3	14.1	14.3	14.0	14.6	14.2
MnO	0.19	0.19	0.19	0.19	0.19
MgO	9.59	9.84	9.35	7.99	9.84
CaO	7.76	7.75	7.81	8.01	7.88
K_2O	1.69	1.7	1.7	1.91	1.78
Na_2O	4.03	3.99	4.1	4.32	4.16
P_2O_5	0.82	0.78	0.8	0.9	0.8
LOI	-0.4	-0.52	-0.66	-0.38	-0.62
Total	99.43	99.52	98.27	100.1	100.3
Mg #	57.3	57.7	56.9	52.1	57.8
Cr	340	354	363	260	408
Co	49	51	52	47	51
Ni	275	301	281	198	289
Rb	36	36	37	40	37
Sr	880	883	886	965	878
Cs	0.46	0.54	0.52	0.48	0.50
Ba	723	716	725	797	714
Sc	14	15	16	14	15
V	148	152	161	151	152
Nb	70	69	70	76	69
Ta	4.08	3.96	3.98	4.33	4.02
Zr	314	309	315	342	312
Hf	6.75	6.63	6.66	7.20	6.64
Th	5.92	5.73	5.70	6.40	5.63
U	1.67	1.60	1.68	1.69	1.57
Y	24	24	25	26	25
La	51	50	50	55	49
Ce	99	99	100	110	99
Pr	12	12	12	13	12

Table 2. Continued.

	TA-2012-33	TA-2012-34	TA-2012-35	TA-2012-37	TA-2012-38
Nd	47	47	48	53	47
Sm	8.90	8.80	8.89	9.57	8.84
Eu	2.88	2.79	2.84	3.01	2.79
Gd	7.54	7.38	7.66	7.94	7.27
Tb	1.03	1.00	1.02	1.06	0.99
Dy	5.43	5.34	5.47	5.74	5.35
Ho	0.92	0.92	0.94	0.98	0.92
Er	2.35	2.29	2.38	2.47	2.36
Tm	0.30	0.29	0.30	0.31	0.29
Yb	1.74	1.72	1.73	1.85	1.72
Lu	0.25	0.24	0.24	0.26	0.24
Cu	37	34	40	38	39
Zn	115	115	117	122	123
Ga	20	21	21	22	20
Pb	3.1	3	3.1	3.4	3
La/Sm_{cn}	3.69	3.65	3.66	3.72	3.61
La/Yb_{cn}	21.1	20.7	20.9	21.4	20.6
Gd/Yb_{cn}	3.60	3.54	3.67	3.56	3.49
Eu/Eu^*_{cn}	1.07	1.06	1.05	1.06	1.06
Ce/Ce^*_{cn}	0.98	0.99	0.99	1.00	1.00
Al_2O_3/TiO_2	5.2	5.4	5.2	5.3	5.3
K_2O+Na_2O	5.7	5.7	5.8	6.2	5.9
Zr/Y	12.8	12.9	12.8	13.1	12.6
Nb/Y	2.9	2.9	2.8	2.9	2.8
Nb/Ta	17	17	18	18	17
Zr/Hf	47	47	47	48	47
Y/Ho	27	26	26	27	27
Pb/Pb^*_{MORB}	0.9	0.9	0.9	0.9	0.9
Nb/Nb^*_{MORB}	1.04	1.05	1.03	1.07	1.04
Zr/Zr^*_{MORB}	1.37	1.38	1.39	1.41	1.39
Ti/Ti^*_{MORB}	0.85	0.86	0.84	0.84	0.86

Table 2. Continued.

	TA-2012-39	TA-2012-41	TA-2012-42	TA-2012-43	TA-2012-47
SiO_2	45.7	44.6	44.7	45.4	45.2
TiO_2	2.59	2.60	2.48	2.55	2.55
Al_2O_3	14.3	13.6	13.6	13.9	13.8
Fe_2O_3	14.5	14.1	13.7	14.1	13.9
MnO	0.19	0.19	0.19	0.20	0.19
MgO	9.27	9.41	8.51	8.57	8.25
CaO	7.84	8.09	7.89	7.71	7.68
K_2O	1.81	1.73	1.89	1.91	1.91
Na_2O	4.11	3.72	3.97	4.4	4.42
P_2O_5	0.81	0.83	0.9	0.91	0.91
LOI	-0.48	0.56	0.56	-0.41	-0.43
Total	100.6	99.38	98.42	99.21	98.4
Mg #	55.9	57.0	55.1	54.7	54.1
Cr	343	364	299	307	288
Co	50	50	48	48	46
Ni	267	268	233	231	213
Rb	39	38	43	42	42
Sr	890	876	928	948	962
Cs	0.48	0.54	0.60	0.58	0.57
Ba	739	726	778	794	792
Sc	15	15	14	14	14
V	152	152	145	148	144
Nb	72	70	75	76	77
Ta	4.14	3.99	4.36	4.37	4.54
Zr	329	317	346	345	357
Hf	6.89	6.66	7.22	7.25	7.51
Th	5.93	5.74	6.49	6.44	6.50
U	1.56	1.62	1.83	1.82	1.82
Y	26	25	26	26	27
La	51	50	55	56	56
Ce	102	101	109	110	111
Pr	12	12	13	13	13

Table 2. Continued.

	TA-2012-39	TA-2012-41	TA-2012-42	TA-2012-43	TA-2012-47
Nd	48	47	50	51	51
Sm	9.00	8.80	9.31	9.34	9.58
Eu	2.84	2.78	2.90	2.94	2.96
Gd	7.43	7.28	7.77	7.71	7.83
Tb	1.00	0.97	1.02	1.03	1.07
Dy	5.54	5.27	5.55	5.49	5.72
Ho	0.94	0.92	0.95	0.95	0.98
Er	2.43	2.34	2.41	2.43	2.51
Tm	0.30	0.29	0.31	0.30	0.32
Yb	1.76	1.69	1.79	1.80	1.83
Lu	0.25	0.23	0.25	0.25	0.25
Cu	51	39	38	38	34
Zn	126	124	129	131	131
Ga	21	21	21	22	22
Pb	3.2	3.1	3.4	3.4	3.5
La/Sm_{cn}	3.67	3.66	3.80	3.85	3.78
La/Yb_{cn}	20.9	21.2	21.9	22.2	21.9
Gd/Yb_{cn}	3.49	3.57	3.58	3.54	3.54
Eu/Eu^*_{cn}	1.06	1.06	1.04	1.06	1.04
Ce/Ce^*_{cn}	1.01	1.01	1.01	1.01	1.00
Al_2O_3/TiO_2	5.5	5.2	5.5	5.4	5.4
K_2O+Na_2O	5.9	5.5	5.9	6.3	6.3
Zr/Y	12.7	12.7	13.3	13.2	13.3
Nb/Y	2.8	2.8	2.9	2.9	2.9
Nb/Ta	17	17	17	17	17
Zr/Hf	48	48	48	48	48
Y/Ho	28	27	27	27	27
Pb/Pb^*_{MORB}	1.0	0.9	1.0	0.9	1.0
Nb/Nb^*_{MORB}	1.08	1.04	1.01	1.02	1.03
Zr/Zr^*_{MORB}	1.44	1.42	1.47	1.46	1.48
Ti/Ti^*_{MORB}	0.86	0.88	0.80	0.82	0.81

Table 2. Continued.

	TA-2012-50	TA-2012-52	TA-2012-53	TA-2012-54	TA-2012-58
SiO_2	45.1	44.8	44.9	44.2	44.6
TiO_2	3.10	3.13	2.51	2.38	2.90
Al_2O_3	14.3	14.8	14.0	13.5	14.6
Fe_2O_3	14.7	14.6	13.9	12.9	14.7
MnO	0.19	0.19	0.19	0.19	0.19
MgO	6.98	6.51	8.82	8.87	7.55
CaO	8.32	8.26	7.59	7.46	8.45
K_2O	2	2.11	1.75	1.48	1.82
Na_2O	4.21	4.51	4.29	3.58	4.2
P_2O_5	0.84	0.93	0.8	0.81	0.79
LOI	0.77	0.61	0.08	2.9	-0.74
Total	100.4	100.4	98.85	98.2	99.09
Mg #	48.5	46.9	55.7	57.7	50.5
Cr	179	161	351	295	181
Co	49	47	48	51	52
Ni	134	108	255	256	129
Rb	47	49	48	51	37
Sr	940	993	884	887	890
Cs	0.61	0.67	0.58	0.66	0.52
Ba	581	636	751	763	721
Sc	14	13	14	15	17
V	187	181	140	105	182
Nb	68	76	72	72	68
Ta	4.11	4.60	4.21	4.18	3.91
Zr	351	383	323	328	311
Hf	7.47	8.02	6.96	6.88	6.78
Th	4.98	5.67	6.21	6.29	5.42
U	1.48	1.78	1.78	1.58	1.54
Y	25	25	25	25	26
La	46	52	52	53	49
Ce	95	107	104	103	98
Pr	12	13	12	12	12

Table 2. Continued.

	TA-2012-50	TA-2012-52	TA-2012-53	TA-2012-54	TA-2012-58
Nd	47	52	49	49	48
Sm	9.48	10.06	9.18	8.93	9.16
Eu	3.04	3.15	2.90	2.79	2.92
Gd	8.02	8.32	7.72	7.30	7.92
Tb	1.05	1.12	1.03	0.99	1.07
Dy	5.59	5.75	5.48	5.38	5.66
Ho	0.92	0.95	0.94	0.93	0.97
Er	2.20	2.23	2.39	2.35	2.44
Tm	0.26	0.27	0.30	0.30	0.30
Yb	1.48	1.49	1.76	1.77	1.77
Lu	0.19	0.19	0.25	0.24	0.25
Cu	49	44	43	30	46
Zn	149	164	124	136	126
Ga	25	25	21	21	23
Pb	3.3	3.5	3.5	2.3	3.2
La/Sm_{cn}	3.15	3.37	3.68	3.80	3.44
La/Yb_{cn}	22.3	25.2	21.3	21.3	19.8
Gd/Yb_{cn}	4.48	4.61	3.63	3.42	3.71
Eu/Eu^*_{cn}	1.07	1.05	1.05	1.06	1.05
Ce/Ce^*_{cn}	1.01	1.00	1.00	0.99	0.99
Al_2O_3/TiO_2	4.6	4.7	5.6	5.7	5.1
K_2O+Na_2O	6.2	6.6	6.0	5.1	6.0
Zr/Y	14.1	15.0	13.0	13.1	12.0
Nb/Y	2.7	3.0	2.9	2.9	2.6
Nb/Ta	17	17	17	17	17
Zr/Hf	47	48	46	48	46
Y/Ho	27	27	26	27	27
Pb/Pb^*_{MORB}	1.0	1.0	1.0	0.7	1.0
Nb/Nb^*_{MORB}	0.99	0.98	1.03	1.18	1.01
Zr/Zr^*_{MORB}	1.45	1.51	1.38	1.45	1.33
Ti/Ti^*_{MORB}	0.96	0.93	0.81	0.81	0.92

Table 2. Continued.

	TA-2012-59	TA-2012-60	TA-2012-61
SiO_2	45.5	45.5	44.3
TiO_2	2.96	2.89	2.81
Al_2O_3	14.7	15.0	13.8
Fe_2O_3	14.9	14.8	14.8
MnO	0.19	0.19	0.19
MgO	7.73	7.52	7.43
CaO	8.59	8.43	8.37
K_2O	1.83	1.93	1.74
Na_2O	4.12	4.28	3.96
P_2O_5	0.76	0.85	0.76
LOI	-0.58	-0.64	1.68
Total	100.7	100.8	99.88
Mg #	50.7	50.1	49.8
Cr	176	175	175
Co	52	50	52
Ni	124	121	125
Rb	36	39	37
Sr	873	923	874
Cs	0.39	0.48	0.56
Ba	700	742	710
Sc	17	16	17
V	183	172	182
Nb	66	70	67
Ta	3.81	4.05	3.87
Zr	302	320	308
Hf	6.51	6.89	6.72
Th	5.33	5.75	5.44
U	1.51	1.59	1.49
Y	26	26	26
La	47	51	48
Ce	96	102	98
Pr	12	13	12

Table 2. Continued.

	TA-2012-59	TA-2012-60	TA-2012-61
Nd	47	50	48
Sm	8.94	9.19	9.14
Eu	2.85	2.97	2.93
Gd	7.77	7.96	7.86
Tb	1.04	1.09	1.04
Dy	5.55	5.64	5.68
Ho	0.95	0.99	0.97
Er	2.38	2.46	2.40
Tm	0.30	0.30	0.30
Yb	1.72	1.81	1.79
Lu	0.24	0.24	0.25
Cu	46	45	46
Zn	125	127	127
Ga	22	23	22
Pb	3.1	3.4	3.2
La/Sm_{cn}	3.41	3.58	3.40
La/Yb_{cn}	19.7	20.3	19.3
Gd/Yb_{cn}	3.74	3.65	3.63
Eu/Eu^*_{cn}	1.05	1.06	1.05
Ce/Ce^*_{cn}	1.00	0.99	1.00
Al_2O_3/TiO_2	5.0	5.2	4.9
K_2O+Na_2O	6.0	6.2	5.7
Zr/Y	11.8	12.5	12.0
Nb/Y	2.6	2.7	2.6
Nb/Ta	17	17	17
Zr/Hf	46	46	46
Y/Ho	27	26	27
Pb/Pb^*_{MORB}	1.0	1.0	1.0
Nb/Nb^*_{MORB}	1.00	1.00	1.05
Zr/Zr^*_{MORB}	1.32	1.36	1.32
Ti/Ti^*_{MORB}	0.96	0.91	0.90

Table 3. Sr isotope data for the alkaline basalts.

	Rb (ppm)	Sr (ppm)	$^{87}Sr/^{86}Sr$	$^{87}Rb/^{86}Sr$
TA 2012-27	38	907	0.703416±11	0.1225
TA 2012-31	36	881	0.703382±12	0.1185
TA 2012-35	37	886	0.703393±11	0.1197
TA 2012-37	40	965	0.703409±09	0.1191
TA 2012-41	38	876	0.703346±12	0.1269
TA 2012-43	42	948	0.703347±11	0.1269
TA 2012-60	39	923	0.703591±11	0.1226

Table 4. Sm-Nd isotope composition of the alkaline basalts.

	Sm (ppm)	Nd (ppm)	$^{147}Sm/^{144}Nd$	$^{143}Nd/^{144}Nd$	T_{DM} (Ma)*	eNd(0)
TA 2012 27	8.752	47.818	0.1108	0.512863±06	426	4.4
TA 2012 31	9.257	50.929	0.1100	0.512902±05	366	5.1
TA 2012 35	9.107	49.335	0.1117	0.512834±09	474	3.8
TA 2012 37	8.770	48.286	0.1099	0.512896±04	374	5.0
TA 2012 41	9.076	49.780	0.1104	0.512922±06	338	5.5
TA 2012 43	8.724	48.296	0.1093	0.512888±04	384	4.9
TA 2012 60	8.251	44.949	0.1111	0.512912±05	355	5.3

*DePaolo (1981)

Table 5. Pb isotopic compositions of the alkaline basalts.

	$^{206}Pb/^{204}Pb$	$\pm 2s^{+}$	$^{207}Pb/^{204}Pb$	$\pm 2s^{+}$	$^{208}Pb/^{204}Pb$	$\pm 2s^{+}$
TA 2012-27	19.575	0.0118	15.586	0.0111	39.088	0.0326
TA 2012-31	19.551	0.0181	15.572	0.0156	39.045	0.0424
TA 2012-35	19.564	0.0258	15.599	0.0216	39.139	0.0574
TA 2012-37	19.557	0.0093	15.578	0.0094	39.064	0.0288
TA 2012-41	19.544	0.0262	15.569	0.0221	39.035	0.0582
TA 2012-43	19.542	0.0135	15.568	0.0123	39.032	0.0354
TA 2012-60	19.404	0.0144	15.581	0.0134	38.994	0.0375

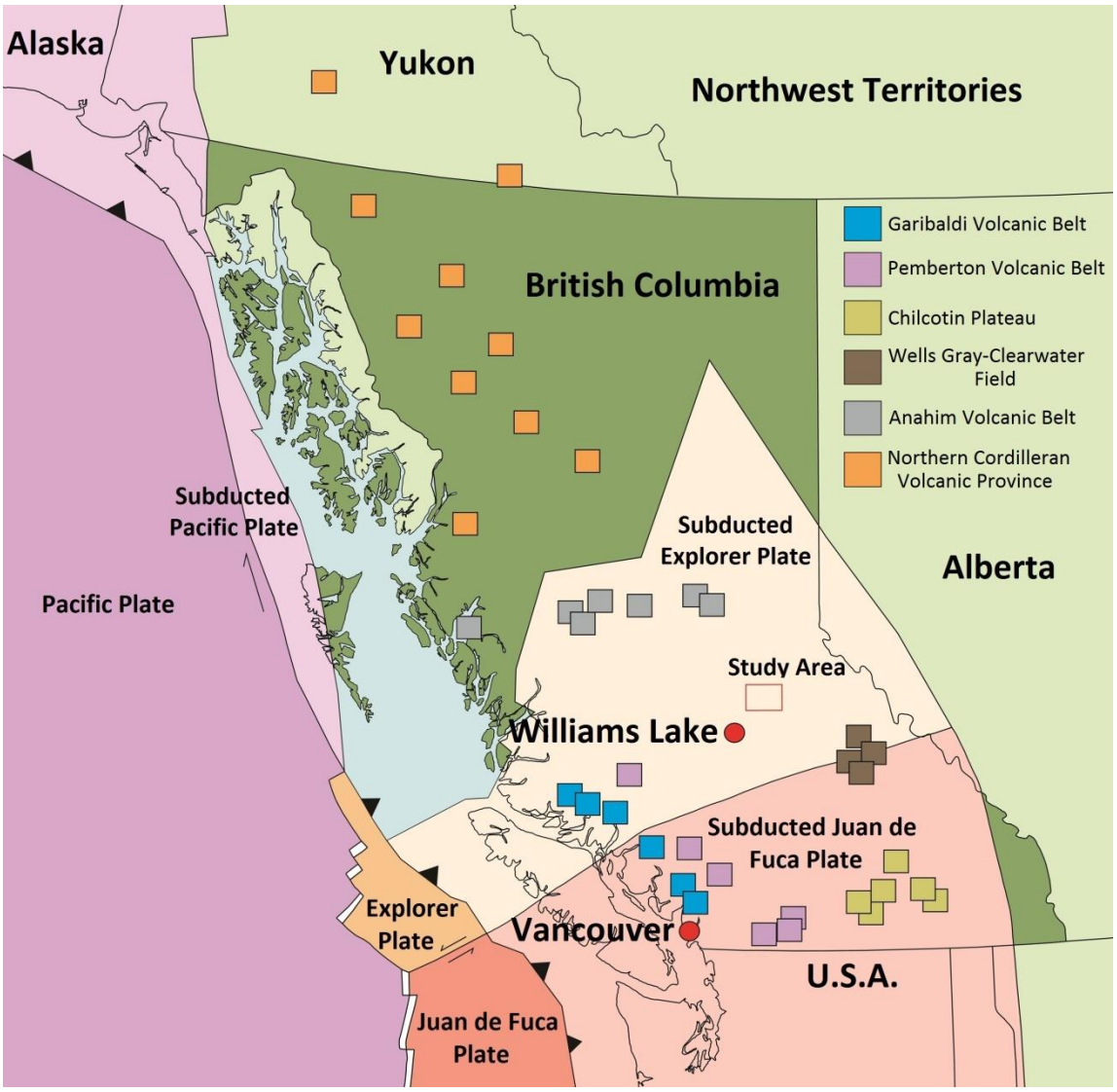

Figure 1. Location of the Tasse alkaline basalts (study area), current tectonic features, and Late Cenozoic volcanic belts (shown schematically) of the Canadian Cordillera (modified from Madsen et al., 2006).

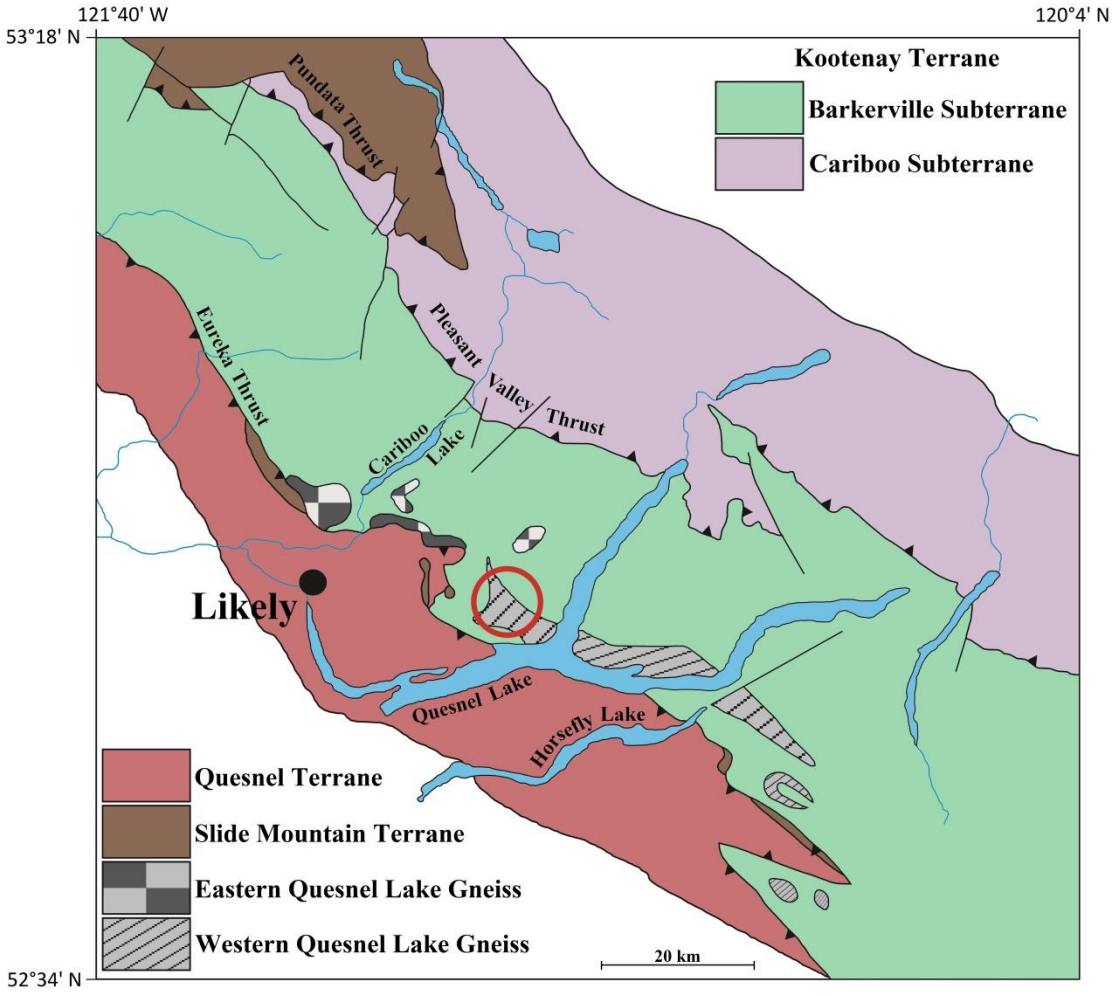

Figure 2. Geological map of associated terranes (Slide Mountain, Quesnel and Kootenay) of the Tasse sampling areas within Southeastern British Columbia. Sampling region is denoted by the red circle (modified from Ferri and Schiarizza, 2006).

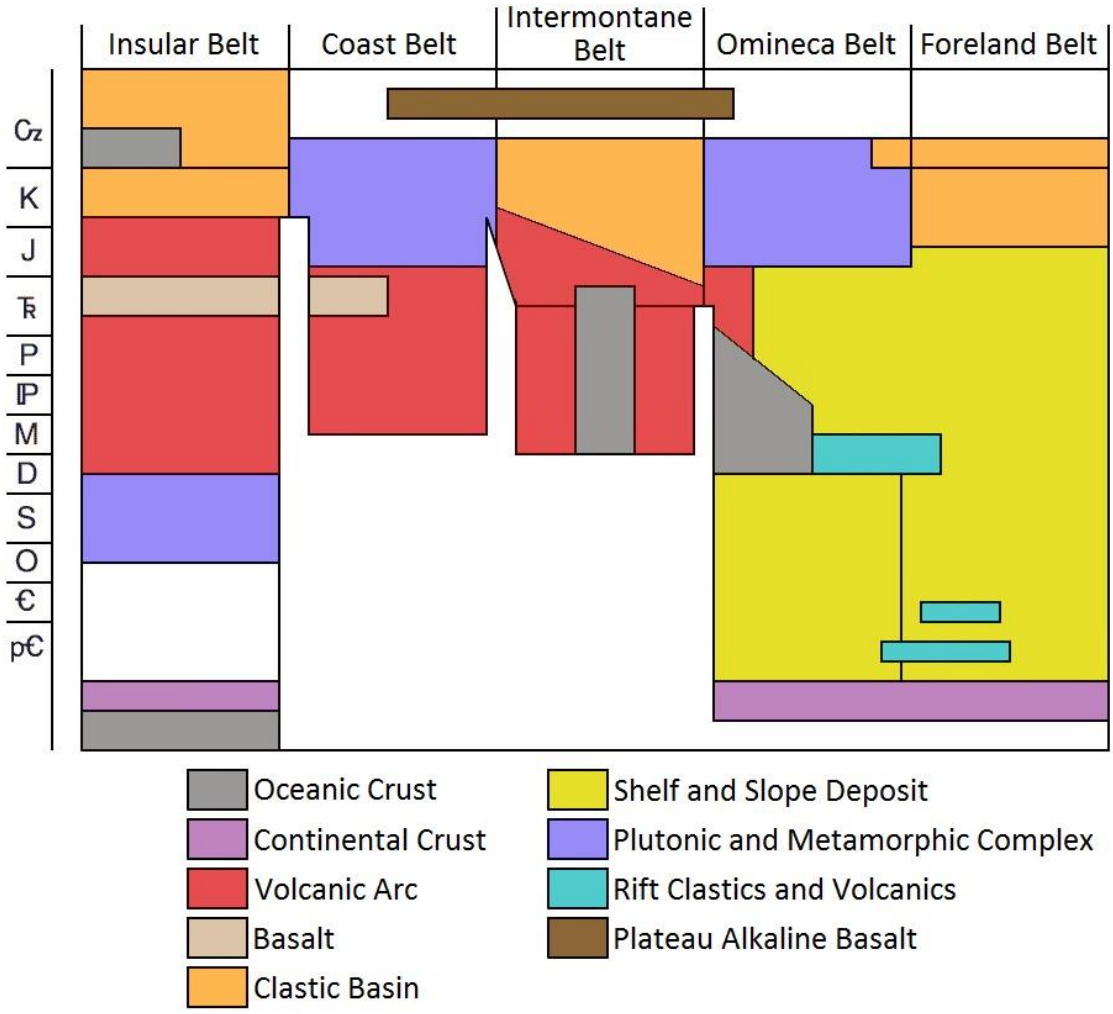

Figure 3. Distribution of lithologies in the five morphogeological belts of British Columbia. Distribution is shown spatially and temporally (modified from Gabrielse et al., 1992).

Figure 4. A map of British Columbia showing the distribution of the five morphogeological belts of the Canadian Cordillera (modified from Gabrielse et al., 1992 and Monger and Price, 2002).

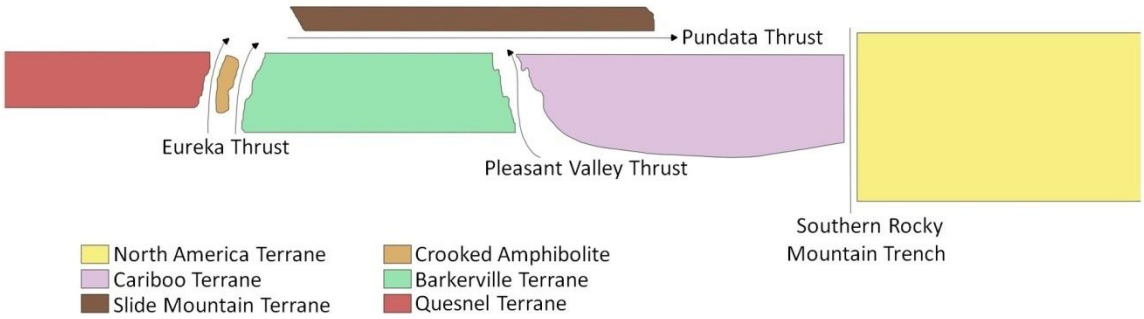

Figure 5. A rough structural schematic showing the relationship amongst the terranes and thrusts (faults) of the Tasse region. The arrows indicate thrust direction (modified from Struik, 1986).

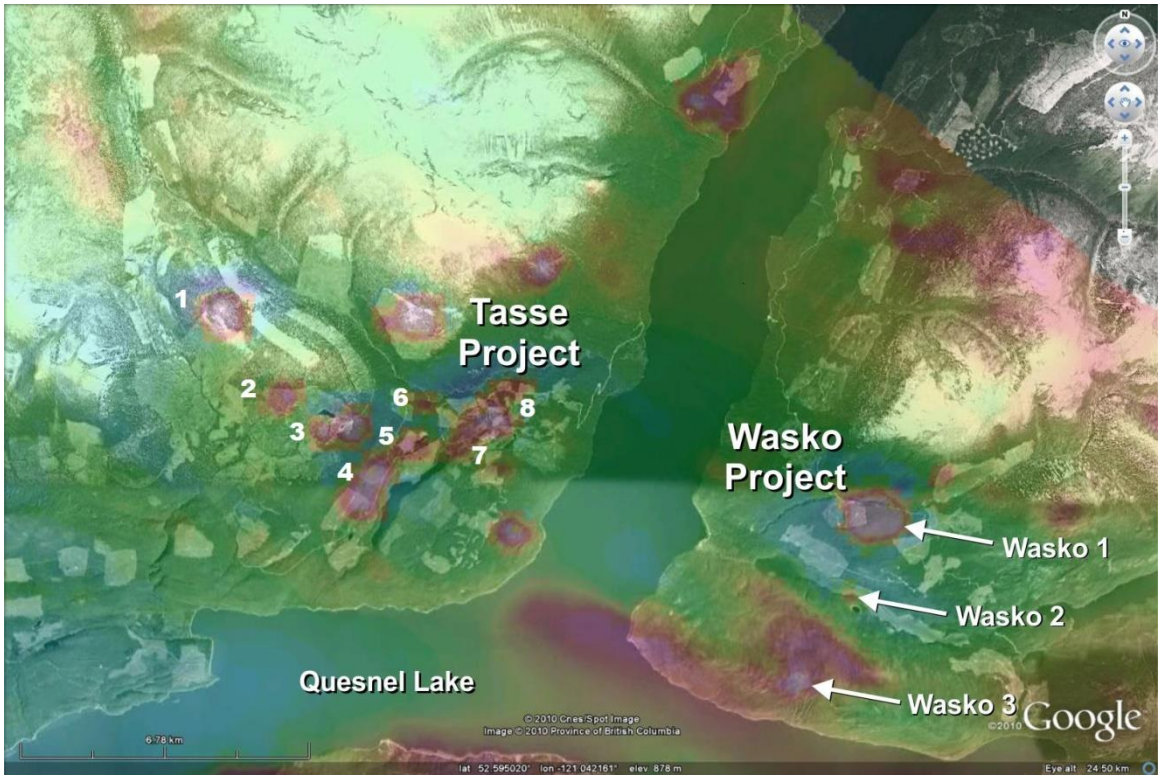

Figure 6. Google Earth overlay of magnetic anomalies for the Tasse and Wasko properties of Barker Minerals Ltd. Numbers associated with the Tasse magnetic anomalies are assigned to sampling locations. Magnetic highs are seen as purple and red (modified from Barker Minerals Ltd.).

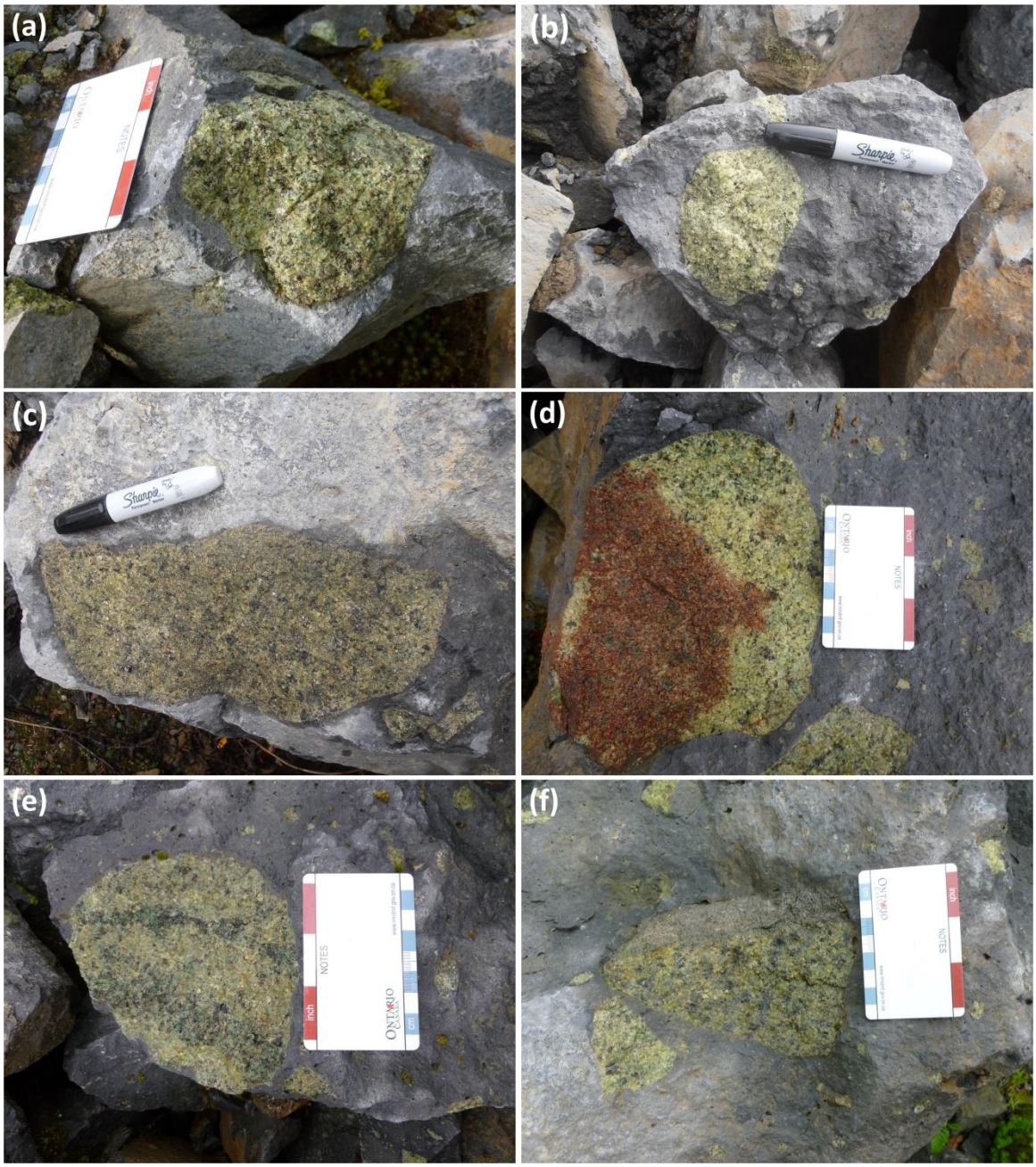

Figure 7. Representative samples of spinel lherzolites found in the Tasse region of British Columbia. (a-c) Spinel lherzolite xenoliths set in host alkaline basalts. (d) Oxidized spinel lherzolite sample. (e-f) Spinel lherzolite samples displaying pyroxene-spinel rich bands and lherzolite-pyroxenite layers, respectively.

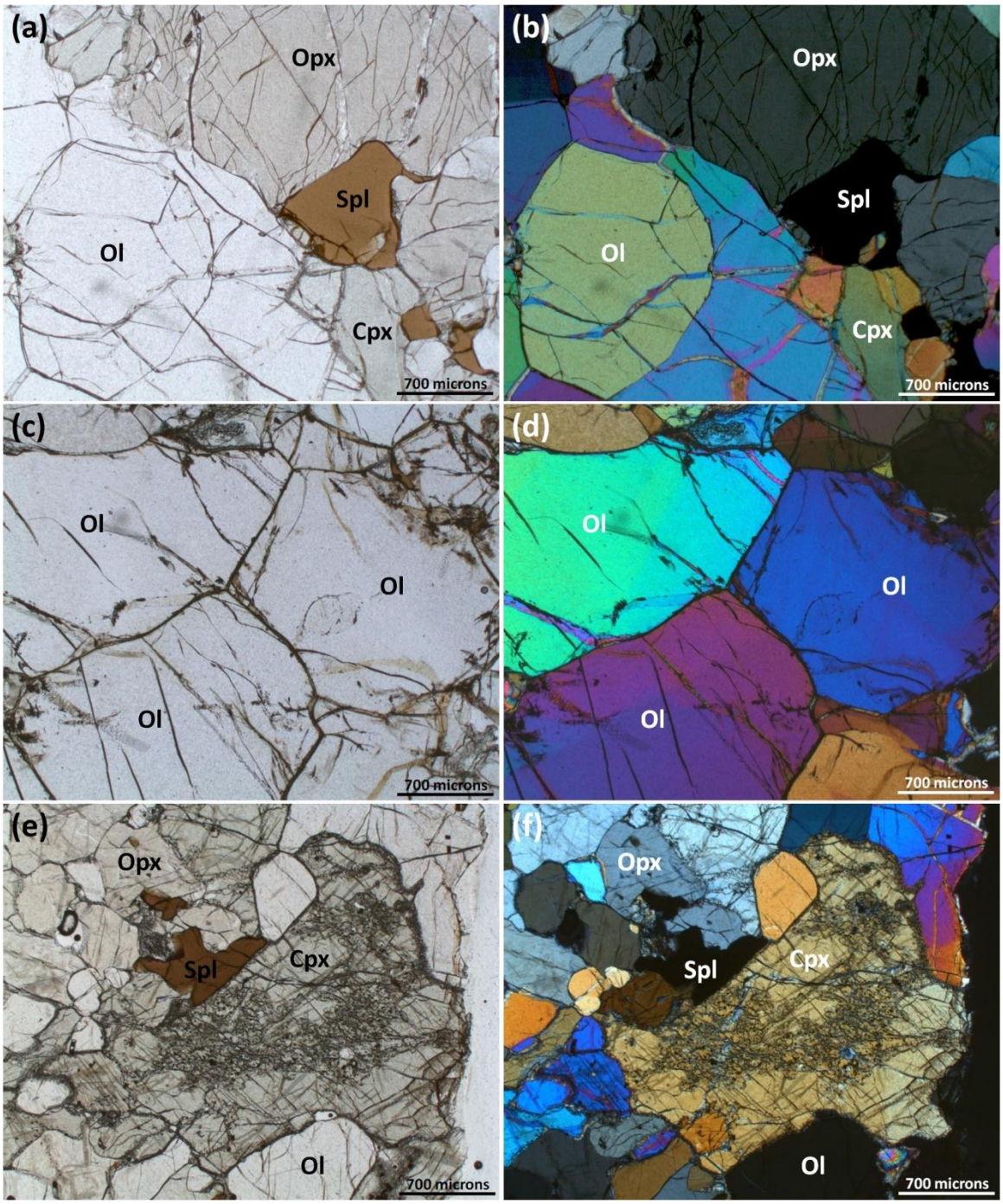

Figure 8. Plane (a, c, e) and cross-polarized (b, d, f) photomicrographs of spinel lherzolites. (a-d) Representative igneous textures and mineral associations. (e-f) Resorption texture of clinopyroxene and associated spinel (Ol: olivine; Opx: orthopyroxene; Cpx: clinopyroxene; Spl: spinel).

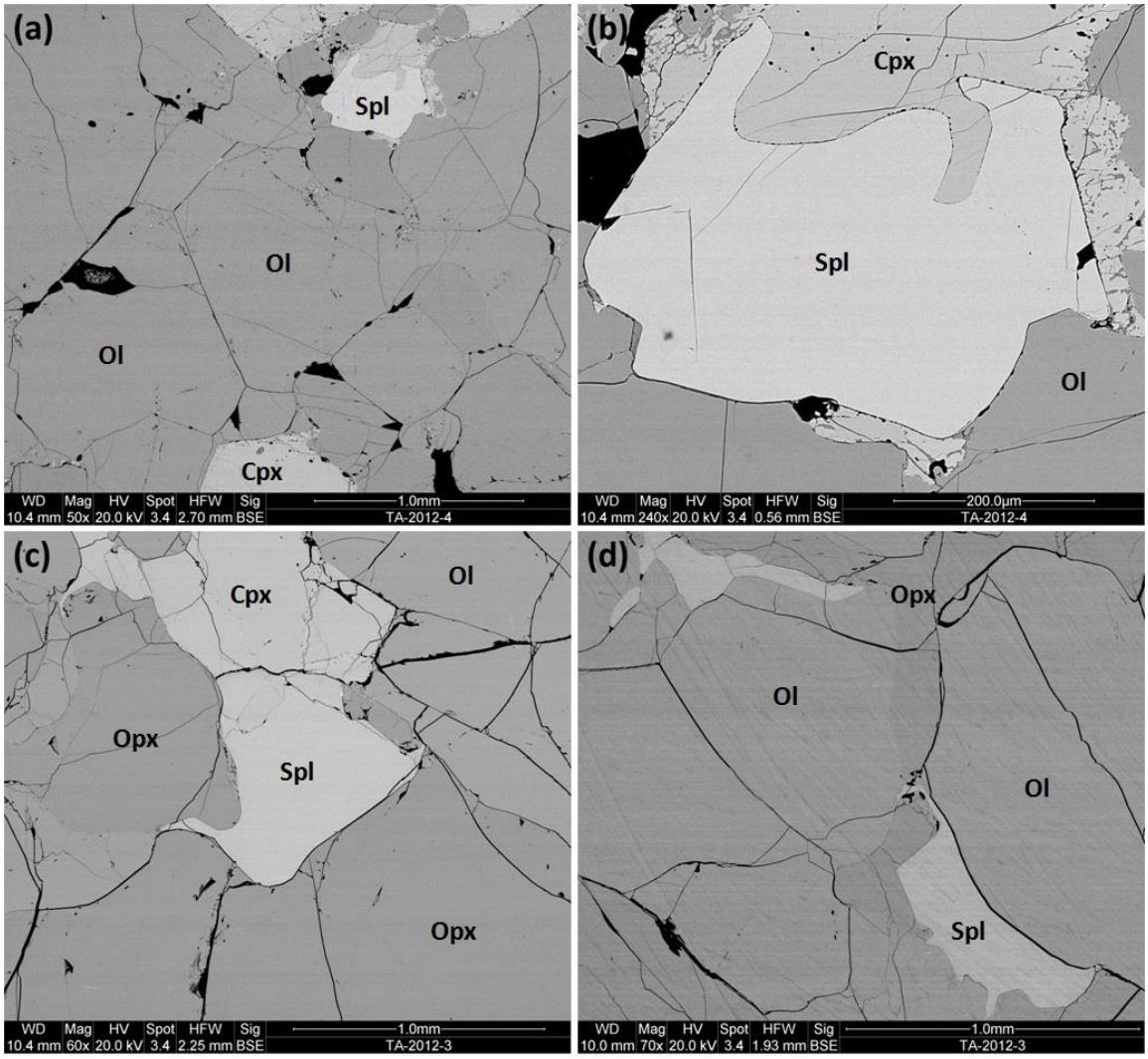

Figure 9. SEM back-scattered electron (BSE) images of spinel lherzolites. (a-b) Spinel (white) associated with resorbed clinopyroxene (light grey) and olivine (dark grey). (c-d) Common textural features of pyroxenes and olivine (light grey and dark grey) with associated spinel (Ol: olivine; Opx: orthopyroxene; Cpx: clinopyroxene; Spl: spinel).

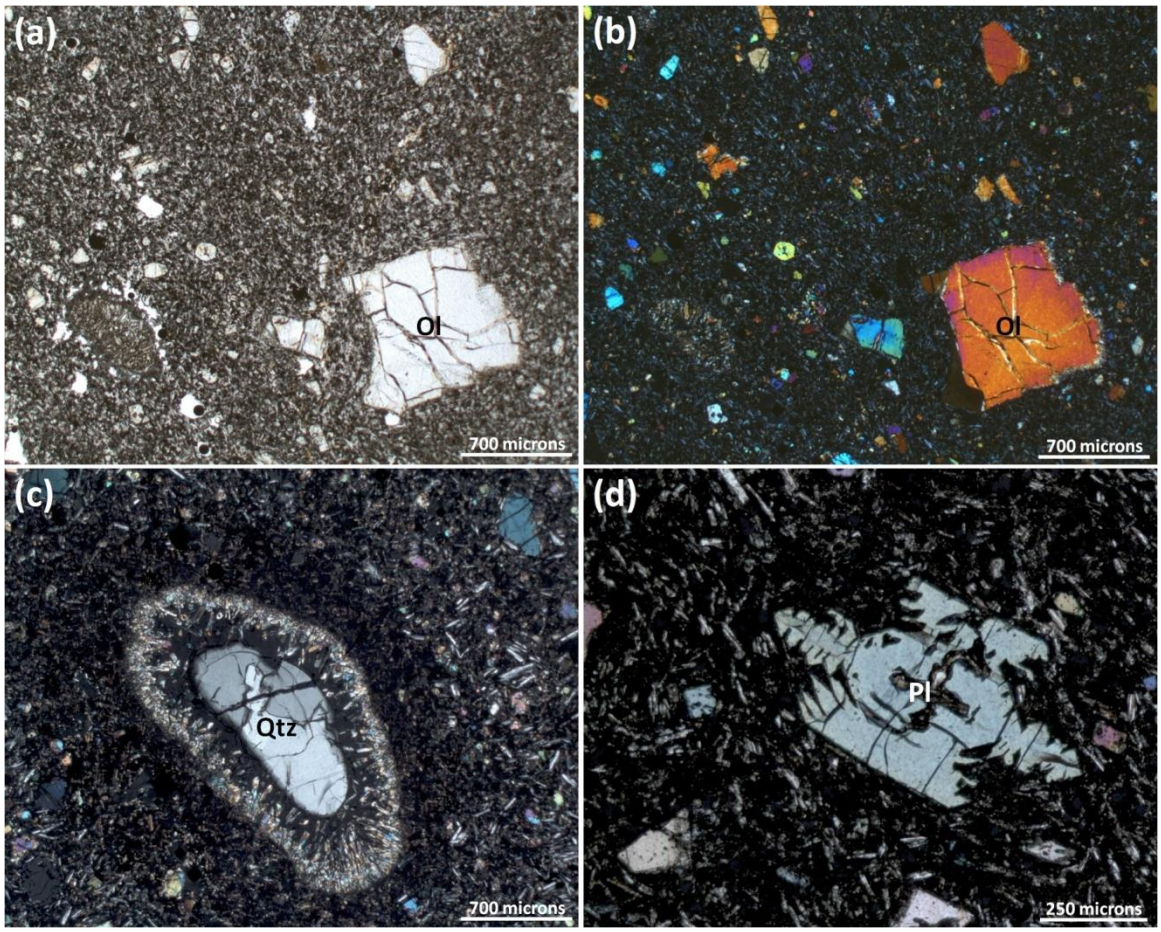

Figure 10. Plane and cross polarized photomicrographs of alkaline basalts (a-b) Representative fine-grained textures and mantle xenocrysts. (c-d) Quartz xenocryst with reaction rim of unknown fine-grained minerals and skeletal textures, respectively. (Mineral abbreviations: Ol - olivine; Qtz - quartz)

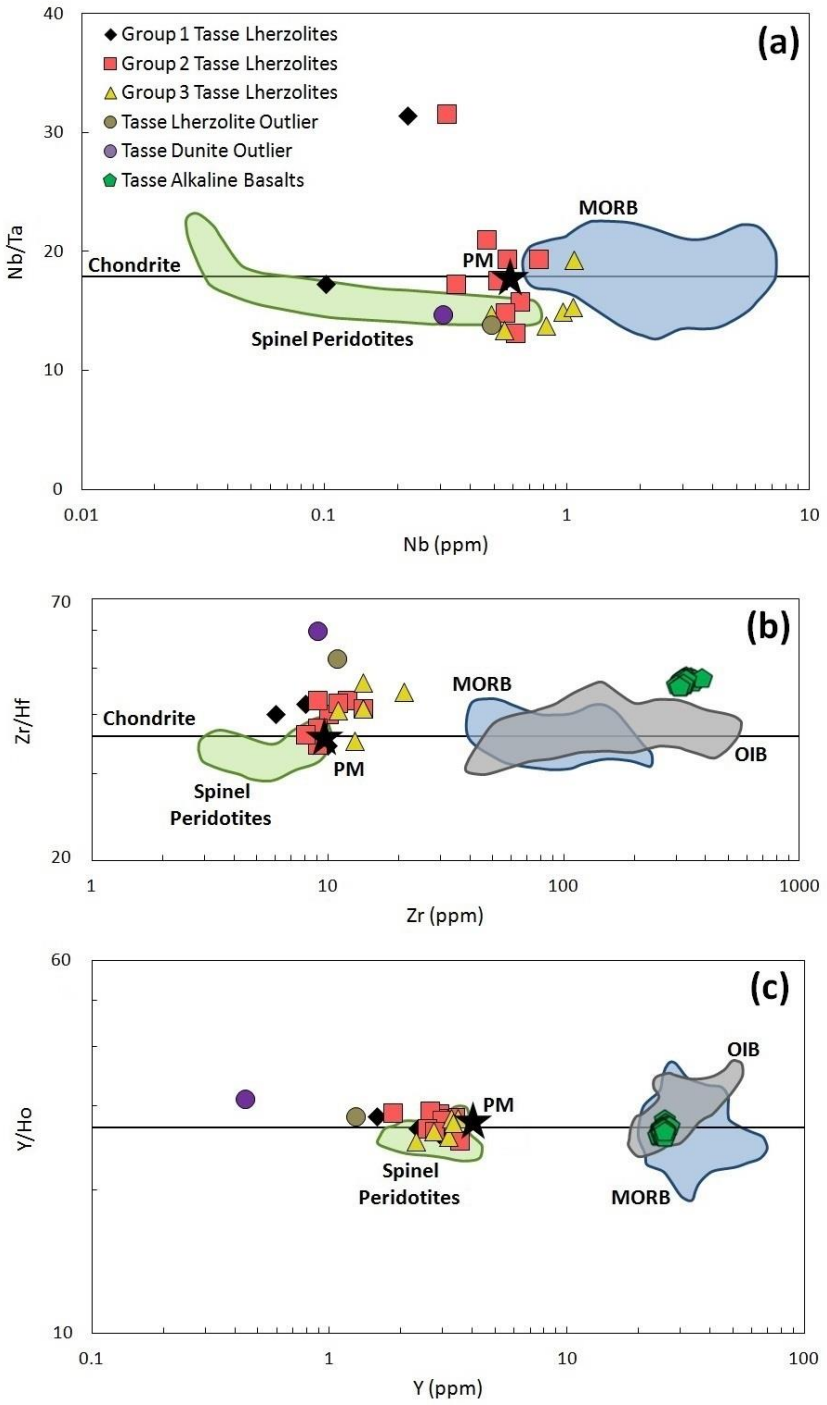

Figure 11. Ratios (a) Nb/Ta, (b) Zr/Hf and (c) Y/Ho of Tasse mantle xenoliths and alkaline basalts. Shaded regions represent spinel peridotites, MORB, OIB and PM are from Jochum et al. (1989). Chondritic values are represented as the black line crossing primitive mantle (PM) shown as a black star.

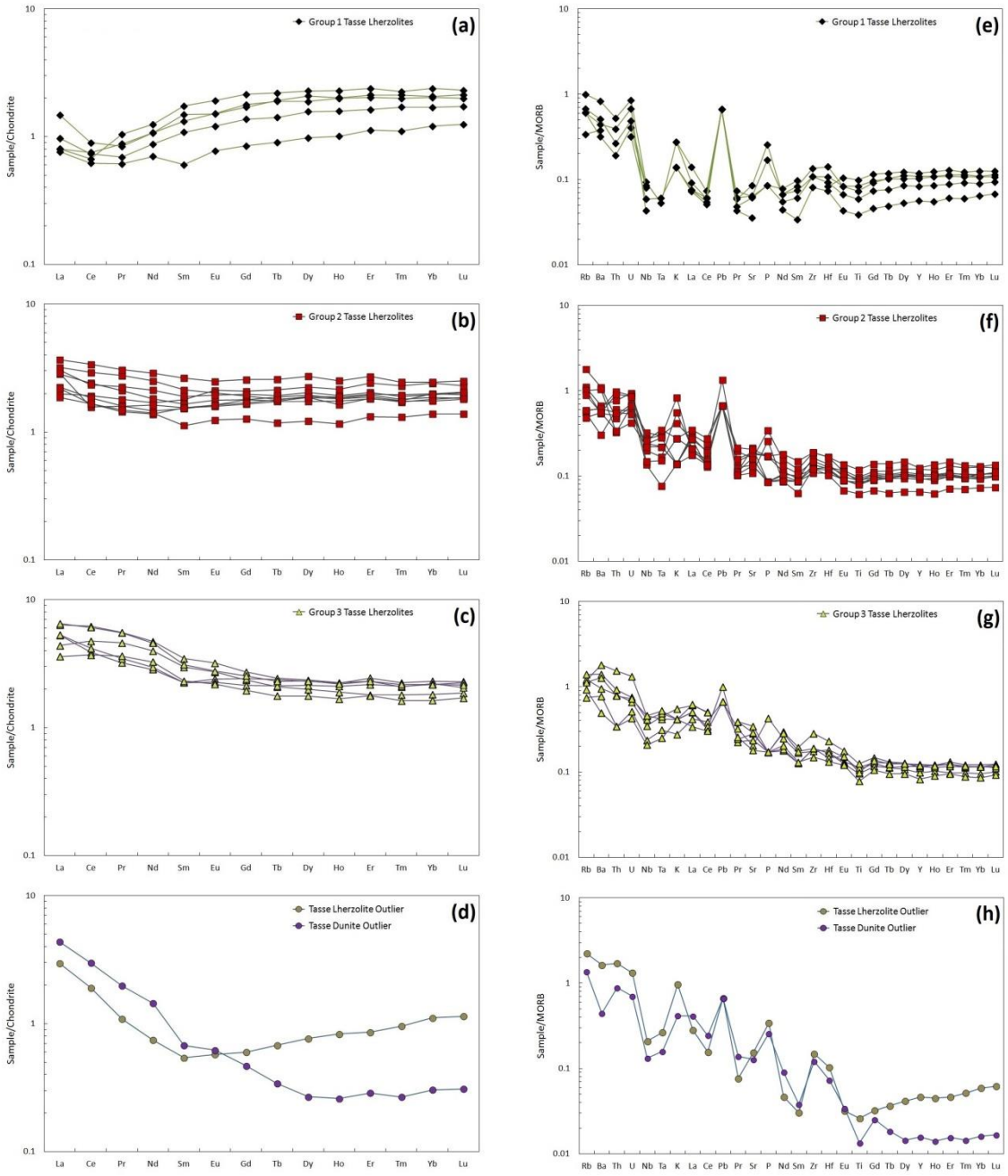

Figure 12. Chondrite- (a-d) and N-MORB- (e-h) normalized patterns for (a and e) Group 1 lherzolites, (b and f) Group 2 lherzolites, (c and g) Group 3 lherzolites and (d and h) Outlier xenolith samples. Chondrite and N-MORB normalization values are McDonough and Sun (1995) and Sun and McDonough (1989), respectively.

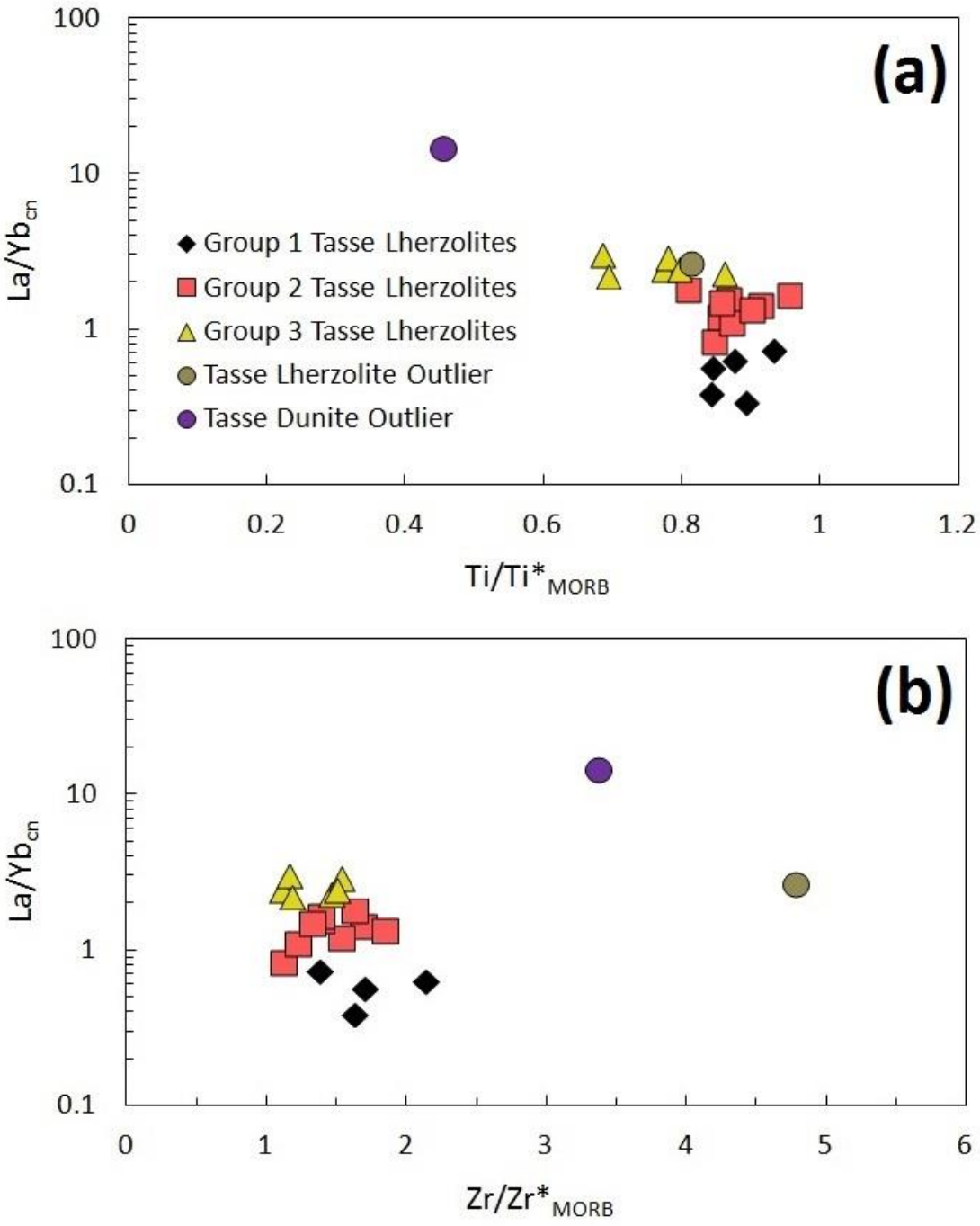

Figure 13. La/Yb_{cn} vs. (a) Ti/Ti^*_{MORB} and (b) Zr/Zr^*_{MORB} plots. Chondrite and N-MORB normalization values are McDonough and Sun (1995) and Sun and McDonough (1989), respectively.

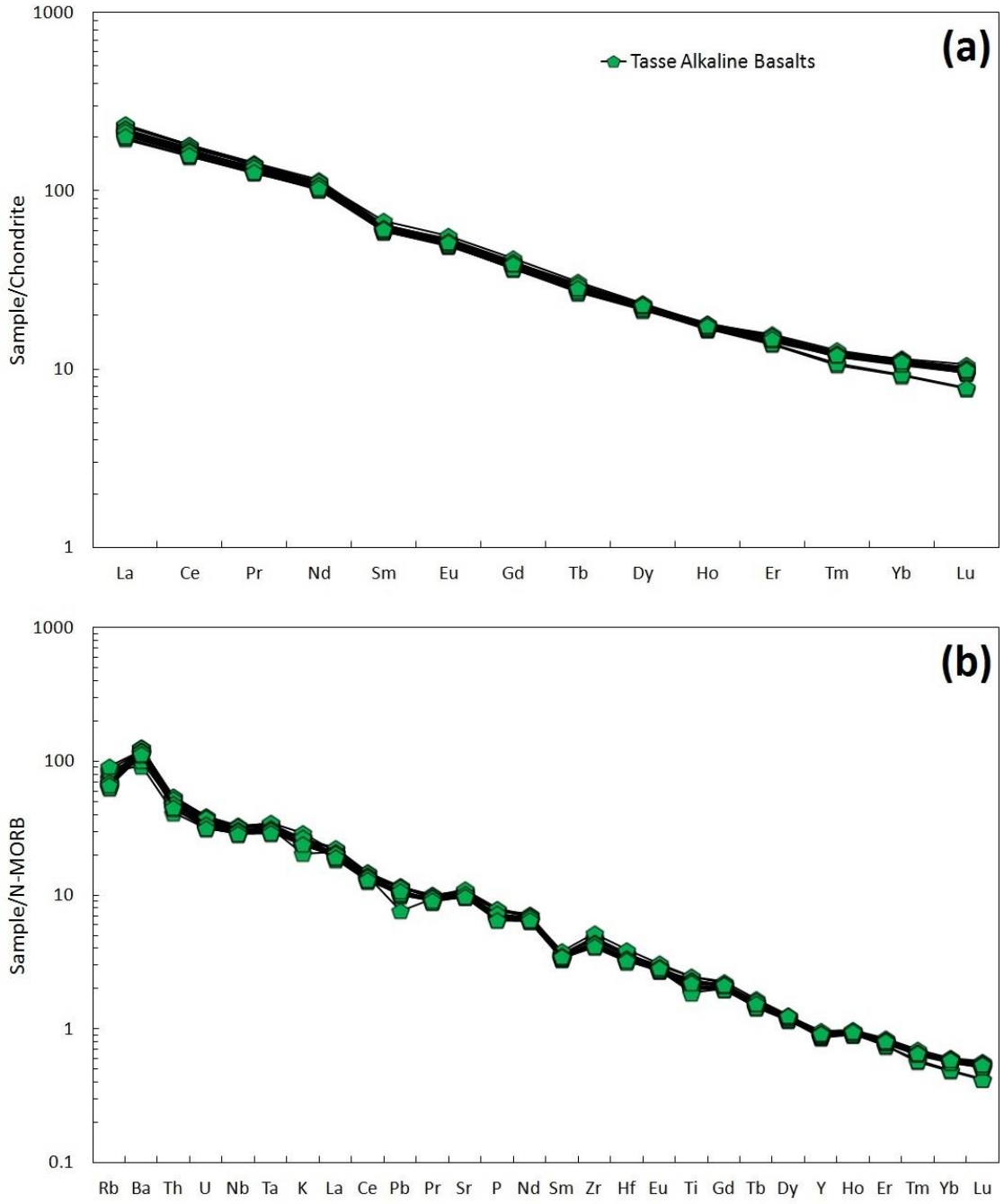

Figure 14. (a) Chondrite-normalized patterns and (b) N-MORB-normalized patterns of the Tasse alkaline basalts. Chondrite and N-MORB normalization values are McDonough and Sun (1995) and Sun and McDonough (1989), respectively.

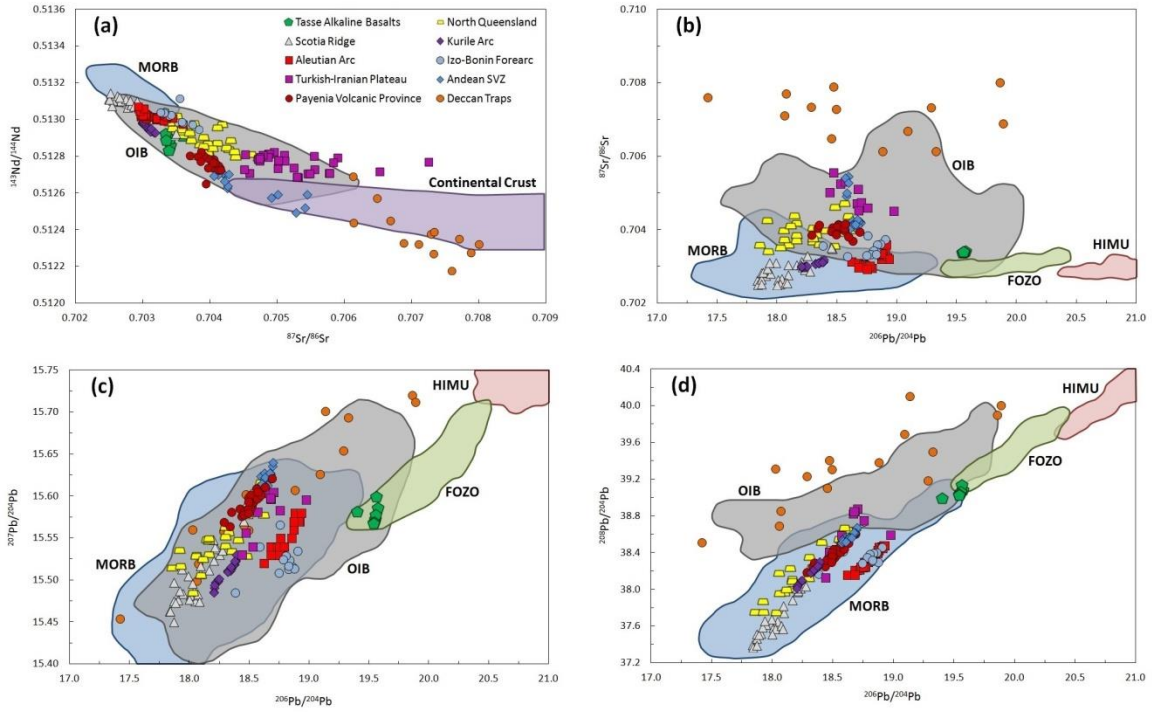

Figure 15. Sr−Nd−Pb isotopic plots of the Tasse alkaline basalts and volcanic rocks from a range of locations and tectonic settings. The shaded regions indicate isotopic source characteristics of mid-ocean ridge basalts (MORB), ocean island basalts (OIB), focal zone (FOZO), high-μ (HIMU) and continental crust from Stracke et al. (2005). Data was collected from Fretzdorff et al., 2002 (Scotia Ridge); Holm et al., 2014 (Andean Southern Volcanic Zone); Kheirkhah et al., 2015 (Turkish–Iranian Plateau); Kuritani et al., 2008 (Kurile Arc); Pearce et al., 1992 (Izo-Bonin Forearc); Peng et al., 2014 (Deccan Trap); Singer et al., 2007 (Aleutian Arc); Søager et al., 2015 (Payenia Volcanic Province); Zhang et al., 2001 (North Queensland). Outlier samples were removed from the shaded regions and Deccan Traps.

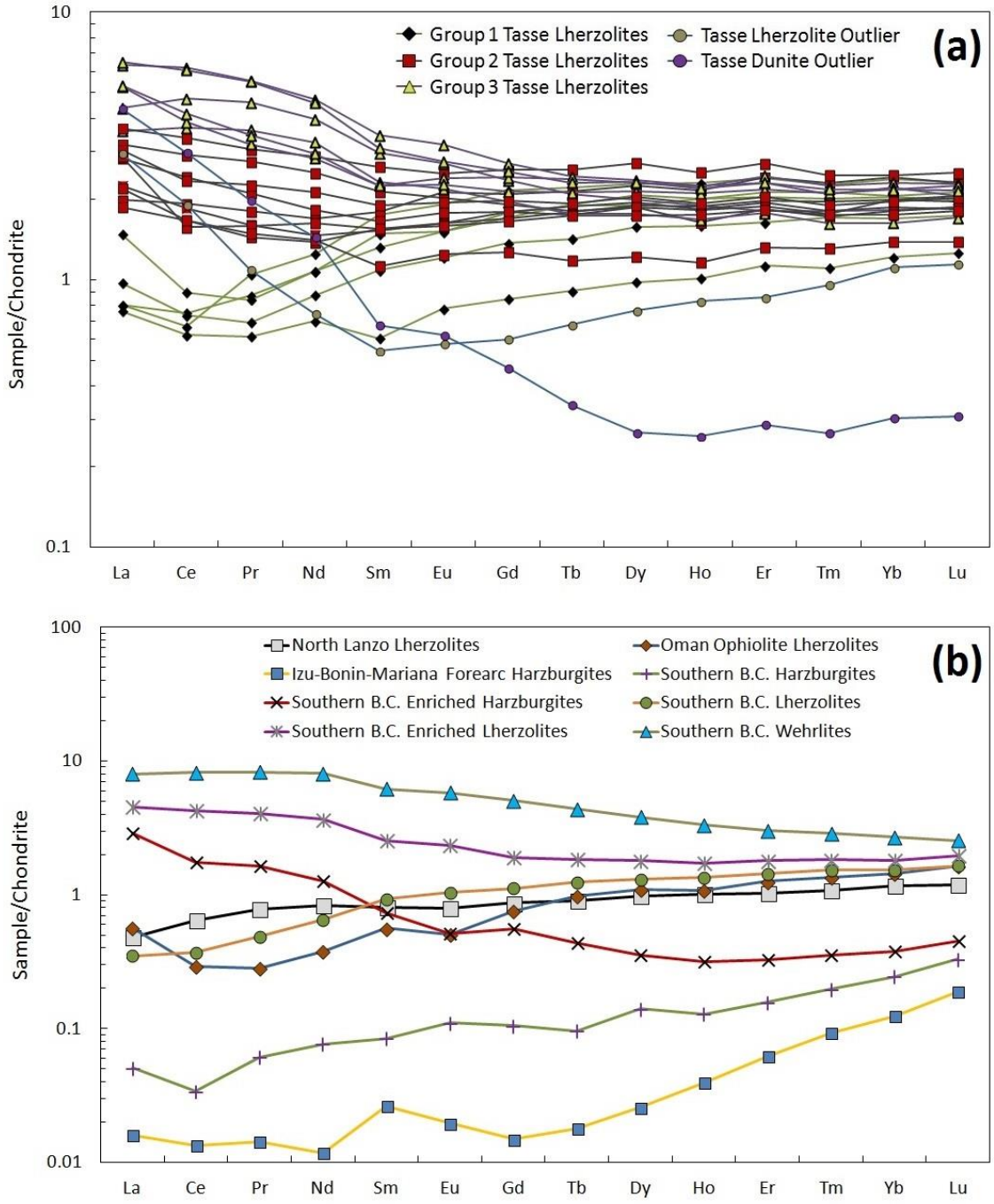

Figure 16. Chondrite-normalized comparison plots of the (a) Tasse xenolith groups and (b) Izu-Bonin-Mariana forearc harzburgites, Central Oman ophiolite lherzolites, North Lanzo lherzolites and xenoliths from other localities in British Columbia. Forearc data from Parkinson and Pearce (1998). Ophiolite lherzolite data from Khedr et al. (2014). North Lanzo data from Guarnieri et al. (2012). Southern British Columbia data from Peslier et al. (2002). Values are normalized to McDonough and Sun, 1995.

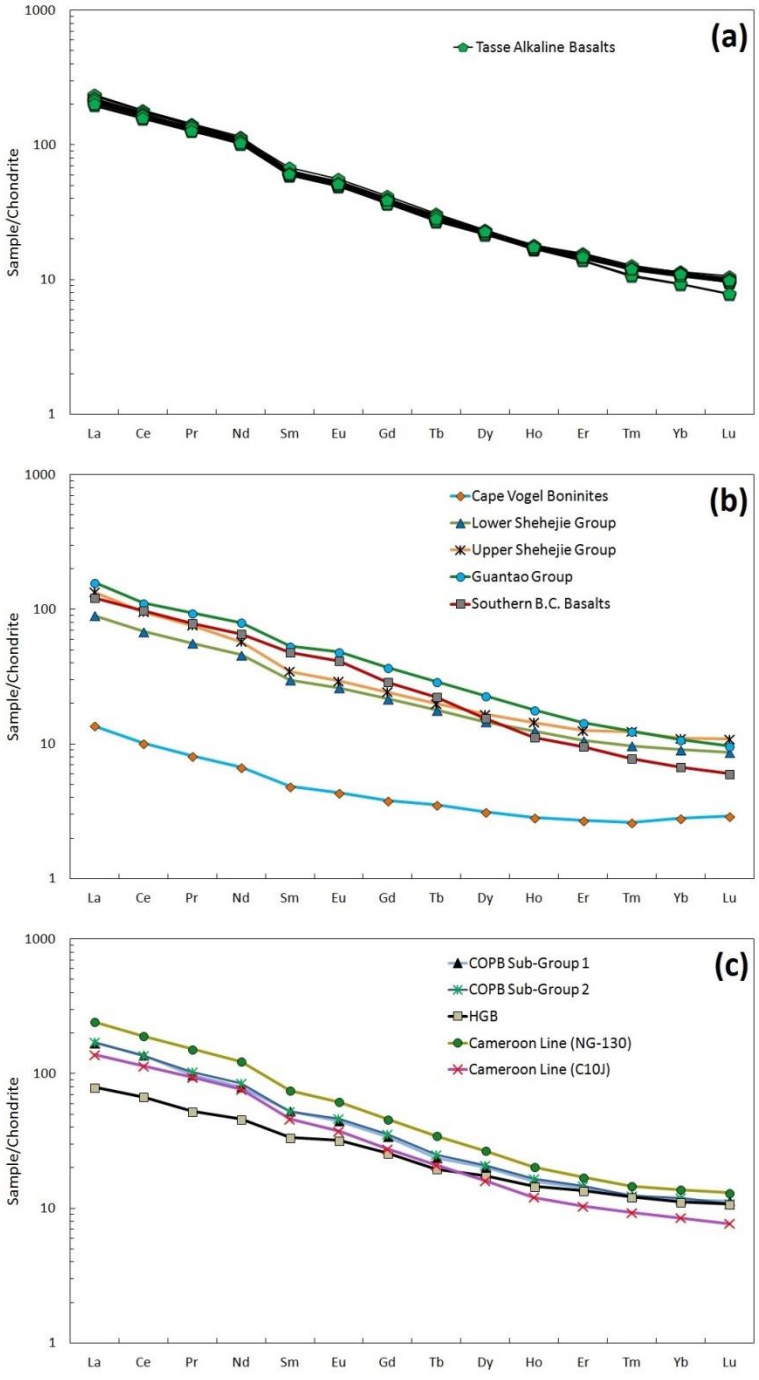

Figure 17. Chondrite-normalized comparison plots of (a) Tasse basalts (b) Cape Vogel boninites, Bohai Basin basalts (LSG, USG, GG) and Southern British Columbia basalts (c) COPB, HGB and Cameroon Line basalts. Boninite data from König et al. (2010). Bohai Basin basalt data Li et al. (2014). Southern British Columbia data from Sluggett (2008). COPB and HGB data from Polat et al. (1997). Cameroon Line data from Nkouandou & Temdjim (2011). Values are normalized to McDonough and Sun, 1995.

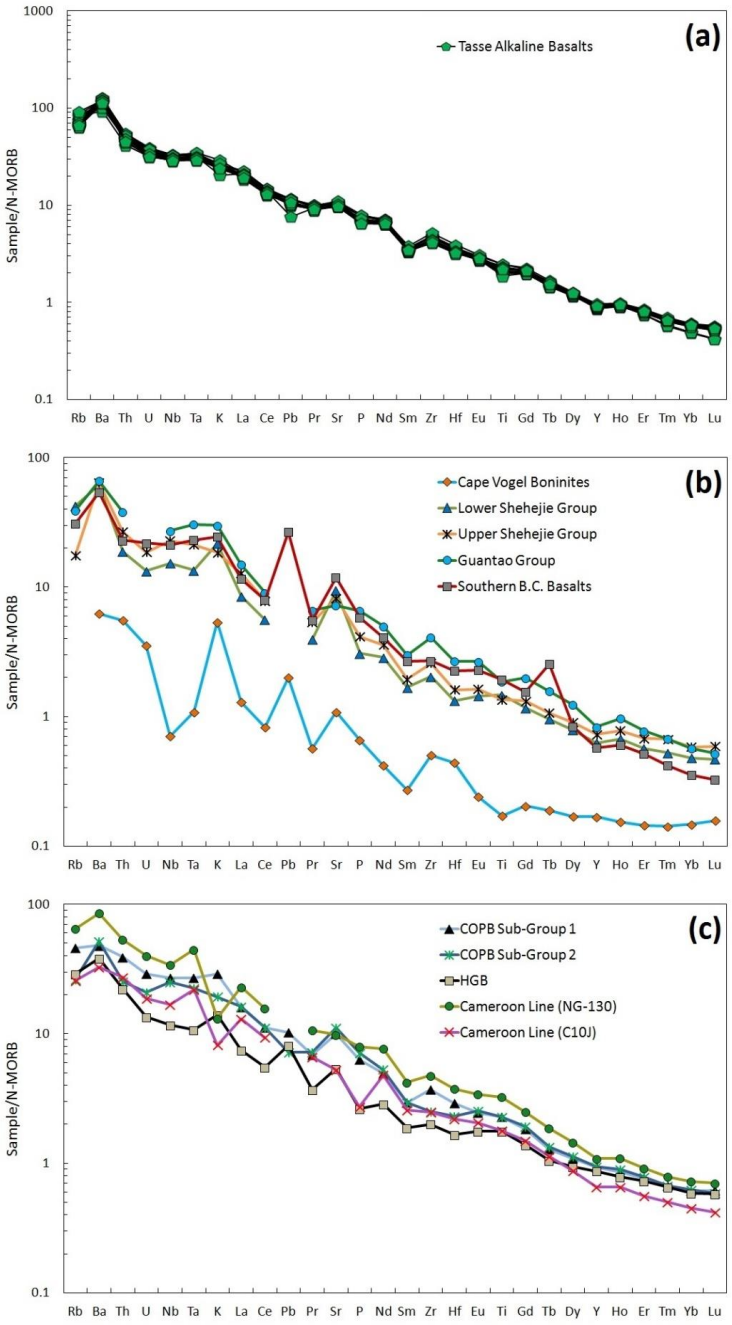

Figure 18. N-MORB-normalized comparison plots of (a) Tasse basalts (b) Cape Vogel boninites, Bohai Basin basalts (LSG, USG, GG) and Southern British Columbia basalts (c) COPB, HGB and Cameroon Line basalts. Boninite data from König et al. (2010). Bohai Basin basalt data Li et al. (2014). Southern British Columbia data from Sluggett (2008). COPB and HGB data from Polat et al. (1997). Cameroon Line data from Nkouandou & Temdjim (2011). Values are normalized to Sun and McDonough and Sun, 1989.

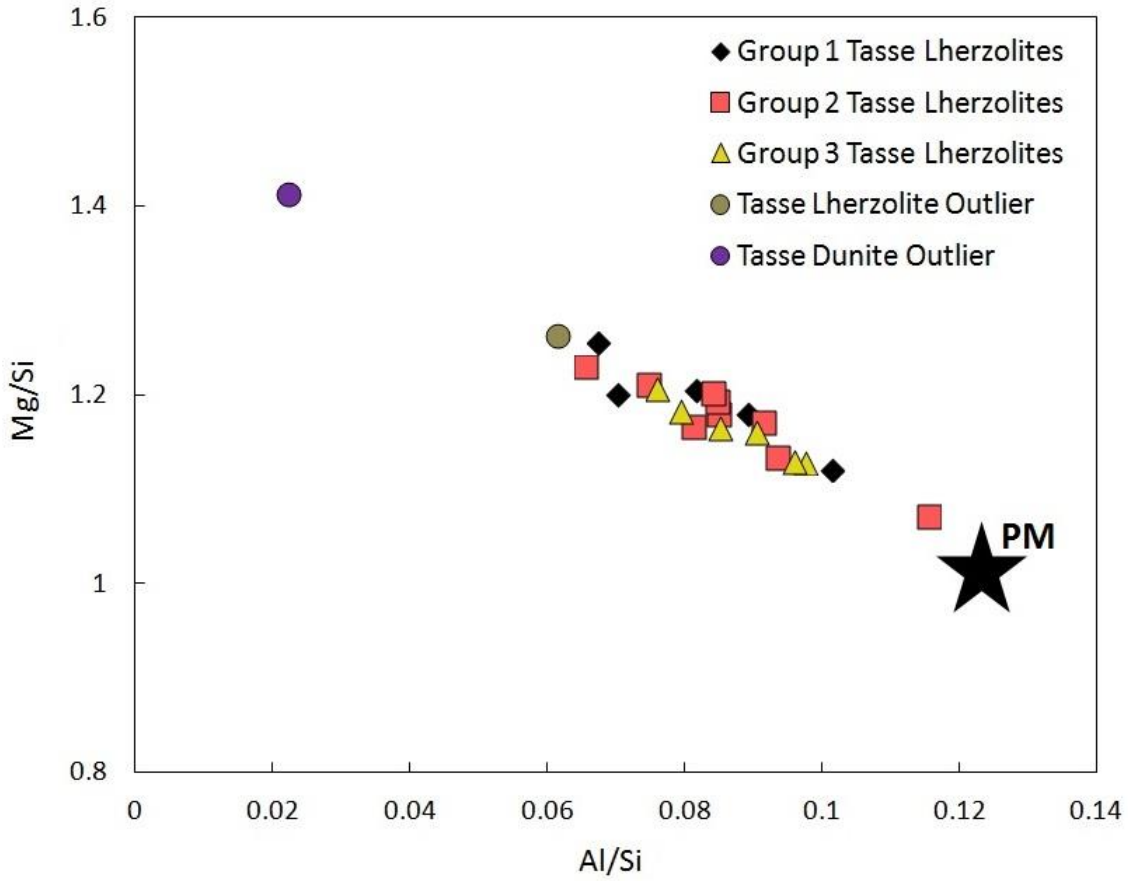

Figure 19. Primitive mantle evolution plot (Mg/Si vs. Al/Si). Linear relationship indicates that the mantle xenoliths originated from a primitive upper mantle source (PM). Major element oxide weight percent values are converted to ppm (modified from Canil and Lee, 2009).

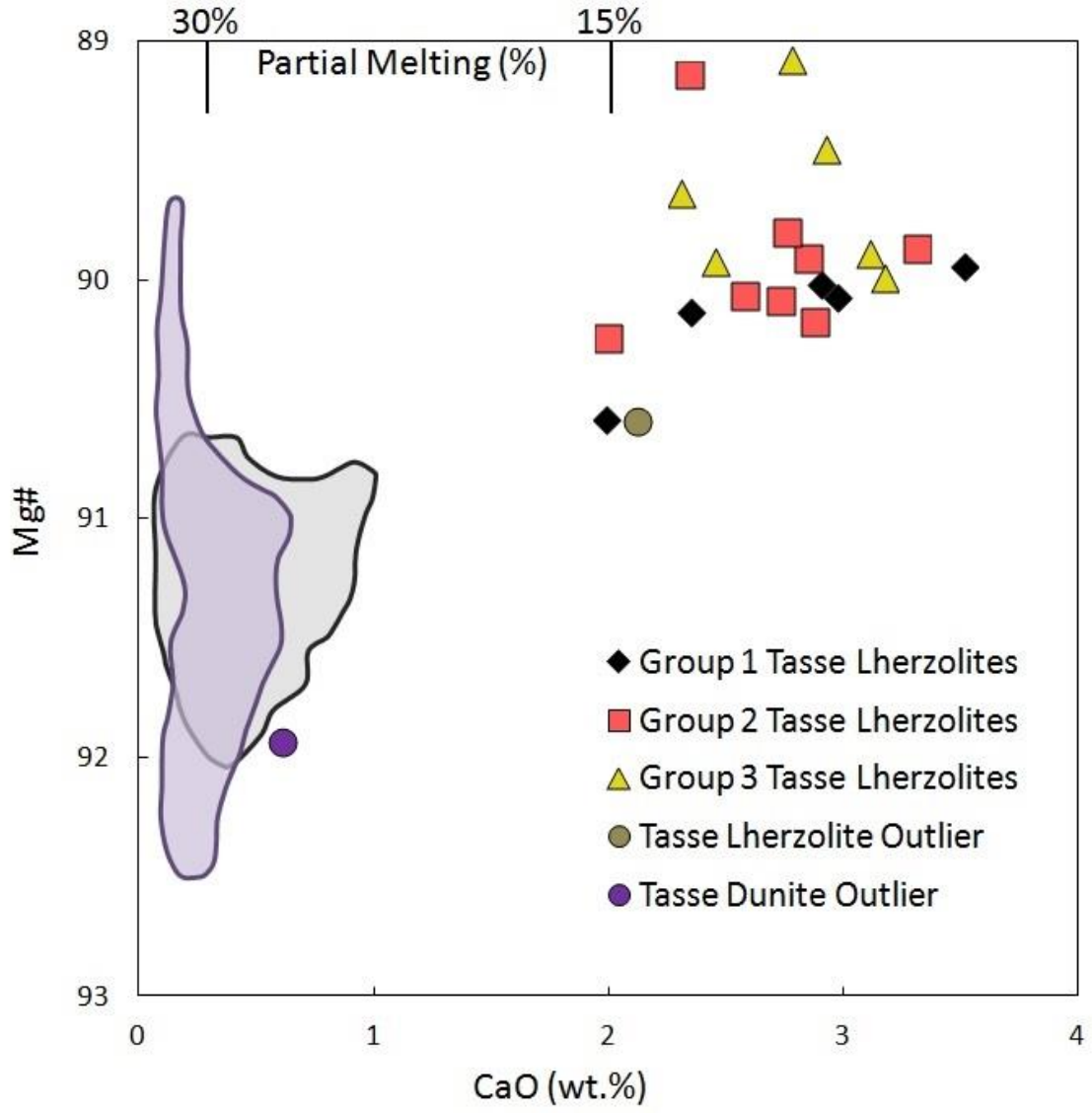

Figure 20. Partial melting diagram utilizing Mg# vs. CaO (wt.%). Vertical lines at the top indicate the percent of partial melting from a primitive source. The grey shaded region represents Torishima and Conical Seamount harzburgite data. The purple shaded region represents Torishima and Conical Seamount dunite data. Data for the shaded regions were taken from Ishii et al. (1992).

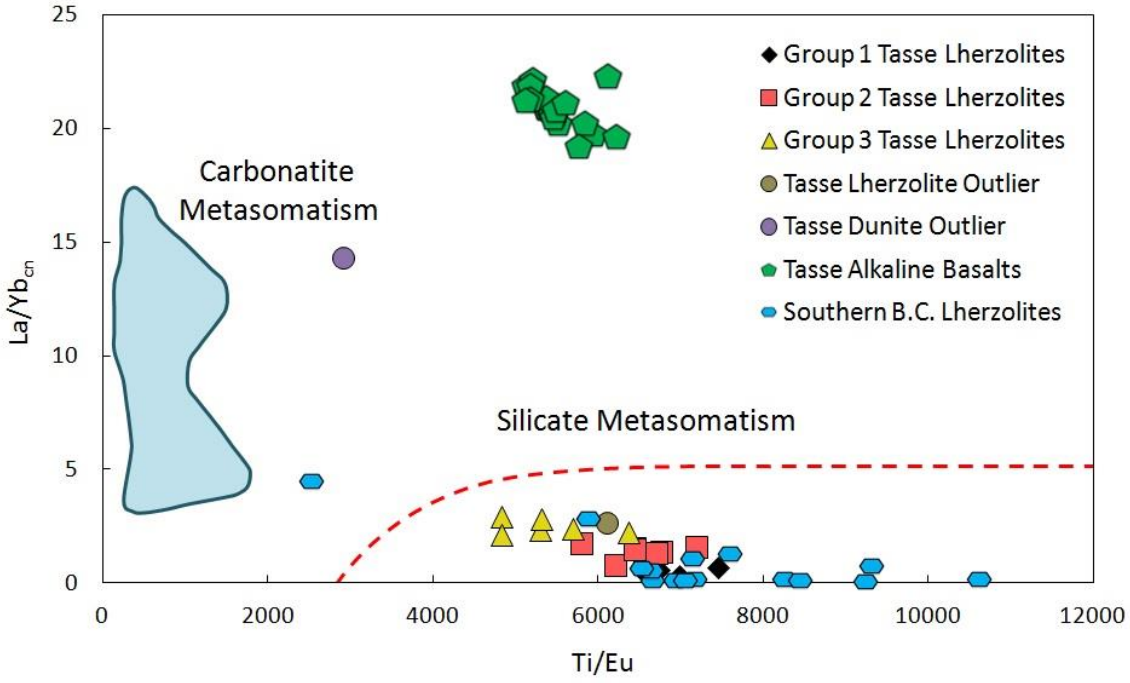

Figure 21. Metasomatism discrimination plot between silicate and carbonatite melt metasomatism. The shaded region indicates Grand Comore xenoliths (from Coltorti et al., 1999) which have undergone carbonatite melt metasomatism. The dashed red line denotes the field dominated by silicate metasomatism. British Columbia lherzolite data was collected from Peslier et al. (2002).

Appendix A. Field description and GPS coordinates of the mantle xenoliths

Sample #	Rock Type	Eastings	Northings	Property #
TA-2012-01	Olivine-Pyroxene-Spinel Peridotite Xenolith	628821	5827460	5
TA-2012-02	Olivine-Pyroxene-Spinel Peridotite Xenolith	628823	5827469	5
TA-2012-03	Olivine-Pyroxene-Spinel Peridotite Xenolith	628828	5827458	5
TA-2012-04	Olivine-Pyroxene-Spinel Peridotite Xenolith	628812	5827480	5
TA-2012-05	Olivine-Pyroxene-Spinel Peridotite Xenolith	628819	5827457	5
TA-2012-06	Olivine-Pyroxene-Spinel Peridotite Xenolith	628822	5827463	5
TA-2012-07	Olivine-Pyroxene-Spinel Peridotite Xenolith	628813	5827460	5
TA-2012-08	Spinel-bearing Dunite Xenolith	628819	5827447	5
TA-2012-09	Spinel-bearing Dunite Xenolith	628820	5827447	5
TA-2012-10	Pyroxene-bearing Dunite Xenolith	628820	5827447	5
TA-2012-11	Olivine-Pyroxene-Spinel Peridotite Xenolith	628820	5827447	5
TA-2012-13	Olivine-Pyroxene-Spinel Peridotite Xenolith	628833	5827461	5
TA-2012-14	Olivine-Pyroxene-Spinel Peridotite Xenolith	628818	5827443	5
TA-2012-15	Olivine-Pyroxene-Spinel Peridotite Xenolith	628790	5827432	5
TA-2012-16	Olivine-Pyroxene-Spinel Peridotite Xenolith	628795	5827444	5
TA-2012-17	Olivine-Pyroxene-Spinel Peridotite Xenolith	628791	5827449	5
TA-2012-18	Pyroxene- & Spinel-bearing Dunite Xenolith	628791	5827449	5
TA-2012-19	Olivine-Pyroxene-Spinel Peridotite Xenolith	628787	5827443	5
TA-2012-20	Olivine-Pyroxene-Spinel Peridotite Xenolith	628787	5827443	5
TA-2012-21	Olivine-Pyroxene-Spinel Peridotite/Pyroxenite Xenolith	628788	5827431	5
TA-2012-22	Olivine-bearing Spinel Xenolith	628770	5827424	5
TA-2012-23	Olivine-Pyroxene-Spinel Peridotite Xenolith	628770	5827424	5
TA-2012-24	Olivine-Pyroxene-Spinel Peridotite Xenolith + Host Basalt	628770	5827424	5
TA-2012-25	Spinel-bearing Dunite Xenolith	628955	5827547	5
TA-2012-44	Dunite Xenolith	628630	5826979	5+
TA-2012-45	Dunite Xenolith	628622	5826976	5+
TA-2012-46	Dunite Xenolith	628593	5826969	5+
TA-2012-48	Dunite Xenolith	628613	5826976	5+
TA-2012-49	Dunite Xenolith	628613	5826976	5+
TA-2012-55	Olivine-Pyroxene-Spinel Peridotite Xenolith	629565	5828132	6
TA-2012-56	Olivine-Pyroxene-Spinel Peridotite Xenolith	629565	5828132	6
TA-2012-62	Olivine-Pyroxene-Spinel Peridotite Xenolith	630012	5827612	7

Appendix B. Field description and GPS coordinates of the alkaline basalts

Sample #	Rock Type	Eastings	Northings	Property #
TA-2012-26	Host Rock - Vesicular Basalt	622827	5827459	5
TA-2012-27	Host Rock - Vesicular Basalt	628831	5827448	5
TA-2012-28	Host Rock - Vesicular Basalt	628831	5827448	5
TA-2012-29	Host Rock - Vesicular Basalt	628832	5827449	5
TA-2012-30	Host Rock - Vesicular Basalt	628829	5827449	5
TA-2012-31	Host Rock - Vesicular Basalt	628829	5827447	5
TA-2012-32	Host Rock - Vesicular Basalt	628819	5827446	5
TA-2012-33	Host Rock - Vesicular Basalt	628815	5827446	5
TA-2012-34	Host Rock - Vesicular Basalt	628823	5827440	5
TA-2012-35	Host Rock - Vesicular Basalt	628823	5827440	5
TA-2012-36	Host Rock - Vesicular Basalt	628823	5827440	5
TA-2012-37	Host Rock - Vesicular Basalt	628798	5827448	5
TA-2012-38	Host Rock - Vesicular Basalt	628894	5827442	5
TA-2012-39	Host Rock - Vesicular Basalt	628788	5827454	5
TA-2012-40	Host Rock - Vesicular Basalt	628788	5827449	5
TA-2012-41	Host Rock - Vesicular Basalt	628790	5827453	5
TA-2012-42	Host Rock - Vesicular Basalt	628628	5826974	5
TA-2012-43	Host Rock - Vesicular Basalt	628623	5826978	5
TA-2012-47	Host Rock - Vesicular Basalt	628623	5826978	5+
TA-2012-50	Host Rock - Vesicular Basalt	625948	5828288	2
TA-2012-51	Host Rock - Vesicular Basalt	625948	5828288	2
TA-2012-52	Host Rock - Vesicular Basalt	625948	5828288	2
TA-2012-53	Host Rock - Vesicular Basalt	624577	5830355	1
TA-2012-54	Host Rock - Vesicular Basalt	624577	5830355	1
TA-2012-57	Host Rock - Vesicular Basalt	624577	5830355	1
TA-2012-58	Host Rock - Vesicular Basalt	624577	5830355	1
TA-2012-59	Host Rock - Vesicular Basalt	624577	5830355	1
TA-2012-60	Host Rock - Vesicular Basalt	624577	5830355	1
TA-2012-61	Host Rock - Vesicular Basalt	624577	5830355	1

Vita Auctoris

Eyal Friedman was born in Tel Aviv, Israel in 1984. He completed his B.Sc. in Geology in 2012 at the University of Windsor. The same year he continued his education and began his M.Sc. degree at the University of Windsor with a focus on geochemistry. He hopes to graduate in December 2015.

"When I break a rock open with my pick, I'm a prophet. I see the past. I see the future. I know where the world is going, and where it's been. And I always, always want to know more."

– Christina Dodd